Pulsed Laser Deposited Indium Tin Oxide and its Indium-rich Composite Thin Films as Efficient Material Platforms for Probing Epsilon-near-zero Plasmon and Lossy Mode Resonance via Kretschmann-Raether Geometry

DOCTOR OF PHILOSOPHY

by

SUMIT GOSWAMI

DEPARTMENT OF PHYSICS

INDIAN INSTITUTE OF TECHNOLOGY GUWAHATI

GUWAHATI -781039, INDIA

NOVEMBER 2021

TH-2572_156121026

TH-2572_156121026

Pulsed Laser Deposited Indium Tin Oxide and its Indium-rich Composite Thin Films as Efficient Material Platforms for Probing Epsilon-near-zero Plasmon and Lossy Mode Resonance via Kretschmann-Raether Geometry

A Thesis submitted in partial fulfillment of the requirements for the award of the degree of

DOCTOR OF PHILOSOPHY

by

SUMIT GOSWAMI

DEPARTMENT OF PHYSICS

INDIAN INSTITUTE OF TECHNOLOGY GUWAHATI

GUWAHATI -781039, INDIA

NOVEMBER 2021

TH-2572_156121026

TH-2572_156121026

Dedicated to my Parents

TH-2572_156121026

TH-2572_156121026

Sumit Goswami
Registration No. 156121026
Department of Physics
Indian Institute of Technology Guwahati
North Guwahati - 781039
Assam, India

Statement

I hereby declare that the matter embodied in this thesis is the result of investigations carried out by me at the Department of Physics, Indian Institute of Technology Guwahati, Guwahati, India, under the supervision of **Prof. Ashwini Kumar Sharma**. This thesis has not been submitted to any university, institute or elsewhere for the award of the any degree, diploma or associate-ship.

Sumit Goswami

Date: 07/03/2022 **Sumit Goswami**

TH-2572_156121026

TH-2572_156121026

Ashwini Kumar Sharma, *Ph.D.*
Professor
Department of Physics
Email: aksharma@iitg.ac.in
Tel: +91-361-258-2724
Fax: +91-361-258-2749

भारतीय प्रौद्योगिकी संस्थान गुवाहाटी
Indian Institute of Technology Guwahati
North Guwahati - 781039
Assam, India

Certificate

This is to certify that work contained in the thesis entitled **'Pulsed Laser Deposited Indium Tin Oxide and its Indium-rich Composite Thin Films as Efficient Material Platforms for Probing Epsilon-near-zero Plasmon and Lossy Mode Resonance via Kretschmann-Raether Geometry'** by **Mr. Sumit Goswami** (Roll no 156121026), a student of Department of Physics, Indian Institute of Technology Guwahati, for the award of degree of Doctor of Philosophy, has been carried out under my supervision and the same has not been submitted elsewhere for the award of any other degree.

Date: 07/03/2022

(**Ashwini Kumar Sharma**)

TH-2572_156121026

TH-2572_156121026

Acknowledgment

First and foremost, I would like to express my sincere gratitude and thanks to my thesis supervisor, Prof. Ashwini Kumar Sharma, for his constant guidance and encouragement throughout my Ph.D. life. I would like to acknowledge him for investing valuable time in all the discussions and for helping me in the smooth conduction of my Ph.D. journey. I consider myself privileged for having such a friendly person as my Ph.D. supervisor.

I am immensely thankful to my DC committee members, Prof. Alika Khare, Prof. Subhash Thota, and Prof. Anugrah Singh, for their fruitful suggestions and constructive criticisms. I would like to specially mention the name of Prof. Alika Khare, my DC chairperson, who has helped me a lot in building up the overall understanding of the experimental research work through countless discussions and fruitful advices.

I am thankful to Prof. Perumal Alagarsamy for allowing me to perform the Hall measurement experiment in his lab and all the useful discussion regarding the electrical analysis of the samples. I would also like to thank Subrata Biswas for helping me with the Hall measurement setup.

I am grateful to all the past and presents HODs, scientific officers, and office staff of the Department of Physics, IIT Guwahati, for their unconditional support during my time of need. They have always extended their helping hand without any hesitation whenever I needed them.

I acknowledge the Central Instrument Facility (CIF), IIT Guwahati, and Department of Physics IIT Guwahati for providing necessary instrumental facilities for carrying out different experimental works over the years.

I would like to acknowledge MHRD for providing me monthly assistantship throughout my Ph.D. career.

I would like to thank all my past and present lab members: Dr. Indrajit, Dr. Partha, Dr. Shantakumar, Dr. Gyan, Dr. Rahul, Dr. Prahlad, Dr. Eshita, Dr. Gobinda, Sasmita Didi, Nagendra, Sudarshan, Pooja, Ankan, and Lwithwsa for their help and support during these

TH-2572_156121026

Ph.D. years. I would like to specially mention the names of Dr. Eshita, Dr. Gobinda, Sasmita Didi for being with me in my difficult times.

I also want to mention my beloved friends and seniors, Dr. Gourab, Dr. Goutam, Dr. Pratap, Dr. Subhrata, Dr. Abhik, Dr. Srikrishna, Dr. Sanjib, Dr. Kallol, Dr. Ramij, Dr. Suvankar, Karuna, Nagendra, Krishna, Shantiram, Udaratta, Sunil, Juhi, Manvendra, Jaishree, Aakanshu, and Debu, who were always there for me through thick and thin.

I want to express my humble gratitude to my family members and close friends back home for their constant encouragement and wholehearted support during all these years.

Sumit Goswami

TH-2572_156121026

Abstract

In the present thesis work, epsilon-near-zero (ENZ) plasmon resonance and lossy mode resonance (LMR) properties of pulsed laser deposited indium tin oxide (ITO) thin films and metallic indium-rich ITO thin films are studied experimentally with the help of Kretschmann–Raether geometry. Wide tuning of the ENZ wavelength over the wavelength range of 900 – 1700 nm is achieved for ITO thin films deposited under background gases such as O_2, N_2, Ar and He. The variation of ENZ plasmon resonance position is connected with the ENZ wavelengths at different background gases and the observed reflection spectra is understood through local field intensity enhancement factor analysis. The effect of surface roughness on the ENZ plasmon resonance is also studied for pulsed laser deposited ITO thin films deposited at different deposition times under a vacuum environment and near-perfect absorption is demonstrated experimentally for the film deposited at the highest deposition time. Such a high value of absorption just above the ENZ wavelength is corroborated by the strong electric field enhancement inside the film layer, while in terms of absorption loss, surface roughness leads the way and contributes immensely toward the occurrence of perfect absorption in the collective media. The LMR response of vacuum-deposited ITO thin film is compared to the films deposited under different background gases and the vacuum-deposited film is established as the material of choice due to their extremely high LMR response. Such a high degree of LMR response is attributed to the metallic indium generated interbands, leading to a high extinction coefficient in the visible range. The effect of overall film thickness on the LMR properties is investigated by depositing several ITO thin films at different deposition times under a vacuum environment. LMR attenuation value as high as -20 dB for transverse electric and -10 dB for transverse magnetic polarization is obtained for the ITO film with the highest film thickness. As an application of the LMR study, refractive index sensing is demonstrated in the RI range 1.3325 – 1.4459 for the ITO film with the highest thickness. A modified transfer matrix method algorithm, which takes the surface roughness of the films into account through the application of anisotropic Bruggeman effective medium approximation, is developed, and using this algorithm, the experimentally observed reflection spectra for ENZ plasmon resonance and LMR is resolved numerically.

TH-2572_156121026

Table of Contents

List of Figures iv

List of Tables x

Abbreviations xi

Symbols xiii

Chapter 1 Introduction 1

1.1 Surface plasmon resonance 2
1.2 Lossy mode resonance 5
1.3 Long range surface exciton-polaritons 7
1.4 Materials for SPR and LMR 8
1.5 ITO as a technological marvel material 9
1.5.1 Effect of tin doping and band structure of ITO 9
1.5.2 SPR studies in ITO thin films 12
1.5.3 Concept of epsilon-near-zero thin films and ITO as an epsilon-near-zero material 12
1.5.4 LMR studies in ITO thin films 14
1.6 Pulsed laser deposition technique for ITO thin films 14
1.7 Motivation 16
1.8 Organization of thesis 17

Chapter 2 Experimental Details, Characterization Techniques and Description of Numerical Framework 19

2.1 Thin Film Deposition 20
2.1.1 Preparation of ITO target 20
2.1.2 Substrate cleaning 21
2.1.3 PLD setup 22
2.2 Characterizations Techniques 26
2.3 Measurement of ENZ plasmon resonance and LMR spectra via K-R geometry 33
2.4 Description of the numerical approach 35
2.5 Conclusion 37

TH-2572_156121026

Chapter 3 Ambient Condition Dependent ENZ Plasmon Resonance Properties of PLD ITO Thin Films 39

3.1 Experimental Details and Characterization Techniques 40

3.2 Results and Discussions 41

3.2.1 Structural, morphological, optical, and electric properties of PLD-ITO thin films under various ambient conditions 41

3.2.2 Experimental reflection spectra 49

3.2.3 Description and Results of Numerical Analysis 51

3.2.4 Results of Electric Field Enhancement Analysis 52

3.3 Conclusion 54

Chapter 4 Effect of Surface Roughness on the ENZ Plasmon Resonance Properties of Vacuum-deposited ITO films.. 57

4.1 Experimental Details and Characterization Techniques 59

4.2 Experimental Results and Retails of Ellipsometry Analysis.. 60

4.2.1 Structural, morphological and electrical properties of vacuum-deposited ITO thin films 60

4.2.2 Experimental reflection spectra of randomly rough ITO film surface 63

4.2.3 Ellipsometry modeling 64

4.3 Description and results of numerical analysis... 70

4.4 Origin of the PA in randomly rough ITO thin films 73

4.5 Modified ENZ mode dispersion.. 76

4.6 Conclusion 78

Chapter 5 Ambient Condition Dependent LMR Response of PLD ITO Thin Films 79

5.1 Experimental details and Characterization techniques.. 80

5.2 Results and Discussions 82

5.2.1 Structural, morphological and optical properties of PLD-ITO thin films under different ambient.. 82

5.2.2 LMR spectra of PLD-ITO thin films under various ambient conditions 86

5.2.3 Results of the numerical analysis 87

5.2.4 Origin of high degree of LMR response in vacuum-deposited ITO films 88

5.3 Conclusion 90

TH-2572_156121026

Chapter 6 Thickness Dependency of LMR Response in Vacuum-deposited ITO Thin Films and Exploration of Refractive Index Sensing as an Application......93

6.1 Experimental Details and Characterization Techniques......94

6.2 Details of the Numerical analysis......96

6.3 Results and Discussions......96

6.3.1 Structural, morphological and optical properties of PLD-ITO thin films under different ambient......96

6.3.2 Experimentally measured LMR spectra of vacuum-deposited ITO thin films......101

6.3.3 Numerically simulated LMR spectra of vacuum-deposited ITO thin films......104

6.3.4 Refractive index sensing studies......106

6.4 Conclusion......109

Chapter 7 Conclusion and Future Scope......111

Bibliography......116

List of Publications......129

TH-2572_156121026

List of Figures

Figure 1-1. *Illustration of surface plasmon polaritons (SPPs) at the metal-dielectric interface. ε_1 and ε_2 are the dielectric constants of the metal and dielectric medium, respectively. A right-handed xyz- coordinate system is given for reference.* 2

Figure 1-2. *Schematic of the excitation of SPs via prism based geometry: (a) Otto geometry; (b) Kretschmann–Raether geometry. Evanescent field generated by the incident radiation is shown in the orange color for both the configurations. Blue colored sinusoidal wave along the x-direction represent the SPPs.* 4

Figure 1-3. *Different experimental arrangements used for the generation of LMR: (a) optical fiber (adapted from ref. [43]); (b) modified Kretschmann-Raether (K-R) geometry (adapted from ref. [44]); (c) planar waveguides with lateral light incidence (adapted from ref. [45]).* 6

Figure 1-4. *In_2O_3 crystal structure: Schematic of the (a) b site, and (b) d site. (b) Schematic of the tin doping sites at In_2O_3 crystal.* 10

Figure 1-5. *Schematic of the band structure of ITO: (a) low doping levels; (b) high doping levels (Burstein-Moss effect).* 11

Figure 2-1. *Step-by-step procedure of preparation of ITO pellet via solid-state synthesis method.* 20

Figure 2-2. *Photographs of ITO pellet (a) before sintering or pre-sintering, (b) after final sintering. A scale is shown below the pellet for size comparison.* 21

Figure 2-3. *Schematic diagram of the PLD setup.* 23

Figure 2-4. *Photograph of the in-house PLD setup.* 24

Figure 2-5. *Photograph of the in-house Hall measurement setup. Inset of the figure shows the inner view of the electromagnet containing Hall probe inside.* 27

Figure 2-6. *Schematic diagram of the SE setup.* 28

Figure 2-7. *Photograph of the SE instrument.* 29

Figure 2-8. *Optical layer model used for SE data fitting.* 30

Figure 2-9. *Photograph of the SE instrument during the measurement of reflectivity spectra at the incident angle 50°. Inset shows the schematic diagram of the K–R geometry-based setup used for the reflection measurement. A right-handed x–y–z coordinate system is displayed on*

TH-2572_156121026

the right-hand side to give an idea about the direction of propagation with respect to the sample geometry. *34*

Figure 2-10. *Photograph of the SE instrument during the measurement of reflectivity spectra at the incident angle 89.95°. Inset: Schematic of the K-R geometry employed for LMR measurement. A right-handed x-y-z coordinate system is placed at the right-hand side to describe the direction propagation with respect to the sample plane.* 35

Figure 3-1. *XRD pattern of ITO thin films deposited under various ambient conditions:* O_2 *(solid red line);* N_2 *(dashed blue line); Ar (dotted magenta line); He (dash-dot olive line).* . . 42

Figure 3-2. *FESEM images of ITO thin films under different background gases: (a)* O_2*; (b)* N_2*; (c) Ar; (d) He.* 42

Figure 3-3. *5×5 μm 2D AFM micrograph of PLD-ITO thin films under various ambient conditions: (a)* O_2*; (b)* N_2*; (c) Ar; (d) He.* 43

Figure 3-4. *Transmission spectra of ITO thin films deposited under various deposition environments:* O_2 *(solid red line);* N_2 *(dashed blue line); Ar (dotted magenta line); He (dash-dot olive line).* 44

Figure 3-5. *Variation of real (* $\langle\varepsilon_1\rangle$ *) and imaginary (* $\langle\varepsilon_2\rangle$ *) part of pseudo-dielectric permittivity (geometric dots represent measured data, and solid lines represents fitted) of ITO thin films deposited at different ambient conditions: (a)* O_2*; (b)* N_2*; (c) Ar; (d) He.* 45

Figure 3-6. *Variation of (a) real (* ε_1 *) and (b)imaginary (* ε_2 *) part of permittivity of the PLD-ITO thin film under different background gases:* O_2 *(solid red line);* N_2 *(dashed blue line); Ar (dotted magenta line); He (dash-dot olive line).* 48

Figure 3-7. *(a) Voltage vs. current graph obtained using four probe method; (b) comparison of sheet resistance determined by four probe and ellipsometry method.* 49

Figure 3-8. *Experimentally measured reflection spectra over the wavelength range of 900 – 1700 nm for ITO thin films deposited at different ambient conditions: (a)* O_2*; (b)* N_2*; (c) Ar; (d) He. Color codes of various incidence angles (from 50° to 70°) are given over the right-hand side of the figure.* 50

Figure 3-9. *Numerically simulated reflection spectra of ITO thin films deposited under different ambient gases: (a)* O_2*; (b)* N_2*; (c) Ar; (c) He. The color code for incident angles in the range of 50° to 70° is shown at the right-hand side of the figure.* 52

Figure 3-10. *Color map of the angular dispersion of LEIEF over the wavelength range of 900 – 1700 nm for PLD-ITO thin under background gases: (a)* O_2*; (b)* N_2*; (c) Ar; (c) He. The color bar positioned at the right-hand side of each sub-figures indicates the amplitude of LEIEF.* 53

TH-2572_156121026

Figure 4-1. *Rietveld refined the XRD pattern for all the samples in the range of 2θ values from 10° to 70°.* 60

Figure 4-2. *Acquired FESEM images of vacuum-deposited ITO thin films for different deposition times: (a) S1 (20 min); (b) S2 (40 min); (c) S3 (80 min).* 61

Figure 4-3. *2D view of AFM micrographs taken over a surface area of 5×5 µm for ITO films at different deposition times: (a) S1 (20 min); (b) S2 (40 min); (c) S3 (80 min).* 62

Figure 4-4. *Variation of Hall resistance, Rxy with the applied magnetic field for ITO pure (black circle), sample S3 (red square), and silver film (blue triangle).* 62

Figure 4-5. *Experimentally measured reflection spectra over the wavelength range of 900 – 1700 nm for the samples: (a) S1; (b) S2; (c) S3. Color codes of various incidence angles (from 50° to 70°) are given over the right hand side of the figure.* 63

Figure 4-6. *(a) Pictorial representation of the random sized and shaped particulates observed in the FESEM image of the sample S3; (b) The simplified version of the structure in figure (a) is obtained through the application of the ABEMA model.* 66

Figure 4-7. *Variation of the measured and fitted spectra of the real ($\langle \varepsilon_1 \rangle$) and imaginary ($\langle \varepsilon_2 \rangle$) part of pseudo-dielectric permittivity over the wavelength range of 220 – 1700 nm for vacuum-deposited at different deposition times: (a) S1 (20 min); (b) S2 (40 min); (c) S3 (80 min).* 66

Figure 4-8. *Variation of the real (ε_1) and imaginary part of the permittivity (ε_2) in the wavelength range of 300 – 1700 nm with the deposition time for the vacuum deposited ITO films. The black dashed line along the middle represents the zero value of the real part of the permittivity.* 69

Figure 4-9. *(a) Comparison of the experimentally measured reflection spectra (black solid spheres) with the simulated spectra for the sample S3 at the incidence angle 50° using three plausible fitting arguments: (i) film + surface roughness (solid red line); (ii) single surface roughness layer described by ABEMA (parameters are given in Table SI1) (dash-dot blue line); (iii) Film + surface roughness layer simulated by employing the procedure described in the ref. [192] (dotted olive line); (b) Comparison of experimental (black sphere) and simulated ENZ plasmon resonance spectra for sample S3 at different Drude scattering frequency values: $E_\Gamma = 0$ (red solid curve), $E_\Gamma = 0.05$ (blue dash-dot curve), $E_\Gamma = 0.1$ (dotted olive curve). Inset shows the expanded view of the experimental vs. simulated spectra near resonance values.* 71

Figure 4-10. *Numerically simulated reflection spectra for all the samples over the wavelength range of 900 – 1700 nm obtained by following the film + surface roughness (ABEMA) model:*

TH-2572_156121026

(a) S1; (b) S2; (c) S3. The color code for various angles is pasted on the right hand side of the figure. 72

Figure 4-11. *Color maps of the wavelength and angular dependency of absorption intensity (1 – reflection intensity) for the samples: (a) S1; (b) S2; (c) S3. The color bar stationed on the extreme right side of the figures represents the absorption intensity. In figure (c), the cyan star at the wavelength 1335 nm and green square at the wavelength 1306 nm imply the experimentally and numerically obtained PA points at the incident angle 50° and 44.32°, respectively, for the sample S3.* 73

Figure 4-12. *(a) Color map of the spatial distribution of the square of the amplitude of the electric field intensity along the z-direction over the wavelength range of 900 – 1700 nm for the sample S3. The dashed and solid white vertical lines represent the ENZ wavelength and numerically acquired PA wavelength, respectively. The color bar positioned at the right hand side indicates the value of the squared electric field amplitude. (b) Spatial distribution of the absorption loss density.* 74

Figure 4-13. *(a) Color map of the wavelength-wise and spatial distribution of the square of the amplitude of the electric field intensity along the z-direction for the sample S1. (b) Spatial distribution of the absorption loss density.* 75

Figure 4-14. *(a) Color map of the wavelength-wise and spatial distribution of the square of the amplitude of the electric field intensity along the z-direction for the sample S2. (b) Spatial distribution of the absorption loss density.* 75

Figure 5-1. *Ray diagram of the microspot doublet lens used LMR measurement via ellipsometer.* 81

Figure 5-2. *An illustration of the interaction of the incident beam with the K-R set-up: (a) at an optimal height; (b) at a slightly different height.* 82

Figure 5-3. *Variation of (a) refractive index and (b) extinction coefficient with the incident wavelength for ITO thin films deposited at various ambient condition.* 85

Figure 5-4. *Experimental LMR spectra of ITO films deposited at various ambient conditions over the wavelength range 400 – 1700 nm for (a) TE polarization and (b) TM polarization.* 86

Figure 5-5. *Numerically simulated LMR spectra of ITO films deposited at different ambient conditions over the wavelength range 400 – 1700 nm for (a) TE polarization and (b) TM polarization.* 88

Figure 5-6. *Rietveld refined XRD pattern of the samples A and B in the range of 2θ values from 10° to 70°.* 89

TH-2572_156121026

Figure 5-7. *2D AFM micrographs of the samples (a) A (In: 3.11%) and (b) B (In: 8.03%) taken over the surface area of 5×5 μm.* 89

Figure 5-8. *Experimental LMR spectra for samples A (In: 3.11%) and B (In: 8.03%) for TE (solid line) and TM (dotted line) polarization.* 90

Figure 6-1. *3D representation of the K-R geometry based set up for refractive index sensitivity measurement. A right-handed coordinate system is placed at the left hand side to describe the direction propagation with respect to the sample plane.* 95

Figure 6-2. *(a) AFM and (b) FESEM images of PLD-ITO thin film under vacuum environment for different deposition time of 120 min (S4).* 97

Figure 6-3. *Rietveld refined XRD pattern of sample S4.* 98

Figure 6-4. *Variation of the measured and fitted spectra of the real ($\langle \varepsilon_1 \rangle$) and imaginary ($\langle \varepsilon_2 \rangle$) part of pseudo-dielectric permittivity over the wavelength range of 220 – 1700 nm for the sample S4.* 99

Figure 6-5. *Variation of the refractive index (n) and extinction coefficient (k) over the 300 – 1700 nm wavelength range for the vacuum deposited ITO samples.* 101

Figure 6-6. *Angular distribution of experimentally measured LMR spectra for TE polarization of ITO thin films deposited under vacuum environment at different deposition times: (a) S1 (20 min), (b) S2 (40 min), (c) S3 (80 min), (d) S4 (120 min). The color code used for the incident angles ranging from 80° to 89.95° is pasted at the right-hand side of the figure.* 102

Figure 6-7. *Angular distribution of experimentally measured LMR spectra for TM polarization of ITO thin films deposited under vacuum environment at different deposition times: (a) S1 (20 min), (b) S2 (40 min), (c) S3 (80 min), (d) S4 (120 min). The color code used for the incident angles ranging from 80° to 89.95° is pasted at the right-hand side of the figure.* 103

Figure 6-8. *Comparison of experimentally measured LMR spectra for (a) TE and (b) TM polarization at the incident angle of 89.95° for different thickness of vacuum-deposited ITO thin films.* 103

Figure 6-9. *Angular distribution of experimentally measured LMR spectra for TE polarization of ITO thin films deposited under vacuum environment at different deposition times: (a) S1 (20 min), (b) S2 (40 min), (c) S3 (80 min), (d) S4 (120 min). The color code used for the incident angles ranging from 80° to 89.95° is given on the right-hand side of the figure.* 105

Figure 6-10. *Angular distribution of experimentally measured LMR spectra for TM polarization of ITO thin films deposited under vacuum environment at different deposition times: (a) S1 (20 min), (b) S2 (40 min), (c) S3 (80 min), (d) S4 (120 min). The color code used*

TH-2572_156121026

for the incident angles ranging from 80° to 89.95° is given on the right-hand side of the figure. 106

Figure 6-11. *Experimentally measured LMR spectra of sample S4 at several SMRI values ranging from 1.3325 (solid black line) – 1.4459 (solid violet line) RIU: (a) for TE polarization, and (b) for TM polarization.* 107

Figure 6-12. *Calculated (via Lorentz fitting of the LMR spectra) LMR wavelength at different refractive index values: (a) for TE polarization and (b) for TM polarization. A scale break is given in both figures over the refractive index range of 1.02 – 1.3125 RIU. In the y-axis, a scale break is put at the wavelength range of 750 – 795 nm for figure (a) and 680 – 815 nm for figure (b). The error involved in determining LMR wavelength via Lorentz curve fitting is also indicated in terms of error bar for each LMR wavelength value. The sensitivity of LMR for every refractive index increment step is also given in both figures (a) and (b).* 108

Figure 6-13. *(a) linear fit of the LMR wavelengths for TE polarization over the region I (1.3325 - 1.3914; solid red line) and region II (1.4165 - 1.4459; solid olive line) of refractive index values; (b) linear fit of LMR wavelengths for TM polarization over the entire refractive index range (1.3325 – 1.4459).* 109

TH-2572_156121026

List of Tables

Table 3-1. *The list of parameters obtained from SE fitting of ITO thin films deposited under different background gases. Along with the plasma energy (E_P) and broadening (E_Γ), carrier concentration and sheet resistance extracted from the Drude model is also given. In the table, two Lorentz oscillators are designated by 1st and 2nd. Oscillator strength (f), central position (E_0), and width (Γ) is given for each oscillators. Uncertainties associated with different parameters are also reported. Note that, SR stands for surface roughness.* 47

Table 4-1. *The list of parameters acquired from SE data fitting for all the vacuum deposited ITO thin films. The last 3 rows are SE fitting parameters for sample S3 at different Drude scattering frequency values, i.e. E_Γ =0, E_Γ =0.05, and E_Γ =0.1. In the table, four Lorentz oscillators are designated by 1st, 2nd, 3rd, and 4th. Oscillator strength (f), central position (E_0), and width (Γ) is given for each oscillators. Uncertainties associated with different parameters are also reported. Note that, SR stands for surface roughness.* 67

Table 4-2. *SE fitting parameters for the sample S3 considering only the surface roughness layer.* 70

Table 6-1. *The list of parameters acquired from SE data fitting of sample S4. In the table, four Lorentz oscillators are designated by 1st, 2nd, 3rd, and 4th. Oscillator strength (f), central position (E_0), and width (Γ) is given for each oscillators. Uncertainties associated with different parameters are also reported. Note that, SR stands for surface roughness.* 100

TH-2572_156121026

Abbreviations

2D	Two-dimensional
3D	Three-dimensional
ABEMA	Anisotropic Bruggeman effective medium approximation
AFM	Atomic force microscopy
arb. unit	Arbitrary unit
ATR	Attenuated total reflection
BEMA	Bruggeman effective medium approximation
CCD	Charge coupled device
CP	Capacitive plasmon
CPR	Capacitive plasmon resonance
DL	Drude-Lorentz
EMR	Electromagnetic resonance
ENZ	Epsilon-near-zero
et. al.	and others
etc.	Et cetera (and other similar things)
FESEM	Field Emission scanning electron microscope
FWHM	Full width at half maximum
ITO	Indium tin oxide
K-R	Kretschmann–Raether
LFIEF	Local field intensity enhancement factor
LMR	Lossy mode resonance
LRSEP	Long range surface exciton-polaritons
Nd:YAG	Neodymium yttrium aluminum garnet
NIR	Near infrared
OMA	Optical multichannel analyzer

TH-2572_156121026

PA	Perfect absorption
PLA	Pulsed laser ablation
PLD	Pulsed laser deposition
PLD-ITO	Plasma laser deposited ITO
RI	Refractive index
RMSE	Root mean square error
SE	Spectroscopic ellipsometry
SEA	Spectroscopic ellipsometry analyzer
SP	Surface plasmon
SPP	Surface plasmon polaritons
SPR	Surface plasmon resonance
SR	Surface roughness
TE	Transverse electric
TM	Transverse magnetic
TMM	Transfer matric method
TM	Transverse magnetic
UV-Vis	Ultra Violate-Visible
XRD	X-ray diffraction

TH-2572_156121026

Symbols

~	Approximately	Δ	Phase difference between *p*- and *s*-polarization
$^{\circ}$	Degree	Ψ	Amplitude ratio between reflection coefficients of *p*- and *s*-polarization
A	Absorbance	ρ_s	Resistivity
β	Wave vector of surface plasmon polaritons	σ	Conductivity
cm	Centimeter	Ω	Ohm
$^{\circ}C$	Degree Celsius	$\hbar$	Reduced Plankc's constant
dB	Decibel	***Hz***	Hertz
$\langle \varepsilon_1 \rangle$	Real part of pseudo-dielectric permittivity	***mbar***	Milibar
$\langle \varepsilon_2 \rangle$	Imaginary part of pseudo-dielectric permittivity	***min***	Minutes
ε_1	Real part of dielectric permittivity	***mm***	Milimeter
ε_2	Imaginary part of dielectric permittivity	n_e	Carrier concentration
ε_{ITO}	Dielectric permittivity of ITO layer	n	Refractive index
ε_{SR}	Dielectric permittivity of surface roughness layer	***nm***	Nanometer
ε_{void}	Dielectric permittivity of void	***ns***	Nanosecond
ε_{∞}	High frequency background permittivity	k	Extinction coefficient
f_{ITO}	Volume fraction of ITO	k_0	Incident wave vector

TH-2572_156121026

f_{void}	Volume fraction of void	***R***	Reflectance
f	Strength of the Lorentz oscillator	***T***	Transmission
E_0	Central position of the Lorentz oscillator	***RIU***	Refractive index unit
Γ	Width of the Lorentz oscillator	R_s	Sheet resistance
E_P	Plasma energy of the Drude model	***Sq.***	Square
E_Γ	Plasma broadening of the Drude model	***S/m***	Siemens per meter
eV	Electron volt	μm	Micrometer
λ	Wavelength of light		

TH-2572_156121026

Chapter 1
Introduction

Ever since its discovery by Fraunhofer in 1817 [1], thin film technology has gradually become an integral part of our day-to-day life with vast application domains ranging from smartphone displays to solar cells [2, 3]. This remarkable journey has been made possible through advancements in sophisticated deposition techniques and modern lithographic techniques. Till now, thin film technology has been utilized in diverse fields of science, like, electronics, optics, magnetics, photonics, space, aircraft, etc. Amongst this plethora of scientific fields, thin-film optics, which is based on the interaction of electrometric waves with thin films, is fundamentally very fascinating. Thin-film optical systems also offer many advantages over their bulk counterparts, such as the compact size of the devices, chemical stability to environmental changes, possibility of surface sensing/probing, relatively large light intensity even for minimal laser powers, etc. [4].

It is well known that the solutions of Maxwell's equations can characterize the interaction of electromagnetic waves with any physical system. Maxwell's equations can be solved by applying boundary conditions at the substrate-film and film-air interfaces in case of single-layered thin films. The solutions of these equations are termed propagation *modes,* and if, somehow, the incident light wave is bounded and/or guided by the thin film layer in question, then the modes are called *waveguide modes* [4]. The confinement of the incident light wave can be achieved by launching the light at an angle greater than the critical angle required for *total internal reflection* (TIR) of a particular interface. An incident light launched at these TIR angles gives rise to an exponentially decaying field normal to the interface in the light propagation direction. This field is known as the *evanescent field,* and it is a characteristic feature of the bound waveguide modes. In the case of absorbing thin films, i.e., the films with finite extinction coefficient (k), this *evanescent field* can cause an energy transfer between the incident light and the thin film through various means, as will be discussed in the sections 1.1, 1.2 and 1.3. This resonant excitation is called *electromagnetic resonance* (EMR) and leads to strong attenuation in a specific range of wavelength/angle depending on the wavelength/angular interrogation modes [5]. Depending upon the means by which the

TH-2572_156121026

excitation is achieved and the dielectric properties of the thin film coating materials and surroundings, EMR can be classified into three major categories: *surface plasmon resonance* (SPR), l*ossy mode resonance* (LMR), and *long range surface exciton-polariton* (LRSEP) [5, 6]. All three EMRs are discussed in detail in the following subsections.

1.1 Surface plasmon resonance

In the case of surface plasmon resonance (SPR), the energy transfer between the thin film and the evanescent field occurs through *surface plasmons* (SPs). *Surface plasmon* (SP) is special kind of a plasma oscillation mode that exists at the interface of metal-dielectric medium [7]. Surface plasmon waves (SPWs), or more precisely *surface plasmon polaritons* (SPPs), are defined as the waves of charge density fluctuations that propagate along this interface [8]. SPPs are essentially two-dimensional (2D) electromagnetic waves that decay evanescently at normal directions and exist only at the interface. A schematic illustration of the SPPs caused by the electric charge accumulation in the metal-dielectric interface is shown in Figure 1-1. SPPs can be generated only on metal or metal-like materials having abundant free electrons available at the surface [8]. This requirement put some basic restrictions on the material's dielectric properties. The real part of dielectric permittivity of the material should be negative. The absolute value of this real part should be greater than its own imaginary part and the permittivity of the surrounding medium.

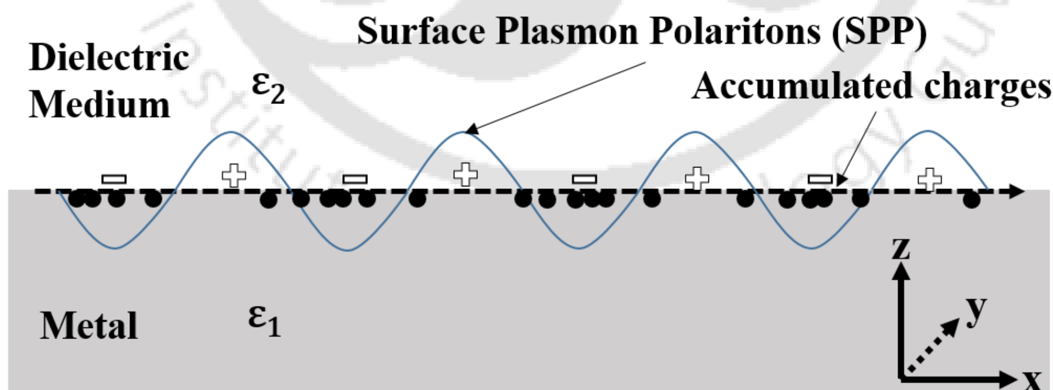

Figure 1-1. Illustration of surface plasmon polaritons (SPPs) at the metal-dielectric interface. ε_1 and ε_2 are the dielectric constants of the metal and dielectric medium, respectively. A right-handed xyz-coordinate system is given for reference.

TH-2572_156121026

Furthermore, SPR, i.e., the resonant excitation of SPs, can be achieved only via transverse magnetic (TM) polarization having the electric field component normal to the interface [8]. This is a consequence of the boundary conditions involving tangential components of the electric (E_y) and magnetic (H_x) fields.

The characteristic equation for SPPs at the metal-dielectric interface, as depicted in Figure 1-1, is given by,

$$\beta = k_0 \sqrt{\frac{\varepsilon_1 \varepsilon_2}{\varepsilon_1 + \varepsilon_2}} \tag{1.1}$$

where β is the wave vector characterizing the propagation of SPs, and $k_0 = \frac{2\pi}{\lambda}$ is the wave vector for incident light of wavelength λ. The imaginary part of the SPP wave vector β is responsible for the ohmic damping of the SPWs and determines the internal absorption in the film. A closer inspection of the eqn. (1.1) reveals that $\beta > k_0$. This enhanced wave vector or momentum physically means a strong coupling between the incident and accumulated surface charges in the metal-dielectric interface [9]. Additionally, the bounded nature of SPPs ensures that the dispersion curve represented by eqn. (1.1) lies on the right hand side of the light line of incident dielectric medium. Thus, normal three-dimensional (3D) light beam cannot excite the SPs unless there is a special arrangement for achieving this *phase-matching* or *momentum-matching* with the SPPs [8]. Many techniques have been employed over the for this purpose. Prism coupling [10, 11], grating coupling [12, 13], excitation via fiber optics [14], etc., are some of the most popular ones. Among these coupling schemes, prism coupling offers relative ease of excitation and does not require any extra lithographic techniques or modification in deposition system.

There are two basic prism coupling configurations used in SPR excitation: Otto [15] and Kretschmann–Raether [16] configuration. Together, they are referred to as attenuated total reflection (ATR) geometry because of the usage of an incident angle greater than TIR [17]. In 1968, Otto presented the first-ever experimental demonstration of excitation of SPs in the metal-dielectric interface by using a geometry similar to that shown in Figure 1-2. (a). In his pioneering work, Otto showed that SPs could be excited in the metal-air interface through the evanescent field of the incident radiation if a sufficient air gap is maintained between a prism

TH-2572_156121026

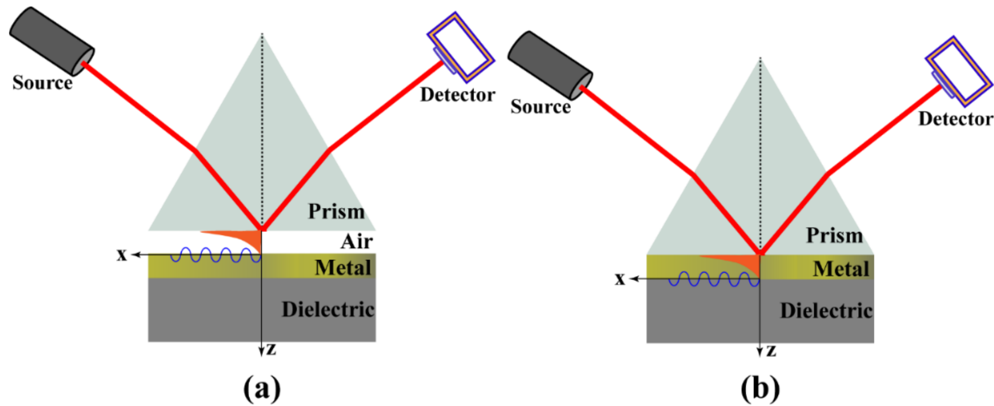

Figure 1-2. Schematic of the excitation of SPs via prism based geometry: (a) Otto geometry; (b) Kretschmann–Raether geometry. Evanescent field generated by the incident radiation is shown in the orange color for both the configurations. Blue colored sinusoidal wave along the x-direction represent the SPPs.

and the metal layer [15]. In this condition, the parallel component of the incident wave vector is matched with the real value of β and SPR is achieved. SPR is signified as a distinct dip in the reflected spectra for a specific incident angle or wavelength value. But the problem with Otto configuration is that a precise air gap of a few hundred nanometers should be maintained between prism and metal layer [18], which is very cumbersome to achive experimentally. Kretschmann solved this problem by depositing metal film directly onto the prism [16], as shown in Figure 1-2. (b). The excitation mechanism is quite similar to that of Otto geometry; the only thing is that SPs are excited at the outer layer (metal-dielectric interface) instead of the inner layer (metal-air interface), as is the case for Otto configuration. Kretschmann geometry is also referred to as Kretschmann–Raether configuration because of the extensive theoretical and experimental contribution made by Raether towards the understanding this geometry [19]. Therefore, "Kretschmann–Raether (K-R) configuration" nomenclature is used throughout the thesis.

The most important advantage of SPR phenomenon is that its resonance position is sensitive to the environmental changes in the outer dielectric layer. Thus, by observing SPR position (wavelength or incidence angle depending upon the mode of interrogation), one can sense several physical, chemical, and biological species [20, 21]. The most prominent use of prism based SPR is found in the biomedical industry with already available biosensors in the market [22-24]. SPR is also commonly used for the detection of adulterates in the food industry

TH-2572_156121026

[25, 26]. Other sensing application of K-R geometry includes refractive index (RI) sensor [27, 28], gas sensor [29, 30], humidity sensor [31], etc., sensing. Apart from these obvious sensing-based applications, when excited resonantly, SPPs can confine the electric field at a length shorter than the wavelength of incident light [7]. Field enhancement on such a small scale has led to some extraordinary applications, all under the banner of *plasmonics*, a term coined by H. Atwater group in the year 2000 [7]. Plasmonics field enhancement in K-R geometry has been utilized in solar cells [32, 33], strong coupling [34, 35], near field microscopy [36, 37], and hot carrier energy distribution determination [38].

1.2 Lossy mode resonance

The lossy mode resonance (LMR) phenomenon comes into play when there is a sufficient coupling between the waveguide modes and the *lossy modes* of the thin films [6]. The necessary condition for this coupling is that there should be a considerable overlap between modal fields [39]. Also, the phase-matching (i.e., equal values of effective indices of lossy modes and evanescent modes) should be satisfied. The occurrence of these two conditions simultaneously in a thin film depends upon the cutoff condition for a particular waveguide mode [6]. The cutoff condition is defined as the starting point for the mode guidance. An increase in film thickness initiates this mode guidance through the modal redistribution [40]. And, for a fixed film thickness value, maximum coupling occurs at those incident wavelengths or angles for which the phase-matching condition is satisfied. When the maximum coupling is achieved for a waveguide mode, a distinct dip transpires at some particular wavelength or angle in the reflection spectra. This resonance dip signifies the LMR excitation for that particular waveguide mode.

For the excitation of LMR with evanescent waves of effective index $n_{eff} = \sqrt{\varepsilon}\sin\theta_i$, the incident light must graze at angles reaching 90° [41]. Thus, optical fibers, which inherently require focused light to be launched parallelly for maximum coupling efficiency [42], are the more natural choice to excite LMR. A schematic representation of the LMR excitation via fiber optics is as shown in Figure 1-3. (a). In contrast, prism based excitation of LMR is very difficult because of the incident beam falling on the slanted side of the prism. This type of incident geometry increases the actual angle in the prism-thin film interface even for near-parallel incid-

TH-2572_156121026

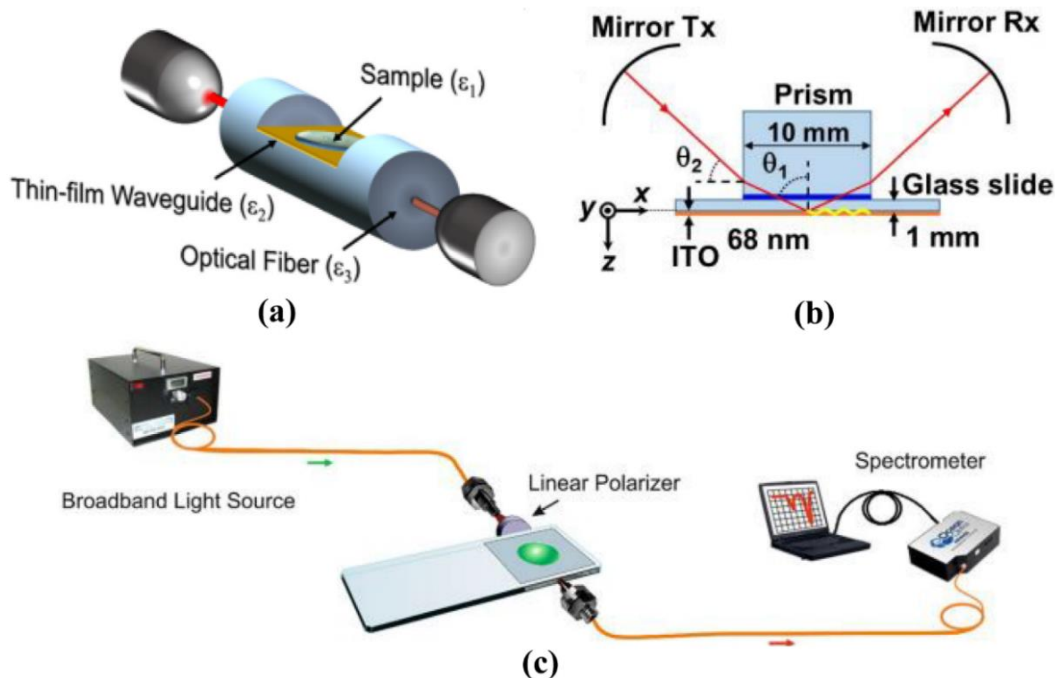

Figure 1-3. Different experimental arrangements used for the generation of LMR: (a) optical fiber (adapted from ref. [43]); (b) modified Kretschmann-Raether (K-R) geometry (adapted from ref. [44]); (c) planar waveguides with lateral light incidence (adapted from ref. [45]).

ence. Del Villar *et al.* solved this problem by making a slight adjustment in the conventional K-R geometry [44]. As shown in Figure 1-3. (b), LMR excitation was achieved in a modified K-R geometry, where the light was incident over the lateral side of an all-side-polished prism. Recently, planer waveguides were also found to be a viable experimental route for the generation of LMR [45, 46]. Figure 1-3. (c) depicts the experimental setup involving nanocoated planer waveguides where the light was incident laterally over the film surface for efficient LMR generation.

Furthermore, LMR can be excited for those materials having a positive real part of permittivity [41]. In addition, the amplitude of the real part of permittivity should be greater than its imaginary part and the permittivity of the surrounding medium. Thus, LMR excitation can only be achieved in dielectric materials, which are at the opposite end of the material spectrum compared to noble metals. LMR offers some basic advantages over the SPR as a whole. To begin with, both transverse electric (TE) and TM polarization can be used for the generation of LMR [41]. In contrast, SPR is excited for TM polarization, as discussed earlier. This strict requirement complicates the matter when it comes to device fabrication. Additionally, the requirement of low-cost dielectric materials as compared to expensive metals

TH-2572_156121026

reduces the fabrication cost significantly in the case of LMR [47]. Last but not least, multiple numbers of LMR dips can be generated just by increasing the film thickness; while SPR is a single resonance phenomenon for a particular material irrespective of the changes in the film thickness [41]. The multiplicity of the resonance spectra appears to be an excellent advantage for LMR based devices with the possibility of using different LMR for different sensing applications.

Similar to the SPR, LMR is also sensitive to changes in the dielectric medium succeeding the LMR active layer. RI sensing is the most widely studied application of the LMR because it constitutes the building block of any biological or chemical sensor. Numerous refractometers based on the LMR phenomenon have been demonstrated in the literature [48-50], with reported sensitivity going as high as 304,361 nm/RIU for the RI range of 1.4487–1.449 [51]. LMR has been utilized for sensing other physical parameters like humidity [52], human breath [53], and voltage [54]. LMR is also sensitive to chemical species such as pH [55], gases [56, 57], ethanol [58], aggressive liquids [59], to name a few. Additionally, effective sensing of different biological species like immunoglobulin G (IgG) [60], C-reactive protein (CRP) [61], and biotin [62]has been achieved via LMR.

1.3 Long range surface exciton-polaritons

There exists a third kind of EMR known as long-range surface exciton-polaritons (LRSEP), which is relatively less known among the research community. These types of surface modes come into play in the case of thin, highly absorbing films cladded symmetrically from each side with comparatively thick transparent dielectric mediums [63]. The upper and lower surfaces of this active absorbing layer cannot support any surface mode. But, when cladded between two dielectric materials, LRSEP arises due to the exclusion of the electric field in the thin active layer through symmetric surface charges over each interface [63]. Similar to the previous two EMRs, LRSEPs also cannot be excited directly by the normal light beam. Prism based ATR geometry, more precisely Otto type configuration, is needed for the excitation of LRSEP. The only difference is that the air gap between the prism and active layer, as shown in Figure 1-2. (a), should be replaced by a dielectric layer similar to the last substrate layer. Grating couplers are also used to excited the LRSEPs in one or two studies [64], though the Otto geometry is the regular standard [63, 65, 66].

TH-2572_156121026

Now, the material required for LRSEPs is slightly uncommon as compared to SPR and LMR. The required material should have a very high value of imaginary permittivity. At the same time, its real part of permittivity should be close to zero. This requirement is fulfilled in a material near its transverse-exciton frequency [67]. That's why the exciton term is used in the nomenclature of LRSEP, even though no real excitonic resonance is involved. Excitation of LRSEPs has been demonstrated in vanadium [63], palladium [68], molybdenum [66], and amorphous silicon [65]. However, there are very few credible reports available for LRSEP compared to the vast literature of the other two EMRs. This is because of the unique permittivity requirements, which only exist near the interband in a material [67]. These interband regions are very difficult to access experimentally in common materials.

1.4 Materials for SPR and LMR

Noble metals are widely regarded as the most conventional material for SPR or plasmonics-related studies [8]. Several studies have been done on metals like gold, silver, copper, aluminum, and so on [69], over the years portraying the SPR behavior when probed via K-R geometry. However, apart from bio-sensing, other exotic application domains of SPR and plasmonics as a whole have not been realized fully at the industry level till now. This may be due to some fundamental drawbacks associated with these noble metals, such as high optical loss, instability to harsh environmental conditions, incompatibility with standard CMOS device fabrication techniques, to name a few [70]. These ambiguities have prompted researchers around the globe to look for possible alternatives to noble metals, especially in the case of plasmonics. Transparent conducting oxides like indium tin oxide (ITO), aluminum/gallium doped zinc oxide (AZO/GZO), and fluorine/dysprosium doped cadmium oxides (F:CdO/Dy:CdO) and transition metal nitrides such as titanium/zirconium/hafnium nitrides (TiN/ZrN/HfN) have emerged as possible alternatives to conventional plasmonics materials [69, 70]. Among these alternatives, optical loss in ITO is less compared to noble metals because of its moderate carrier density. Additionally, there are no interband transitions present in the region of SPR excitation in the case of ITO, which further minimizes the losses. ITO is chemically more stable than conventional metals and can be fabricated easily using CMOS fabrication techniques. Moreover, an ultra-thin layer of ITO films can be deposited without the formation of islands.

TH-2572_156121026

Dielectric materials with a high refractive index (HRI) and low extinction coefficient (*k*) or optical losses are the material of choice for LMR [47]. In this context, different metal oxides like ITO [41], indium oxide (In_2O_3) [71], titanium oxide (TiO_2) [48], tin oxide (SnO_2) [56], zinc oxide (ZnO) [72] and its doped derivatives [73, 74] are most widely used for LMR excitation. Additionally, other HRI coating materials like silicon [75], graphene oxide [58], polymers, perovskites [76], etc. are also being tried so far to probe LMR at different wavelength regimes. Amongst this plethora of material choices, the bulk of the LMR studies, be it fundamental property investigation or studies based sensing applications, are done in ITO thin films. The reasons behind this tendency are the availability of ITO films at the commercial level, well-known optical properties of ITO, and chemical stability. Also, deposition schemes on complicated geometries like fiber optics are well-rehearsed in the case of ITO. Most importantly, SPR and LMR can be achieved simultaneously in ITO [44], which offers additional advantages in sensing and other applications. ITO satisfies the required conditions of SPR in the NIR region, while in the visible region, excitation LMR is achievable. Keeping these things in mind, ITO is chosen as a material platform to study the LMR and SPR properties and their applications in this thesis.

1.5 ITO as a technological marvel material

ITO remains one of the most celebrated material platforms in optoelectronic industries with already marketized applications in touch panel displays [2, 77], thin film transistors [78, 79], solar photovoltaics [80, 81], anti-reflective coatings [82], energy-efficient windows [83], gas sensors [84], to name a few. The wide bandgap of ITO is responsible for its high degree visible range of transparency, while tin (Sn) doping and internal oxygen vacancies account for its excellent electrical properties like low resistivity and high conductivity [85]. A unique combination of these two properties has established ITO as a top-drawer material in the technological field.

1.5.1 Effect of tin doping and band structure of ITO

The internal structure of ITO is almost similar to its founding material, In_2O_3. In_2O_3 belongs to a space group Ia3 material having a cubic bixbyite structure with a lattice constant of 10.118 nm [86]. The calculated density for the In_2O_3 unit cell is 7.120 gm/cm^3. There are exactly 80 atoms in the primitive unit cell of In_2O_3, out of which 32 are metallic indium cations,

TH-2572_156121026

and oxygen (O_2) anions account for the rest of the atoms [87]. These 32 indium cations sit on two discrete kinds of non-equivalent six-fold coordinate sites, popularly known as *b* and *d* sites. One-fourth of the indium cations resides at the *b* sites, which is a trigonally compressed octahedral. At this site, cations (In^{3+}) and anions (O^{2-}) are equidistantly spaced at 2.18 Å. The remaining three-fourth of the cations reside on highly distorted octahedral *d*-sites. It has three sets of In – O distances: 2.13, 2.19, and 2.21 Å. As shown in Figure 1-4 (a)-(b), In cations reside at the center while six oxygen atoms sit at six corners of the distorted cubes for both *b* and *d* sites. Two oxygen atoms are missing along the body diagonals of *b* sites and face diagonals of *d* sites. These oxygen vacancies (V_O) act as doubly ionized donors and contribute two electrons to the electrical conductivity [88].

Furthermore, in the case of ITO, In_2O_3 is doped with tin cations which have a smaller ionic radius than indium. Thus, tin (Sn^{4+}), having a valancy of four, replaces indium (In^{3+}) of valancy three inside the In_2O_3 structure and provides one extra electron to the conduction band [89].

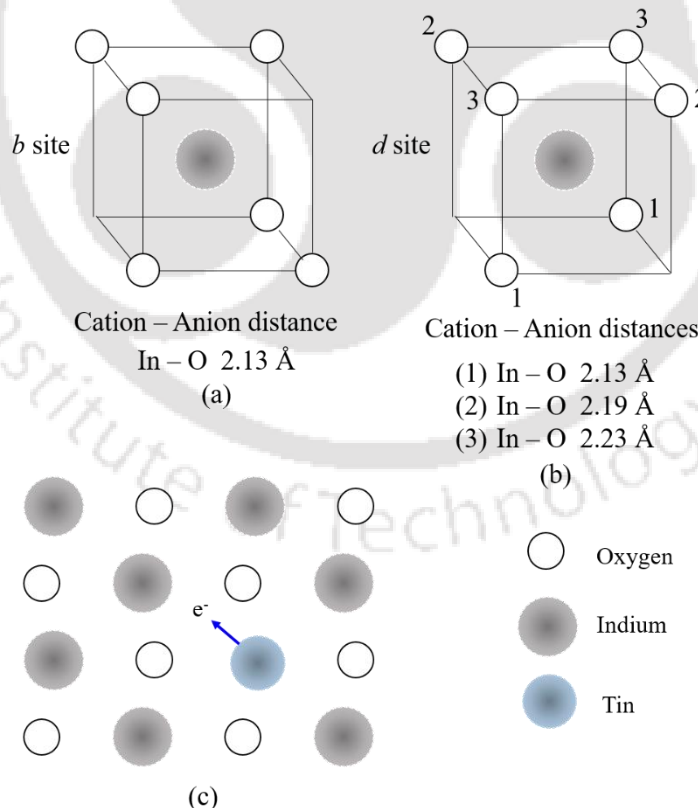

Figure 1-4. In_2O_3 crystal structure: Schematic of the (a) b site, and (b) d site. (b) Schematic of the tin doping sites at In_2O_3 crystal.

TH-2572_156121026

A perfect understanding of electronic band structure is necessary to get a good insight into the interplay between optical and electrical properties of the ITO thin films. Fan and Goodenough have provided a simple description of otherwise complex ITO band structure based on their electron spectroscopy for chemical analysis (ESCA) and X-ray photoelectron spectroscopy (XPS) data [90]. In their band structure model, as shown in Figure 1-5. it was proposed that In_2O_3 has a filled O^{2-}:$2p^6$ valance band, and the core In: 3d band lies right below the valance band edge E_v. In: 5s conduction band with band edge, E_c lies about 3.5 eV above E_v. This energy gap is called a bandgap. The Fermi energy E_f is very close to the conduction band edge. The next higher band is In: 4d band. Now, in the case of ITO for low tin doping concentration, the donor level (Sn^{4+}) and impurity levels (V_O: oxygen vacancies) lie just below conduction band edge E_c. The Fermi level lies in between E_c and impurity levels. For very high doping concentration, both donor and impurity levels merge with the conduction band, forming a ‘‘degenerate’’ type semiconductor. In this way, if the doping concentration keeps on increasing, electrons in the lower states of conduction bands will “block” these states resulting in a bandgap broadening, an effect known as the Burstein-Moss shift [91].

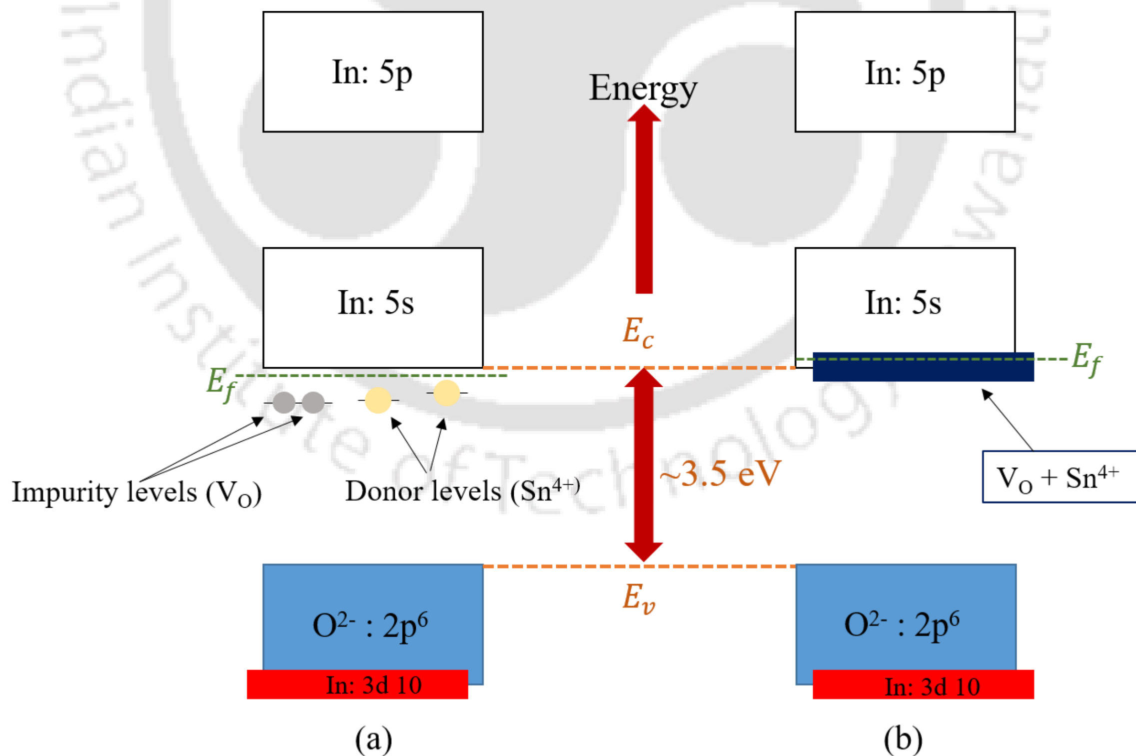

Figure 1-5. Schematic of the band structure of ITO: (a) low doping levels; (b) high doping levels (Burstein-Moss effect).

TH-2572_156121026

1.5.2 SPR studies in ITO thin films

Over the years, SPR in ITO has been demonstrated experimentally in several excitation geometries like prism-based K-R [92] and Otto configurations [93], fiber optics [41], and gratings [94]. But, we will be focusing on the work done SPR via K-R geometry for this short literature survey. The first-ever experimental demonstration of SPR was given by Rhodes *et al.* in the year 2006 [92]. Using K-R geometry, they demonstrated SPR spectra for wavenumber ranging from 4200 cm^{-1} (0.52 eV) to 10 000 cm^{-1} (1.24 eV) and for incident angles 40° - 70°. They compared the SPR effect in ITO to that of gold to show that the farmer one is advantageous for the study of SPs and can also be used to directly observe the plasma frequency (ω_p), which is not possible in gold due to interband transitions. Two years later, the same group explored the film thickness dependency of SPR in ITO thin films deposited by the rf-magnetron sputtering method [95]. Film thickness-dependent plasmon excitation was divided into two categories: for low thickness, i.e., up to 80 nm, the excitation is governed by screened-bulk plasmon (SBP), a one-dimensional excitation that is responsible for charge transfer across the films and does not show any incident angle dependency. For thicknesses greater than 80 nm, ITO films exhibit SP excitation, and its wavenumber and angular dependency are analogus to that of noble metals. In another interesting work, Kim *et al.* compared the SPR response of pulsed laser deposited ITO (PLD-ITO) thin films with that of AZO and GZO thin films at the telecommunication wavelength (1.55 μm) and observed more intense resonance response in case of ITO thin film as compared to other two TCOs [96]. This increased intensity was attributed to the higher imaginary part of permittivity in the ITO thin film. The effect of metal seeding on the SPR properties of the ITO thin films is also studied by Chen *et al.* for Ag-ITO co-sputtered thin films [97].

1.5.3 Concept of epsilon-near-zero thin films and ITO as an epsilon-near-zero material

Most of the reports on SPR properties of alternative plasmonic materials are focused on validating these materials as credible replacements of noble metals for plasmonics applications. However, Khurgin showed that the noble metals are still preferable over the

TH-2572_156121026

alternative plasmonics materials when it comes to application domain requiring higher propagation constants and field enhancements [98]. He compared the figure of merit (FOM) of noble metals to that of semiconducting materials and established that noble metal has higher FOM values over the wavelength region of interest. The vibrant promises of alternative plasmonic materials are yet to be realized on device-level because of these constraints. However, in-depth research in this field has given rise to a new branch of nanophotonics: *epsilon-near-zero photonics* [99]. Though the concept of *epsilon-near-zero* (ENZ) was there in the case of metamaterials from the year 2004 [100], it gained considerable momentum due to the realization of extraordinary merits of TCOs as ENZ material. Vanishingly small dielectric permittivity values of TCOs near ENZ wavelength, the wavelength at which the real part of permittivity crosses zero, has led to many unprecedented phenomena like ultra-fast all-optical switching [101, 102], giant optical nonlinearity [103, 104], perfect absorption (PA) [105, 106], super-coupling [107, 108], optical time reversal [109], and so on. The EMR in such ultra-thin films required for ENZ applications comes from a capacitive-like plasmon, i.e., different from SPs in a way that the opposite charges develop on either side of the thin conducting films as opposed to the charges developed across the length of the film in the case of SPs. The perpendicularly polarized resonance related to these capacitive plasmons (CPs) was first designated as *capacitive plasmon resonance* (CPR) by Franzen *et al.* [110]. Nowadays, however, the CPR occurring at the vicinity of ENZ wavelength has been termed as *ENZ plasmon resonance* [102, 111] due to the existence of near-zero-valued dielectric constant between the two parallel plates of the capacitor. This terminology is followed throughout the thesis to describe the EMR effect in ITO thin films.

PA of electromagnetic waves is one of the most intriguing applications of ENZ materials from the standpoint of fundamental physics. PA also has many game-changing applications, such as bolometers [112], plasmonic sensors [113], light-harvesting [114], and hot electron photodetection [115]. Luk *et al.* provided the first experimental demonstration of PA in ENZ ITO thin films of various thicknesses excited via K-R geometry [105]. They were able to achieve PA in ITO thin film of thickness as low as 24 nm, for which the single-pass attenuation was only 5%. A very high degree of electric field enhancement in the vicinity of the ENZ wavelengths was established as the main reason behind such a high value of absorption in ultra-thin ITO films. Broadband PA was also realized experimentally by Yoon

TH-2572_156121026

et al. over the NIR region (wavelength range of 1450 - 1750 nm) for a three-layer ITO film [106]. Each film had different degrees of free carrier concentration, thus different ENZ values. In another interesting study, Anopchenko *et al.* presented as high as ~20% tunability of PA wavelength in ITO-TiO_2-Au structure, employed in K-R geometry, by changing the electrical bias voltage from 0 to 5 volt [116].

1.5.4 LMR studies in ITO thin films

The first-ever experimental demonstration of fiber optics refractive index sensor based on the LMR phenomenon was given by Del Villar *et al.* in ITO thin films [41]. They also showed multiple resonance bands experimentally for a higher film thickness of 440 nm. This study elevated LMR as a promising candidate for resonance based sensing application, a field dominated solely by SPR at that time, and prompted a sea of studies afterward exploring both application domain and fundamental aspects of the LMR phenomenon [6, 43, 47]. In 2015, Del Villar *et al.* presented the first successful experimental study on LMR excitation of ITO thin films via K-R geometry [44]. They achieved this using an all-side-polished prism, as described in section 1.2. Later, the same group experimentally demonstrated refractive index sensing of LMR for ITO thin films [117]. Using a slightly modified K-R geometry (usage of an all-side-polished prism), they were able to achieve RI sensitivities up to 700 nm/RIU and 1200 nm/RIU for TE and TM polarization, respectively. However, the majority of LMR studies are done using optical fibers due to the critically low LMR intensity and RI sensitivity of the thin film counterpart.

1.6 Pulsed laser deposition technique for ITO thin films

Over the years, ITO thin films have been deposited using several deposition techniques, like radio frequency (RF) magnetron sputtering [118], pulsed laser deposition (PLD) [119], electron beam evaporation [120], atomic layer deposition (ALD) [121], and spray pyrolysis [122]. Amongst this abundance of deposition techniques available, PLD is experimentally simple on one side and conceptually fascinating on the other [123]. Though the first report on the deposition of thin films via PLD can be dated back to the year 1965 [124], the real potential of PLD was recognized by the broader scientific community after the successful depositions of high-temperature (high-T_c) superconductors in the late 1980s [125, 126]. Ever since PLD has been used to deposit high-quality thin films of complex oxides, sulfides, nitrides, metallic

TH-2572_156121026

thin films, perovskites, 2D materials, etc. [127, 128]. PLD is a consequence of the *pulsed laser ablation* (PLA) process, in which a high-power laser light is focused onto a target to cause ablation of the target material [129]. After PLA, a plasma plume containing target constituents like neutral atoms, ions, molecules, etc., gets deposited onto a heated substrate that is kept at a distance of 3 to 10 cm apart [123]. The characteristics of the deposited thin films depend upon several parameters associated with the PLD process, such as laser wavelength, laser fluence, target-to-substrate distance, substrate temperature, presence of ambient gas (i.e., type of gas and the gas pressure) in the chamber, and so on [130]. PLD offers some unique advantages over other deposition techniques, namely, deposition from highly energetic beam having initial velocities $\geq 10^6$ cm^2/sec, the ability of congruent transfer of target constituents, the capacity of reactive deposition in gas ambient, and the ability to deposit multilayer thin film in a single step [123]. However, PLD also from suffers some inherent drawbacks such as non-uniformity of thin films, generation of big-sized particulates, the appearance of re-sputtering, and surface defects due to the highly energetic plasma plume [123].

Kim *et al.* in 1999 studied the effect of substrate temperature, oxygen pressure and tin concentration on the electrical optical and structural properties of the pulsed laser deposited (PLD-ITO) thin films [131]. As suggested earlier, the background gas type plays a crucial role in determining the optical, electrical, structural, and morphological properties of any pulsed laser deposited thin films. Apart from O_2, gases like nitrogen (N_2), helium (He), argon (Ar), and xenon (Xe) [132, 133], has been used inside the PLD chamber to achieve nanostructures and other important properties in ITO thin films. However, in a very interesting work, Perrière *et al.* showed that PLD of ITO thin films in a high vacuum environment leads to the formation of In or In-Sn nanoclusters embedded in a pure ITO matrix [134]. They also demonstrated that these metal-rich ITO films show a superconducting transition near 8 K due to the presence of metallic indium. Millon *et al.* pinpointed oxygen vacancies as the root cause of this phase separation [135]. They showed that the additional electrons generated by oxygen vacancies act as reduction centers to induce the development of metallic nanoclusters.

In the context of ENZ, Naik *et al.* demonstrated that crossover frequency could be tuned efficiently by changing the tin dopant concentration for PLD-ITO thin films [136]. Fang *et al.* achieved tuning of crossover wavelength over the entire NIR range (1270 nm – 1930 nm) by changing the oxygen partial pressure and substrate temperature ITO thin films deposited via

TH-2572_156121026

PLD [137]. In a similar vein, Xian *et al.* were able to tune the ENZ wavelength from 1564.7 nm to 1392.8 nm by lowering the oxygen pressure from 30 Pa to 10 Pa [138]. However, to the best of our knowledge, there are no studies performed in LMR when it comes to films deposited via PLD.

1.7 Motivation

All the studies on ENZ-ITO thin films are mainly focused on the wavelength tuning aspects of the ENZ property. However, a systematic study linking the ENZ plasmon resonance of PLD-ITO thin films to the tunability of ENZ wavelengths is still missing from the literature. Also, most of the PLD parameters are not yet being utilized in the context of ENZ properties of ITO thin films. The use of different ambient gases inside the deposition chamber is an enthralling prospect that can effectively tune oxygen vacancies, and thereby, directly controlling the ENZ wavelengths.

The optical properties of vacuum-deposited indium-rich ITO thin films are hardly being analyzed in the literature. This is probably because of bigger particulates, which resulted in a very high degree of surface roughness in such films [134]. Though the surface roughness has been studied quite extensively in the case of SPR [139-144], there is no such report exploring the surface roughness effect on ENZ plasmon resonance. All these reports on SPR response of metallic thin films focused on understanding the effect of surface roughness in the visible and/or near-infrared spectrum range, where both the amplitude of real and imaginary part of permittivity is much greater than one. But this situation is drastically different in ENZ material, whose main recipe is that it has a significantly small permittivity value [99]. Thus, the necessary approximations on permittivity that goes into the derivations related to the surface roughness effect on the metallic films is not be applicable here. Experimental studies on surface roughness-modified ENZ modes could reveal fascinating physical insights into this exciting field. Such an eye-catching prospect gives motivation for the study of the effect of the increasing surface roughness on the ENZ modes.

As discussed in the earlier sections, fiber optics has dominated LMR research due to its superlative intensity and sensing response compared to thin film geometries. The LMR absorption intensity depends upon the extinction coefficient; the higher the extinction coefficient, the better the LMR intensity for a particular material [145]. But the problem with

TH-2572_156121026

dielectric materials used for LMR excitation is that it has low extinction coefficient values. An adequate amount of metal doping in dielectric material can solve this problem through enhanced the extinction coefficient values coming from the metal interbands. Vacuum-deposited ITO thin films with the pre-existing metallic indium phase could provide a single-step solution to the LMR intensity problem without any external metal doping requirement.

Film thickness plays a crucial role in determining cutoff conditions for the modes to be guided inside the thin film waveguides, thereby dictating the generation of LMR [6]. The effect of film thickness on the LMR response has been well documented both numerically [145] and experimentally [51] in the case of fiber optics. However, there is no such report exploring the film thickness dependency of thin film based K-R geometry. This particular gap in the literature motivates the study of the effect of film thickness in vacuum-deposited ITO thin films.

1.8 Organization of thesis

In this present thesis, the effect of different gas ambient on the ENZ plasmon resonance properties of PLD-ITO thin films is studied systematically through experimental and numerical analysis. However, a randomly rough film surface with a very high degree of surface roughness was observed for the films deposited at high vacuum conditions. In this context, the effect of increasing surface roughness on the ENZ plasmon resonance has been explored in vacuum-deposited metallic indium-rich ITO films. Additionally, PA is demonstrated for the film with the highest surface roughness value as an application of ENZ plasmon resonance study. In the second half of the thesis, LMR spectra of vacuum-deposited metallic indium-rich ITO, generated via simple K-R geometry, have been compared experimentally and numerically with the films deposited in other ambient conditions. The effect of overall thickness (film + surface roughness) on the LMR properties of metallic indium rich ITO thin films is also studied in detail. Further, refractive index sensing has been presented as an application of the LMR.

The overall thesis work is organized in seven chapters as follows:

Chapter 1: "Introduction" **Introduction** contains a detailed literature survey on the importance of the ITO as a technologically important material, its properties, along with motivation and objective of the present work. The theory and importance of ENZ modes and LMR in connection with the PLD-ITO thin films are outlined.

TH-2572_156121026

Chapter 2: "Experimental Details, Characterization techniques and Description of Numerical Framework" describes the PLD technique used for deposition of ITO thin films and experimental details of different characterization tools like spectroscopic ellipsometry, XRD, AFM, FESEM, Uv-Vis-NIR spectroscopy, four probe, and Hall measurements are also presented. Spectroscopic ellipsometry has been discussed in detail in the context of optical characterization of ITO thin films. It also presents an overview of the numerical framework which is used for simulating the experimental reflection spectra corresponding to ENZ plasmon resonance and LMR.

Chapter 3: "Ambient Condition Dependent ENZ Plasmon Resonance Properties of PLD ITO thin films" explores the tunability of ENZ properties of PLD ITO thin films deposited at different ambient conditions; namely, O_2, N_2, Ar, and He. Local electric field enhancement in connection to the absorption intensity is also discussed for a better physical understanding of the resonance effect.

Chapter 4: "Effect of Surface Roughness on the ENZ Plasmon Resonance Properties of Vacuum-deposited ITO films and Demonstration of PA as an Application" discusses the effect of increasing surface roughness on the ENZ plasmon resonance of vacuum-deposited randomly ITO films. In addition to this, near-perfect absorption has been demonstrated as an application of ENZ phenomena.

Chapter 5: "Ambient Condition Dependent LMR response of PLD ITO thin films" presents an elaborate discussion on the LMR properties of ITO thin films deposited at different ambient conditions of PLD chamber.

Chapter 6: "Thickness Dependency of LMR response in Vacuum-deposited ITO Thin Films and Exploration of Refractive Index Sensing as an Application" investigate the role of overall film thickness on the LMR properties of the vacuum-deposited ITO thin films. Refractive index sensing properties have been studied in this context by mixing water and glycerol at different weight percentages.

Finally, in **Chapter 7, *"Conclusion and Future Scope"***, the salient features of the present work are summarized, and future scope of the work are highlighted.

TH-2572_156121026

Chapter 2

Experimental Details, Characterization Techniques and Description of Numerical Framework

The current thesis work is mainly focused on exploring the ENZ plasmon resonance and LMR properties of the ITO thin films by both experimental and theoretical means. The deposition of ITO thin films is carried out using PLD technique. As discussed in Chapter 1, PLD offers several advantages over other deposition techniques. In the present work it is also shown that PLD is capable of depositing metallic indium-rich ITO thin films in a single deposition cycle, i.e., without the use of any secondary procedures. Though LMR and SPR were studied experimentally as well numerically in the case of thin film based K-R geometry [44], the requirement of a custom-made all-side-polished prism could potentially increase the experimental cost significantly. Keeping this in mind, the studies on ENZ plasmon resonance and LMR are performed in a simple K-R geometry that does not require any specialized prism. The ITO thin films deposited via PLD have considerable surface roughness. However, the integration of the effect of the surface roughness into simple numerical simulation algorithms like the transfer matrix method (TMM) is rarely being discussed in the literature. In this work, a modified TMM, which takes into account the surface roughness of the films through the application of the anisotropic Bruggeman effective medium approximation (ABEMA), is developed to realize the experimental ENZ plasmon and LMR spectra numerically. Additional characterization techniques are also required to support the analysis of ENZ plasmon resonance and LMR properties of PLD-ITO thin films. The optical properties of the ITO thin films are studied with the aid of spectroscopic ellipsometry (SE) and Uv-Vis-NIR spectroscopy. X-ray diffraction (XRD) is used for crystallographic phase analysis of the films, while surface morphology is visualized using atomic force microscopy (AFM) and field emission scanning tunneling microscopy (FESEM) measurements. The electrical properties of the PLD-ITO thin films are studied with the help of Four probe and Hall measurements.

TH-2572_156121026

This chapter presents the experimental details of the setups used for the deposition of ITO thin films, ENZ plasmon resonance, and LMR spectra measurement. All the additional characterization tools used for analyzing the ITO thin films are also discussed. The chapter also contains the details about the modified TMM method which is being used for numerical analysis of PLD-ITO thin films throughout the thesis work.

2.1 Thin Film Deposition

Overall thin film deposition procedure in the case ITO films deposited via PLD can be divided into three categories: ITO target (pellet) preparation, cleaning of corning glass substrate before deposition, and finally, deposition using PLD set up. All these procedures are discussed in great detail in the subsequent sections.

2.1.1 Preparation of ITO target

10 wt.% SnO_2 doped ITO pellets were prepared from the mixture of commercially available In_2O_3 powder (Alfa Aesar, purity 99.9%, -325 mesh) and SnO_2 powder (Alfa Aesar, purity 99.9%, <10 µm powder) via solid-state synthesis route. The entire pellet preparation procedure is shown in Figure 2-1. First, a mixture of 3.5695 gm. of In_2O_3 powder and 0.4305 gm. of SnO_2

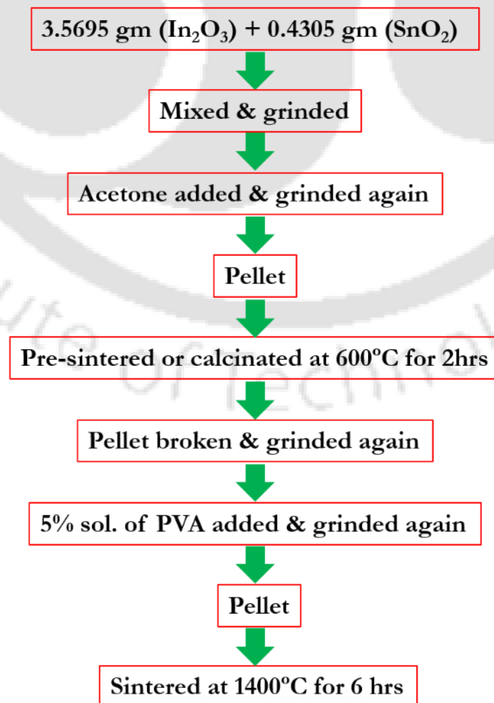

Figure 2-1. Step-by-step procedure of preparation of ITO pellet via solid-state synthesis method.

TH-2572_156121026

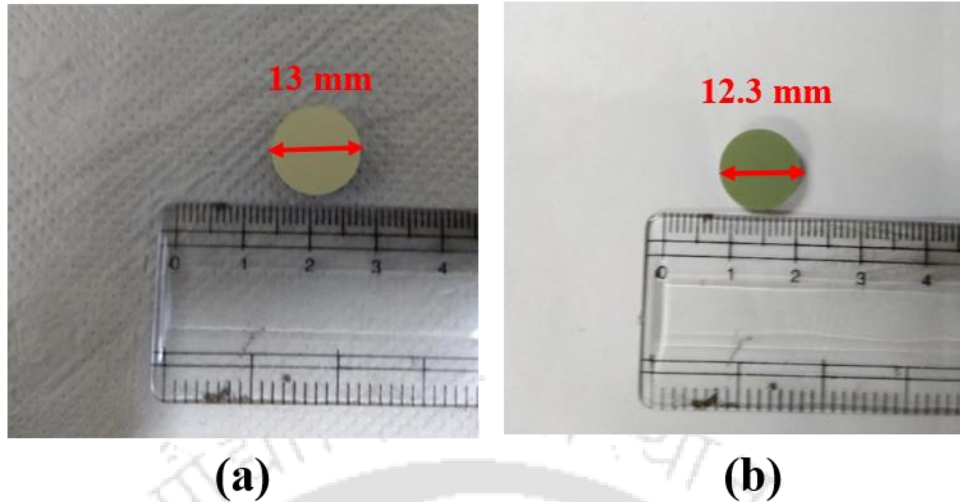

Figure 2-2. Photographs of ITO pellet (a) before sintering or pre-sintering, (b) after final sintering. A scale is shown below the pellet for size comparison.

powder was grinded continuously for 4 hours with the help of mortar and pestle. The weight measurement of the powders was done in a high-precision weighing machine (Model: *AG135*; Make: *METTLER TOLEDO*) which is capable of measuring weight as low as 0.1 mg. During this grinding process, a small amount of acetone was mixed to get a homogeneous mixture. Now, these finely grinded powders were pressed into a form of dense pellets by applying a pressure of ~ 35 kg/cm^2 in a laboratory-grade hydraulic press (KBr Press M-20). Pellets were calcinated (pre-sintered) at 600°C in the air for 2 hours to achieve dewaxing. Pre-sintered pellets were broken into the form of fine powder and grinded again for some time, but this time by mixing 5wt% solution of polyvinyl alcohol (PVA), an organic binder. Finally, pellets were prepared and sintered for 6 hours in air at 1400°C temperature to obtain the final product. Figure 2-2 shows the photograph of ITO pellets before and after the sintering procedure. It can be seen that an unsintered pellet of diameter 13 mm shrinks to a pellet of diameter 12.3 mm after sintering due to the chemical reaction between the In_2O_3 and SnO_2 powders. This indicates that the sintered pellets are more compact than the unsintered pellets and could be used as a target in the PLD setup.

2.1.2 Substrate cleaning

In this work, ITO thin films were mainly deposited onto corning glass (Eagle XG) substrate. Corning glass was chosen over the transparent substrates like quartz, sapphire and MgO due to its environment friendly (no heavy metals) nature and lower price. Before

TH-2572_156121026

introducing the corning glass substrates (0.7 × 15 × 15 mm) to the PLD chamber, they were first cleaned thoroughly in distilled water and then cleaned ultrasonically for 20 min each in acetone and 2- propanol, respectively. Finally, the substrates were blow-dried in the flow of pure N_2 gas (purity: 99.999%), which is kept at a pressure of 130 to 140 kg/cm^2 under a metal cylinder of volume 47 liters.

2.1.3 PLD setup

PLD is one of the most versatile technique among the various available physical vapor deposition (PVD) techniques. Pulsed laser ablation (PLA) process is at the heart of the PLD technique. PLA process starts within a target material when a high-power laser beam is focused onto target with an energy density that is beyond the ablation threshold of that particular material. Several events occur after the interaction of the laser pulse with the target material [123]. First, after interaction with a ns pulse, rapid heating and vaporization of the target takes place. Next, absorption of the incident laser energy by the vapor species increases until breakdown occurs and a highly dense plasma is formed. The absorption of remainder of the laser pulse energy subsequently heats up and accelerates the nascent plasma. Plasma plume contains molecules, neutral atoms, ions, electrons, etc. This plasma plume expands in vacuum or ambient gas environment forming a Knudsen layer in the process. The Knudsen layer, formed due to the collisions atoms and ions, modifies the velocity distribution of the plasma plume to drifted Maxwellian with the direction of propagation along the normal to the target surface [146]. Thereby, the PLA process results in a highly directional plasma plume traversing away from the target surface initial velocities $\geq 10^6$ cm/s. The presence of background gas inside the PLD chamber generally serves three purposes [130]: the slowing down of plasma plume; reduction in number and modification of size and shape of the ejected particulates; controlling the oxidation/nitrogen state in the case of oxide/nitride materials. Plasma plume forms a shock wave font in the presence of gas of background due to the compression of vapor species [147]. Thereafter, gradually slowed down plasma plume gets deposited onto a heated substrate kept a distance 3 cm to 10 cm away from the target. Film growth and nucleation process of PLD-grown thin films can be divided into three categories [130]: (i) Volmer–Weber or 3D island growth, (ii) Frank–van der Merwe or 2D full-monolayer growth, and (iii) Stranski–Krastinov growth in which two dimensional growth followed by the 3D island

TH-2572_156121026

growth. The selection of the growth process to be followed in PLD depends upon the thermodynamics relating film and substrate surface energies, and the interface energy of film-substrate.

The deposition of the ITO thin films was carried out in an *in*-house PLD chamber. Figure 2-3 and Figure 2-4 depict the schematic and the actual experimental setup of PLD, respectively. Basically, all the important reactions related to the PLD take place in an ultra-high vacuum compatible stainless steel chamber of diameter 12 inches. The PLD chamber is custom-made by *EXCEL INSTRUMENTS* to allow the assembling of the vacuum evacuation unit, pressure gauge unit, target carrousel unit, substrate holder, laser beam entering port, and the reactive gas inlet port. There are also some extra ports dedicated to the monitoring and observation of the plasma deposition processes. The target carrousel, capable of controlling six targets simultaneously, is loaded through a 150 CF port. Rotating and rastering of targets can

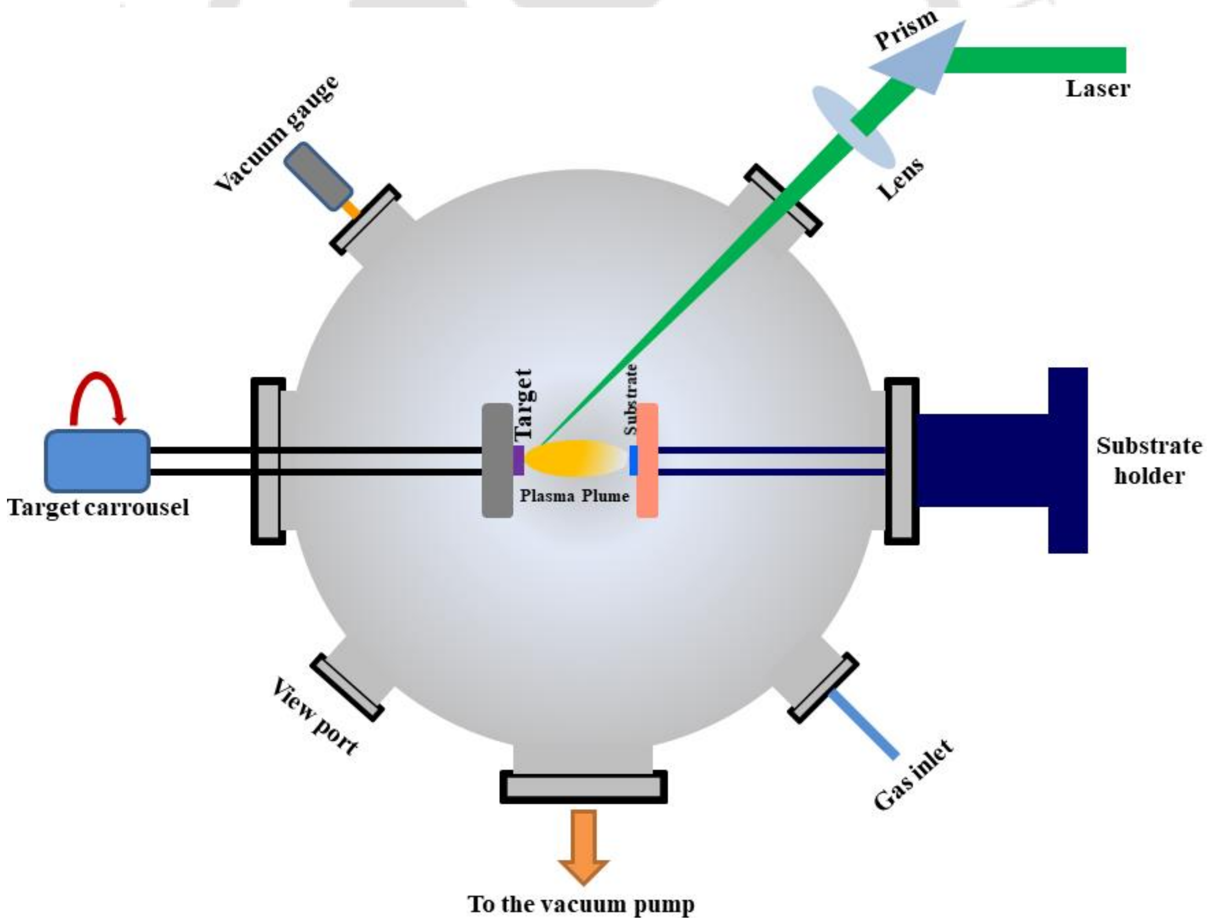

Figure 2-3. Schematic diagram of the PLD setup.

TH-2572_156121026

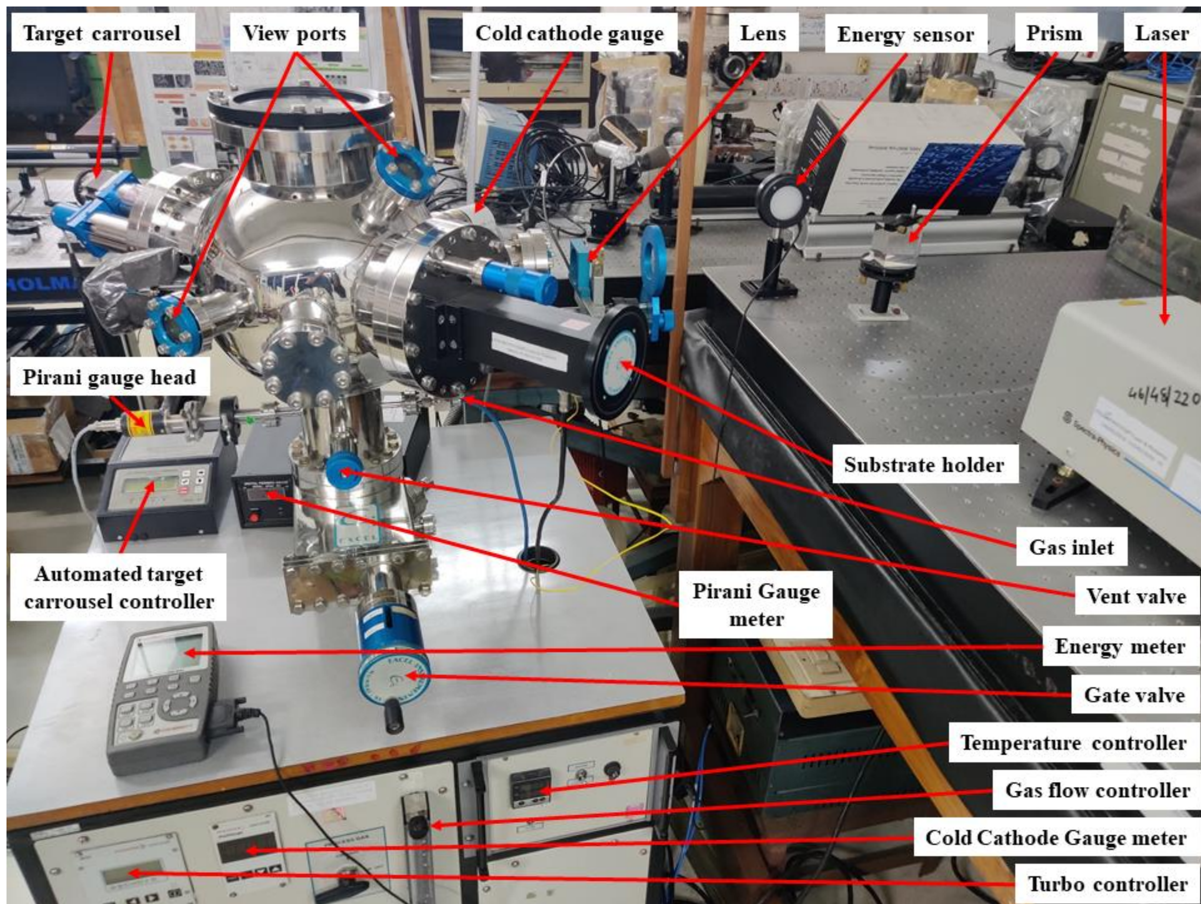

Figure 2-4. Photograph of the in-house PLD setup.

be controlled by an automated target carrousel controller unit (Model: *ATCC – 101*; Make: *EXCEL INSTRUMENTS*). A substrate holder unit is attached to another 150 CF port just opposite the target carousel unit. One or two substrates can be loaded to the substrate holder, depending upon the requirement. The height of the substrate from the base of the substrate holder and hence the target-to-substrate distance can be changed efficiently with the help of the screws attached to the four pillars of the substrate holder. The target-to-substrate distance was fixed at 3.5 cm for all the depositions in the current scenario. A 1.5-inch heater with an embedded K-type thermocouple is connected with the substrate heater enabling step-wise control of the substrate temperature up to 800°C. In the current work, however, the substrate temperature was fixed at 400°C through the duration of the deposition. After the deposition, the substrate temperature was kept at 400°C for another 40 min in order to achieve annealing of the sample. In addition to this, heating and cooling rates were also maintained at 6°C/min and 4°C/min, respectively.

TH-2572_156121026

Before the start of the deposition process, the PLD chamber was evacuated to a high vacuum level using a turbomolecular pump (Model: *Hi pace 300 C*; Make: *Pfeiffer vacuum*) which is backed by a rotary vane pump (Model: *DUO 10 MC*; Make: *Pfeiffer vacuum*). This dual-pump assembly is connected with the PLD chamber through a gate valve, closing which the PLD chamber can be disconnected completely with the whole pump assembly. The pressure level inside the chamber is measured by two different pressure gauges working at two distinct vacuum levels. For higher pressure levels, i.e., $10^3 – 10^{-3}$ mbar, a Pirani gauge (Model: *DHPG - 011*; Make: *KM V Vacuum Technologies)* is used, while the lower pressure level ($10^{-2} – 10^{-7}$ mbar) is measured by a cold cathode gauge (Model: *IKR 251*; Make: *Pfeiffer vacuum*). The PLD chamber was evacuated to a base pressure of 2×10^{-5} mbar before each deposition cycle. In the case of ITO thin films deposited under high vacuum ambient, this 2×10^{-5} mbar pressure is maintained throughout the deposition cycle. Background gases could be purged into the chamber through a gas inlet port. This port is connected with four cylinders containing 99.999% pure O_2, N_2, Ar, and He gases via 6 mm OD × 4 mm ID polyurathene pneumatic PU tubes. The gas pressure inside the chamber can be controlled by a gas flow controller. The gas pressure is maintained at 0.05 mbar for the deposition of ITO thin films under a gaseous environment. After the whole deposition process is over, the vacuum inside the chamber can be released by using a vent valve.

Finally, a *Q*-switched Nd:YAG laser source (Model: *Quanta-Ray INDI-HG*; Make: *Spectra Physics;* wavelength - 532 nm, repetition rate - 10 Hz, pulse width - 8 ns) was used to facilitate the ITO deposition process. A high-power laser beam coming from the externally placed laser source enters the PLD chamber through a glass window after deviating at an angle of 90° via a high damage threshold fused silica prism. A laser pulse of energy 40 mJ (as measured by the energy meter (Model: FIELDMAXII-TOP; Make: *COHERENT*)) was focused onto the ITO pellet by a lens of focal length 35 cm to obtain a fixed fluence value of 5 J/cm^2. The energy of the laser was monitored cautiously throughout the deposition process. In the current thesis work, two types of deposition processes were performed. One deposition was carried out in the presence of O_2, N_2, Ar and He gas. The deposition time was varied in such a way that the overall thickness (film + surface roughness) of the ITO thin films remained constant in all such background gases. Other deposition was carried out at high vacuum and the different properties were compared to the films deposited under various gaseous

TH-2572_156121026

environments. The deposition time for the vacuum-deposited ITO thin films was varied to explore the effect of overall film thickness over the ENZ plasmon resonance and LMR properties.

2.2 Characterizations Techniques

Various characterization techniques were used over the PLD-ITO thin films in order to study the structural, morphological, topological and optical properties of the deposited thin films. The following subsections report the detailed specifications of all these characterization techniques.

X-ray diffraction (XRD): A high power XRD (Model: *SmartLab*; Make: *Rigaku*; power 9 kW, Cu Kα radiation at $\lambda = 0.154056$ nm) operated at glancing angle mode (incidence angle fixed at 1°) was applied to study the structural properties of the PLD-ITO thin films. XRD Data was recorded in the diffraction angle range of 10º to 70º at a step of 0.02º and the scan speed was 3º/minute. After loading the thin films inside the XRD chamber, the height corrections and angle correction algorithm was run in the XRD instrument software to nullify the effect of the substrate. The crystallographic phase analysis of the samples was carried out by performing a Rietveld refinement operation over the XRD data through an open-sourced *FullProf Suite* software.

Field emission scanning electron microscope (FESEM): Surface morphologies of all the films were characterized by field emission scanning electron microscope (FESEM) (Model: *Sigma 300*; Make: *Zeiss*) operated at a fix electron high tension (EHT) value of 3 kV. Before introducing into the FESEM instrument, ITO thin films were gold-coated using a sputter coater. The working distance of the electron gun was varied from 2 mm to 4 mm depending upon the quality of the images.

Atomic force microscopy (AFM): Atomic force microscopy (AFM) (Model: *Cypher*; Make: *Oxford*) was employed for morphological as well as topological characterization of the PLD-ITO thin films. The measurement was done over a surface area of 5 × 5 μm by utilizing the non-contact or tapping mode of the AFM. The scan rate was fixed at 1 Hz, and the images were recorded by 512 number of line scans. Thereby, the resolution of each pixel was 3.9 nm. The RMS surface roughness was calculated from these AFM images using an open-sourced software named *Gwyddion*.

TH-2572_156121026

Four-probe measurement: The sheet resistance and the electrical resistivity of the PLD-ITO thin films were calculated by utilizing the four-probe (Model: *DFP-02*; Make: *SES Instruments*) measurement. Current (I) through the four probes in contact with thin film surface was changed from 0 mA to 4 mA at a step of 0.25 mA and the corresponding change in the voltage (V) was recorded. The sheet resistance (R_s) can be calculated from the slope of the linear fitted I-V curve via the relation:

$$R_s = k\left(\frac{V}{I}\right) \tag{2.1}$$

where k is the geometric factor. k is valued at 4.53 for a semi-infinite thin film sheet.

Hall measurement: The carrier concentration (n_e) of the samples was determined by a room-temperature Hall measurement setup which was built *in*-house. Figure 2-5 shows the photograph of the Hall measurement setup. An electromagnet (Model: *EM4-HVA*; Make: *LakeShore*) capable of generating a magnetic field from -0.5 T to +0.5 T was applied to modulate the Hall voltage of the thin films via Van der Pauw geometry. The Hall voltage (V_h) changes with the varying magnetic field (H) were measured by a nanovoltmeter (Model: *2182A*; Make: *Keithley*). First, the Hall coefficient (R) is calculated for a fixed value of source

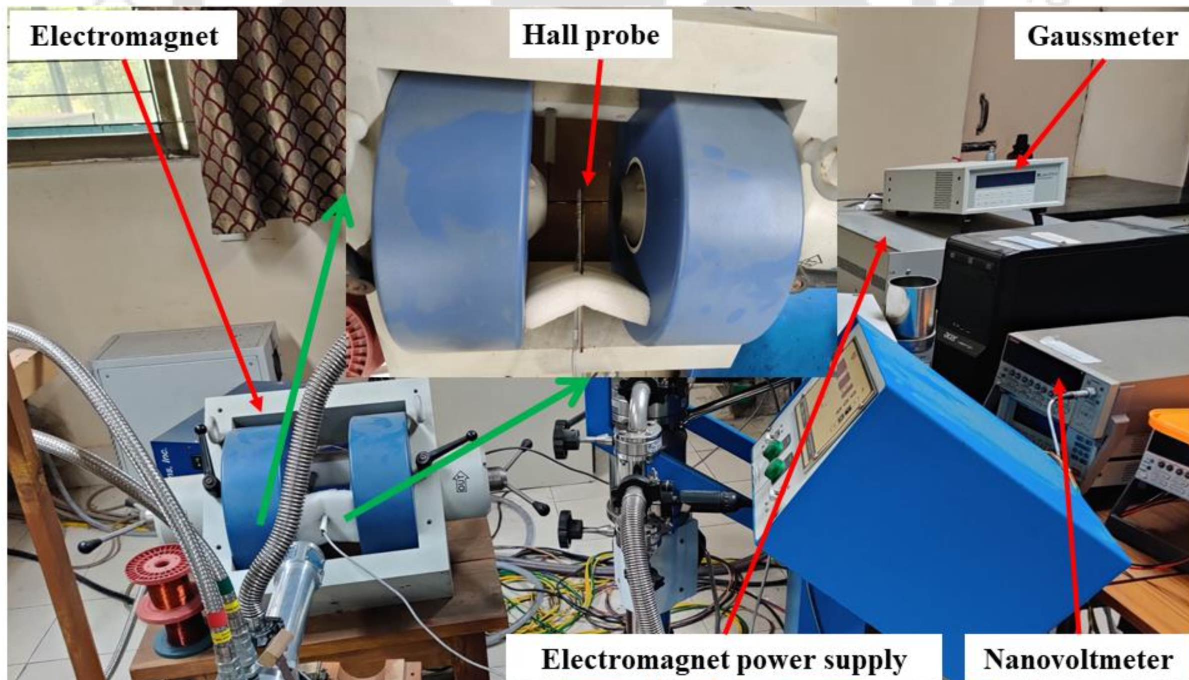

Figure 2-5. Photograph of the in-house Hall measurement setup. Inset of the figure shows the inner view of the electromagnet containing Hall probe inside.

TH-2572_156121026

current (I) using the relation:

$$R = \frac{V_h d}{IH} \tag{2.2}$$

where d is the thickness of the film and $I = 10\ mA$ in this case. Thereby, the carrier concentration (n_e) is given by,

$$R = \frac{1}{n_e q} \tag{2.3}$$

where q is the charge of the electron. The value of electronic charge is 1.6×10^{-19} Coulomb.

UV-Vis-NIR spectrometer: The transmission spectra of the PLD-ITO thin films were collected using a UV-VIS-NIR spectrometer (Model: *Lambda 950*; Make: *Perkin Elmer*). The spectra were recorded over the wavelength of 250 – 2500 with a step size of 1 nm.

Spectroscopic ellipsometer (SE): Spectroscopic Ellipsometry (SE) is a non-destructive tool for the optical characterization of thin films. Figure 2-6 shows the schematic of the SE setup and Figure 2-7 shows a photograph of the actual instrument (Model: *GSE5E*, Make: *SEMILAB*). An unpolarized white light from the Xenon lamp source passes through a polarizer to make it linearly polarized. This linearly polarized light is focused on the sample with of a microscopic doublet lens. For an incidence angle of 75°, the spot size over the sample is 70 × 70 μm. After the interaction with the sample, the change in the polarization state of the reflected light is measured by an analyzer. In wavelength-based interrogation mode, two detec-

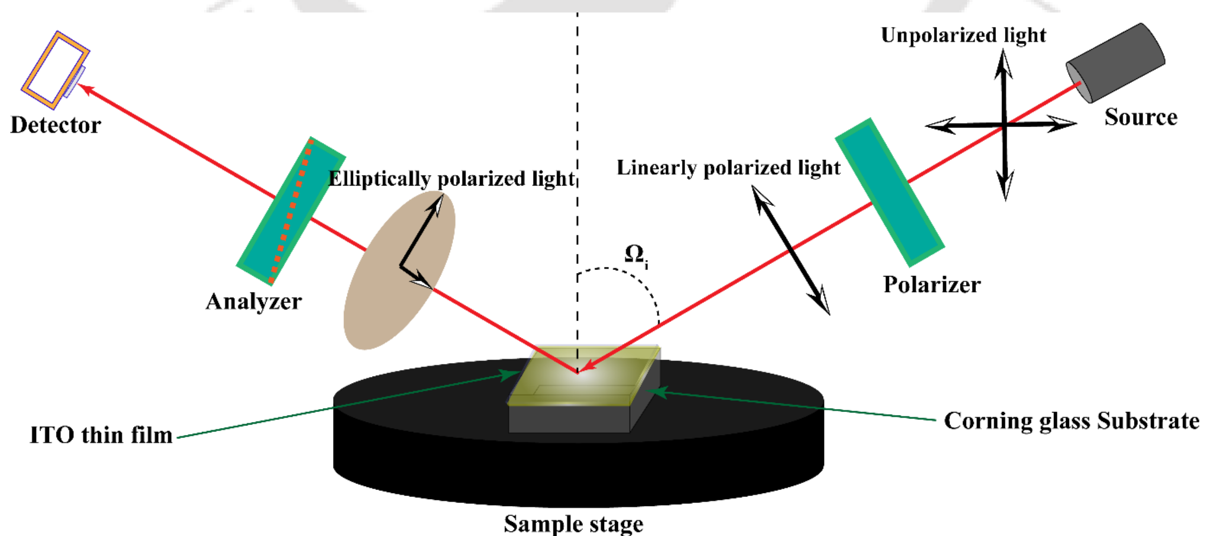

Figure 2-6. Schematic diagram of the SE setup.

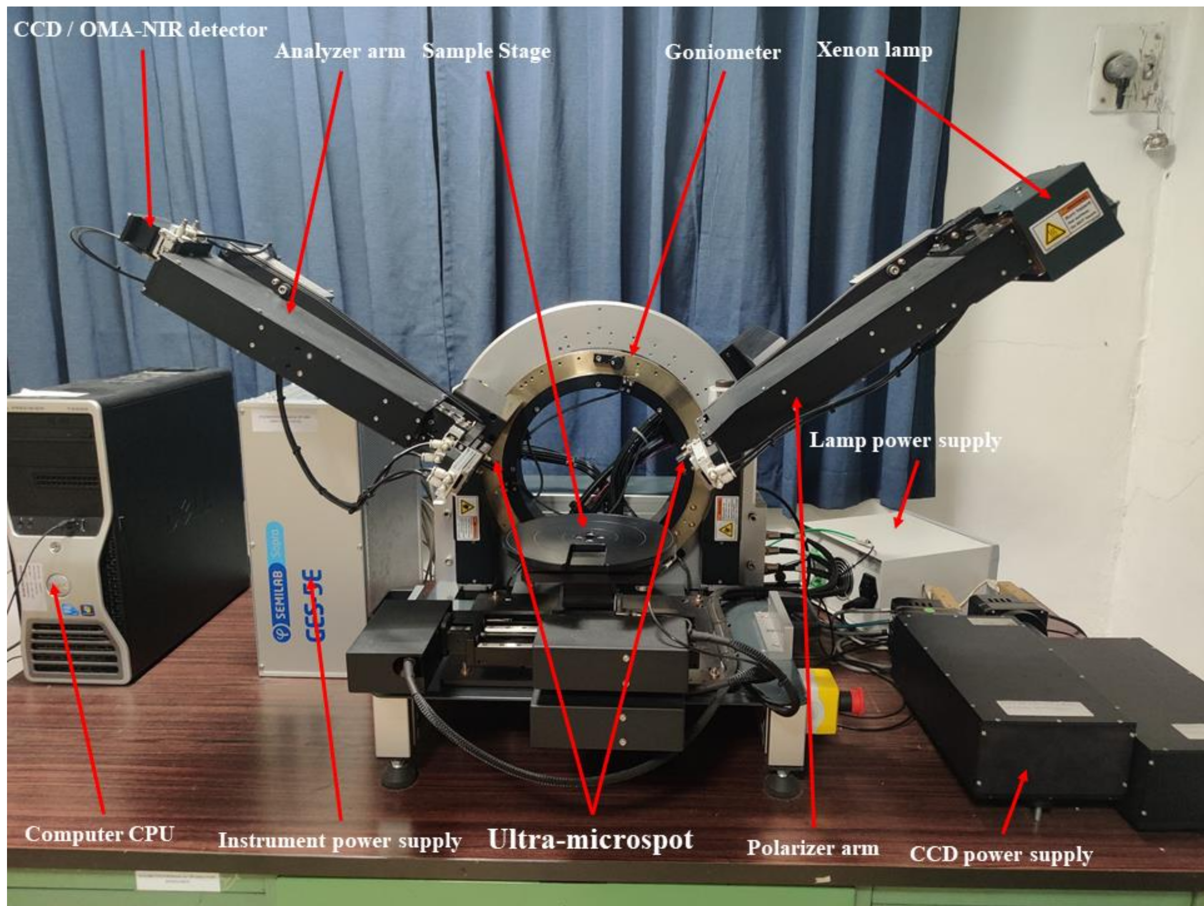

Figure 2-7. Photograph of the SE instrument.

tors are used in tandem to cover the wavelength from UV to NIR range. A charge-coupled device (CCD) and a InGaAs based optical multichannel analyzer (OMA) NIR detectors are being used to cover the wavelength ranges of 172 – 973 nm and 830 – 1706 nm, respectively. The phenomena of change in polarization state and the amplitude of the incident light are used to extract important information like refractive index, dielectric constant, film thickness, roughness, etc., by developing a suitable optical model in the SE analysis software. The measured Ψ and Δ spectra are related to the reflection coefficient along with *s*- or TE- and *p*- or TM- polarization direction via the following relation [148],

$$\rho \equiv \tan\Psi \exp(i\Delta) \equiv \frac{r_p}{r_s} \tag{2.4}$$

where Ψ represents the amplitude ratio between reflection coefficients of *p*- and *s*-polarization, while Δ is the phase difference between these two. Another common representation of SE data is given in terms of pseudo-dielectric function ($\langle\varepsilon\rangle$). The pseudo-

TH-2572_156121026

dielectric function can be related to the optical data ($\Psi - \Delta$ spectra) measured by SE using the following equation [148],

$$\langle \varepsilon \rangle = \varepsilon_a \sin^2 \theta_i \left[1 + \tan^2 \theta_i \left(\frac{1-\rho}{1+\rho} \right)^2 \right] \quad (2.5)$$

where ε_a is the ambient dielectric constant and θ_i is the incident angle of the beam. Since the measurement was performed in atmospheric condition, ε_a is taken as 1. An incident beam at an angle (Ω_i) 60° is used to record the data. SE is basically an indirect method for material characterization. An optical model that has a correct analytical representation of the material to be analyzed must be developed in the spectroscopic ellipsometry analyzer (SEA) software. This software uses a standard regression based Levenberg-Marquardt algorithm [149] to minimize the difference between measured data and fitted data. The figure of merit of SE analysis is given by the root mean square error (RMSE) values, which is defined as [150],

$$RMSE = \sqrt{\frac{1}{2N-m} \sum_{i=1}^{N} \left[\left(\frac{f_{1,meas}^i - f_{1,\text{calc}}^i}{\sigma_{1,meas}^i} \right)^2 w_1 + \left(\frac{f_{2,meas}^i - f_{2,\text{calc}}^i}{\sigma_{2,meas}^i} \right)^2 w_2 \right]} \quad (2.6)$$

where N is the number of data points, m is the number of fitted model parameters, f_{meas}^i and f_{calc}^i are the ith measured and calculated ellipsometric quantities, σ_1^i and σ_2^i are the point-wise experimental errors belonging to the ith f_1 and f_2 measurements, w_1 and w_2 are the user-defined weight factors.

Figure 2-8 shows the layer diagram of the optical model used to fit the ellipsometry data in the wavelength 220 – 1700 nm range. The bottom layer consisting of the corning glass substrate

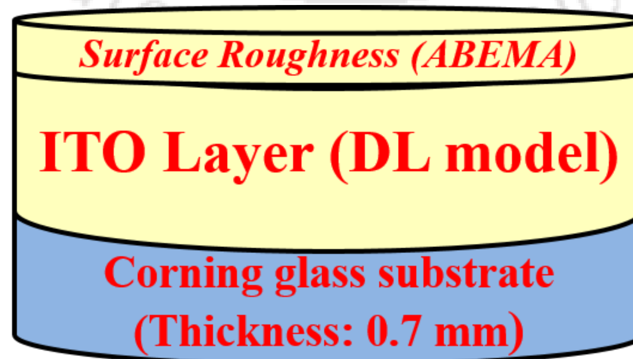

Figure 2-8. Optical layer model used for SE data fitting.

TH-2572_156121026

of thickness 0.7 mm is fitted with the help of the *nk*-file library available in the *SEA v1.0.4* software. On top of the substrate, a pristine layer of ITO is considered. This layer is modeled by a combination of the Drude model and multiple Lorentz oscillators. The Drude model describes the free electron behavior of ITO films [8], while the Lorentz model takes care of the bandgap absorption and interband transitions [148]. The equation for the Drude model is given by [150],

$$\varepsilon_D(E) = \varepsilon_\infty - \frac{\left(\frac{E_P}{E}\right)^2}{1+\left(\frac{E_\Gamma}{E}\right)^2} + i\frac{E_\Gamma}{E}\frac{\left(\frac{E_P}{E}\right)^2}{1+\left(\frac{E_\Gamma}{E}\right)^2} \tag{2.7}$$

where E_p and E_Γ are the plasma energy and the broadening, which is in connection with the scattering frequency and ε_∞ is the high-frequency background permittivity. Drude model can be used to predict electrical conductivity (σ) and the carrier concentration (n_e) of the thin film using the relation

$$\sigma = \frac{\varepsilon_0 E_P^2}{E_\Gamma \hbar} \qquad n_e = \frac{m_e^* \varepsilon_0 E_P^2}{\hbar^2 q^2} \tag{2.8}$$

where ε_0 is the free-space permittivity, $\hbar$ is the reduced Planck's constant, m_e^* is the scalar effective mass of the electrons, and q is the electronic charge. The electrical conductivity (σ) can be used to determine resistivity (ρ_s) and the sheet resistance (R_s) using the relation,

$$\rho_s = \frac{1}{\sigma} \qquad R_s = \frac{\rho}{d} \tag{2.9}$$

where d is the film thickness of ITO thin films determined by SE data fitting. For multiple Lorentz oscillators, the dispersion relation is given by [150],

$$\varepsilon_L(E) = \sum_{j=1} \frac{f_j E_{0_j}^2\left(E_{0_j}^2 - E^2\right)}{\left(E_{0_j}^2 - E^2\right)^2 + \Gamma_j^2 E^2} + i\frac{f_j E_{0_j}^2 \Gamma_j E}{\left(E_{0_j}^2 - E^2\right)^2 + \Gamma_j^2 E^2} \tag{2.10}$$

TH-2572_156121026

where f_j is the strength of the *j*th oscillators, E_{0_j} is the energy position of the *j*th oscillators, and Γ_j is the width of the *j*th oscillator. Thus, the total contribution from the Lorentz oscillator is determined by the sum over the *j* number of oscillators. The contribution of these two models, i.e., the Drude model and Lorentz oscillators, to the final model dielectric functions of the samples can be parameterized as: $\varepsilon_{DL} = \varepsilon_D + \varepsilon_L$. Moreover, the SE technique is quite sensitive to the surface features and interface properties of the sample. In this regard, generally, the surface roughness layer on top of the ITO thin film layer is modeled by Bruggeman effective medium approximation (BEMA) [148],

$$f_{ITO}\frac{\varepsilon_{ITO}-\varepsilon_{SR}}{\varepsilon_{ITO}+2\varepsilon_{SR}}+f_{void}\frac{\varepsilon_{void}-\varepsilon_{SR}}{\varepsilon_{void}+2\varepsilon_{SR}}=0 \quad (2.11)$$

where f_{ITO} and f_{void} are the volume fractions of the ITO layer and void, respectively. ε_{ITO} and ε_{void} is the dielectric constants of the ITO film and the void medium, respectively. For modeling surface roughness, it is considered that both the system has equal volume fractions, i.e., $f_{ITO} \equiv f_{void} \equiv 0.5$. However, BEMA is valid for spherical inclusion of the surface constituents and fails to describe surface constituents with different geometry. In such cases, ABEMA was introduced [151, 152]. Though ABEMA was developed originally for these ordered surface features, it is found very useful in describing the optical features of gratings with randomly rough edges [153]. The equation of ABEMA is given by,

$$f_{ITO}\frac{\varepsilon_{ITO}-\varepsilon_{SR}}{\varepsilon_{ITO}/\varepsilon_{SR}+L_i\left(\varepsilon_{ITO}-\varepsilon_{SR}\right)}+f_{void}\frac{\varepsilon_{void}-\varepsilon_{SR}}{\varepsilon_{void}/\varepsilon_{SR}+L_i\left(\varepsilon_{void}-\varepsilon_{SR}\right)}=0 \quad (2.12)$$

where L_i is the depolarization factor along the ith-axis. Equation (2.12) has to be solved for dielectric permittivity of the surface roughness layer ε_{SR}. Now, suppose the shape of the surface roughness constituents deviates from the spherical nature. In that case, the depolarization factor along the optical axis (along the *z*-direction) will be different from the perpendicular directions (*x*- and *y*-directions). For uniaxially anisotropic materials, the value of L_x and L_y can be easily calculated from L_z using the relation:

$$L_x = L_y = \frac{1-L_z}{2} \quad (2.13)$$

TH-2572_156121026

In SE analysis of the present work, the variable parameters used in the fitting algorithm are: ITO layer thickness, surface roughness (ABEMA) thickness f_{ITO}, depolarization coefficient along the z-direction L_z, Drude model parameters (E_P, E_Γ) and parameters for multiple Lorentz oscillators (f, E_0, Γ). ε_∞ was fixed at 0 for all the samples. Values of each of these parameters is given in the tabular form in the relevant chapters.

2.3 Measurement of ENZ plasmon resonance and LMR spectra via K-R geometry

The experimental measurement of the ENZ plasmon resonance signal was done in the same SE instrument by employing K–R geometry. A photograph of the SE instrument taken during the reflectivity spectra measurement using the K–R geometry-based setup is as shown in Figure 2-9. The schematic of the actual K-R geometry is also shown at the inset of the same figure. θ_i and θ_r are the incident and reflection angles inside the prism. These angles can be calculated easily from the incident angle (θ) outside the prism using the geometrical relation

$$\theta_i = \theta_r = 90 - \frac{\theta_P}{2} - \sin^{-1}\left(\frac{\sin\theta_{FA}}{n_P}\right) \tag{2.14}$$

where θ_P is the prism angle and for a right-angle prism, its value is 90°. n_P is the refractive index of the prism. θ_{FA} is the face angle and is given by,

$$\theta_{FA} = 90 - \frac{\theta_P}{2} - \theta \tag{2.15}$$

The dielectric constants of the film, surface roughness, and air layers are indicated clearly in the inset of Figure 2-9. The substrate holding a thin film layer having some surface roughness was index-matched to the right angle BK7 glass prism (Model: RT-107A; Make: *Prism India Pvt. Ltd.*; Dimensions: 22.9 × 22.9 × 20 mm) with index matching fluid (Model: *IML 150*; Make: *Norland*; refractive index, n: 1.52 @ 589 nm; viscosity: 100 cps). After each measurement, the prism was thoroughly cleaned using methanol reagent (HPLC Grade, purity: 99%,). The incident angle outside the prism of a purely TM-polarized light was varied from 50° to 70° in a step of 1°, and the reflected data were collected over the wavelength range of 900 – 1700 nm using the OMA NIR detector. The stage height was adjusted in such a way that

TH-2572_156121026

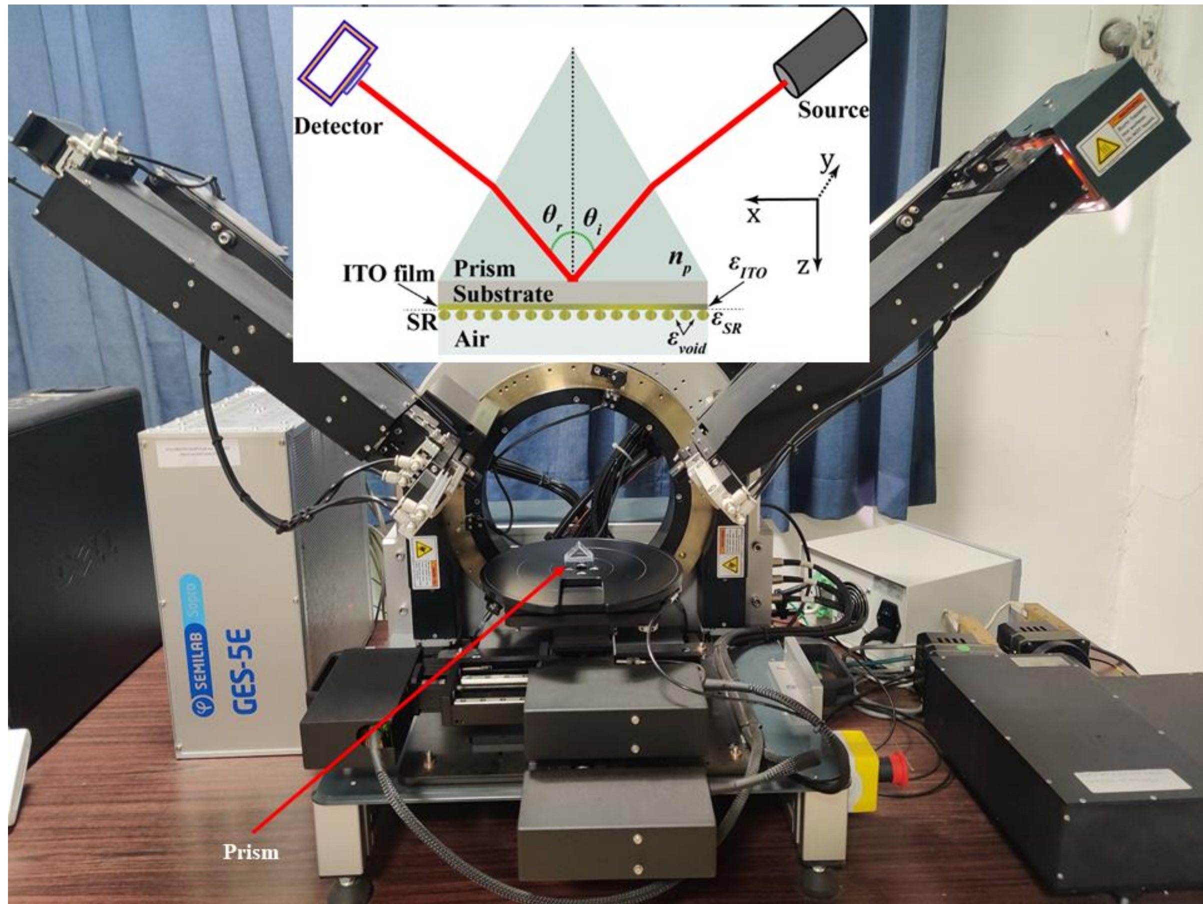

Figure 2-9. Photograph of the SE instrument during the measurement of reflectivity spectra at the incident angle 50°. Inset shows the schematic diagram of the K–R geometry-based setup used for the reflection measurement. A right-handed x–y–z coordinate system is displayed on the right-hand side to give an idea about the direction of propagation with respect to the sample geometry.

the intensity was maximized at the detector.

Furthermore, a similar kind of setup was used for LMR spectra measurement, with the only difference being the usage of grazing angles. Figure 2-10 shows the photograph of the SE instrument while taking the reflection measurement at the incident angle of 89.95°. A simple K-R configuration, where both incident and reflected light travels through the diagonal faces of the right-angle BK7 glass prism, as shown in the inset of Figure 2-10, was applied for this purpose. Note that the present setup is relatively more straightforward than that used in Ref. [44]. In their K-R configuration, the light beam was incident over the lateral faces of a customized all-side-polished prism. LMR reflection data for TE and TM polarizations over the

TH-2572_156121026

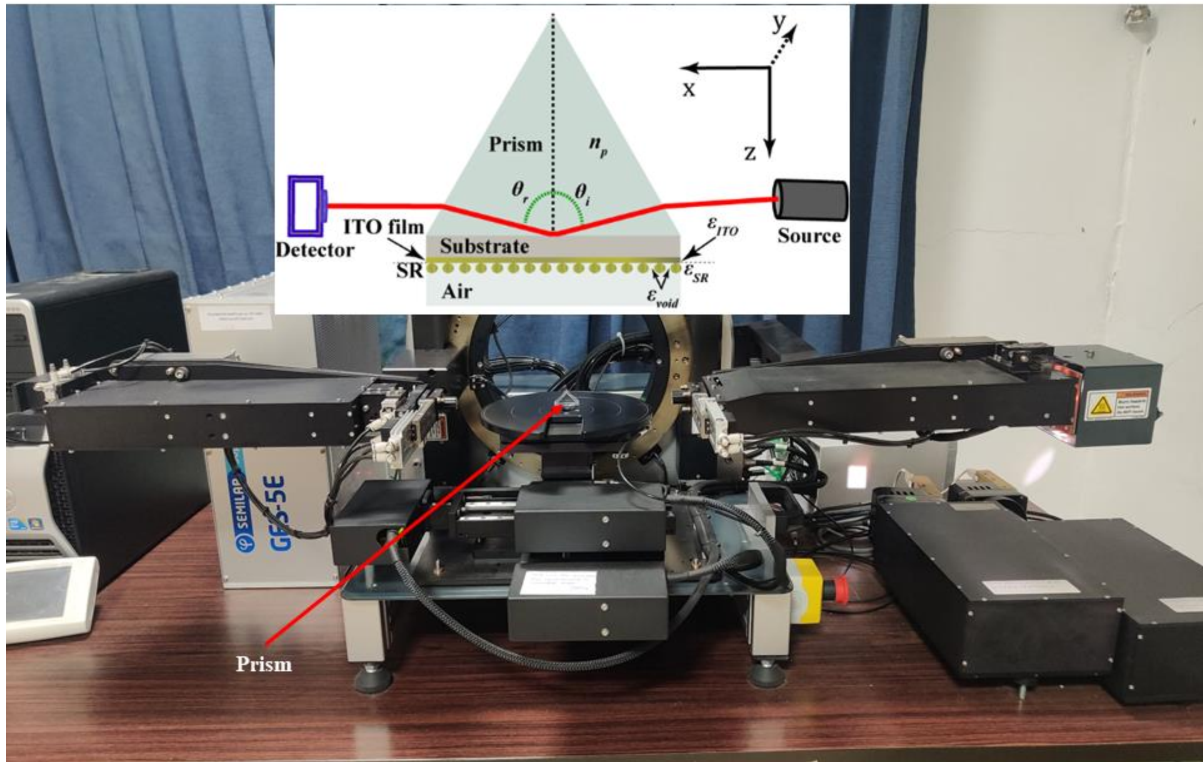

Figure 2-10. Photograph of the SE instrument during the measurement of reflectivity spectra at the incident angle 89.95°. Inset: Schematic of the K-R geometry employed for LMR measurement. A right-handed x-y-z coordinate system is placed at the right-hand side to describe the direction propagation with respect to the sample plane.

wavelength range of 400 – 900 nm was recorded using the CCD detector. However, both CCD and OMA NIR detectors were used simultaneously for RI sensing experiments to cover the maximum wavelength domain. For measuring the angular dispersion of the LMR spectra, the incidence angle was varied from 80° to 89.95° at a step of 1° (0.95° for the last step).

2.4 Description of the numerical approach

A transfer matrix method (TMM), which connects the field amplitudes of the first layer to the last layer in a multilayered system, is generally used to effectively simulate the reflection and transmission data from a multilayer film [154]. But this commonly used TMM framework is valid for the isotropic layer only. However, as discussed in Section 2.2, the surface roughness layer composed of particulates having a random size and shape behaves as an optically anisotropic layer. The dielectric constant of such an anisotropic material is a tensor quantity with diagonally non-vanishing components, ε_a^x, ε_a^y, and ε_a^z, respectively. The optical

TH-2572_156121026

response of such a layer differs significantly from that of the isotropic layer, such as the uniform film underneath the surface roughness. As for numerical integration of this optically anisotropic description in a multilayered structure, a 4 × 4 matrix formulation was introduced by Berreman [155]. However, this bulky 4 × 4 matrix can be reduced to a relatively simpler 2 × 2 matrix, and the coupling terms of the TM- and TE- polarized components can be ignored safely if we approximate the azimuth angle between the direction of the anisotropic inclusions and the incident beam to be zero [156]. Proceeding with this approximation, a commonly used multilayered TMM [154] is being modified to include optical anisotropy in the calculation. For TE-polarized light, the modified intermediate transfer matrix, which relates the field components of the consecutive layers of isotropic and anisotropic materials considering the wave-propagation along the *z*-direction, is given by,

$$M_i = \frac{1}{2}\begin{pmatrix} \left(1+\frac{k_z^{a,TE}}{k_z^i}\right)e^{-ik_z^i d_i} & \left(1-\frac{k_z^{a,TE}}{k_z^i}\right)e^{-ik_z^i d_i} \\ \left(1-\frac{k_z^{a,TE}}{k_z^i}\right)e^{+ik_z^i d_i} & \left(1+\frac{k_z^{a,TE}}{k_z^i}\right)e^{+ik_z^i d_i} \end{pmatrix} \tag{2.16}$$

For TM-polarized light, the same equation reads as,

$$M_i = \frac{1}{2}\begin{pmatrix} \left(1+\frac{\varepsilon_i k_z^{a,TM}}{\varepsilon_a^x k_z^i}\right)e^{-ik_z^i d_i} & \left(1-\frac{\varepsilon_i k_z^{a,TM}}{\varepsilon_a^x k_z^i}\right)e^{-ik_z^i d_i} \\ \left(1-\frac{\varepsilon_i k_z^{a,TM}}{\varepsilon_a^x k_z^i}\right)e^{+ik_z^i d_i} & \left(1+\frac{\varepsilon_i k_z^{a,TM}}{\varepsilon_a^x k_z^i}\right)e^{+ik_z^i d_i} \end{pmatrix} \tag{2.17}$$

where, d_i is the thickness of the concerned layer (film or surface roughness). Note that these equations are different from that described in Ref. [154], applicable for isotropic layers only. the wave-vectors for isotropic (k_z^i) and anisotropic ($k_z^{a,TE}$ and $k_z^{a,TM}$ for TE- and TM-polarizations, respectively) layers are given by [157],

$$\begin{aligned} k_z^i &= \sqrt{\varepsilon_i \omega^2 - k_x{}^2} \\ k_z^{a,TE} &= \sqrt{\varepsilon_a^y \omega^2 - k_x{}^2} \\ k_z^{a,TM} &= \sqrt{\varepsilon_a^x \omega^2 - k_x{}^2\, \varepsilon_a^x / \varepsilon_a^z} \end{aligned} \tag{2.18}$$

where, ε_i is the dielectric constant of the isotropic film layer. $\varepsilon_a^x, \varepsilon_a^y$ and ε_a^z is the dielectric constant of the surface roughness layer along *x*-, *y*- and *z*- directions, respectively.

TH-2572_156121026

$k_x = \left(\frac{2\pi}{\lambda}\right) n_p \sin\theta_i$ is the incident wave-vector with n_p and θ_i being the refractive index and angle this incident wave makes inside the prism. For an N-layer system with an interconnecting isotropic and anisotropic layer in the middle, the overall transfer matrix is given by [154],

$$M = \left(\prod_{i=1}^{N} M_i\right) = \begin{pmatrix} M_{11} & M_{12} \\ M_{21} & M_{22} \end{pmatrix} \tag{2.19}$$

Now, using these matrix elements, reflection coefficient and thereby, the total reflection can be calculated via the relation [154]:

$$\begin{aligned} r_{TE/TM} &= \frac{M_{21}}{M_{11}} \\ R_{TE/TM} &= \left| r_{TE/TM} \right|^2 \end{aligned} \tag{2.20}$$

This modified TMM algorithm was implemented in MATLAB (version: *2018b*; License No.- 40783582) code by employing the 5-layer system, as shown in the insets of the Figure 2-9 and Figure 2-10. The first two layers, i.e., prism and substrate, are approximated to be one single layer of semi-infinitesimal thickness extended in the negative *z*-direction. This combined layer is modeled using *nk*-file of BK-7 glass from the *nk*-file library of SEA software (*SEA v1.0.4*). Drude-Lorentz (DL) model is applied to reconstruct the dispersion behavior of the PLD-ITO thin film layer. Partial dielectric constants of the surface roughness layer on top of the film are retrieved by solving the Eqn. (2.12), and the same values were used for modeling the layer. The air layer was also taken as a semi-infinite layer and its dielectric constant was taken as unity. Parameters of the DL model and ABEMA assisted surface roughness layer corresponding to each PLD-ITO thin film will be further discussed separately in the subsequent chapters.

2.5 Conclusion

In the present chapter thin film deposition procedure employed for the deposition of ITO thin films studied in the current thesis work is discussed. This chapter also elaborates on different techniques that are being used for the characterization of PLD-ITO thin films. Experimental setups employed for the measurement of ENZ plasmon resonance and LMR spectra are presented in detail. Finally, the modified TMM method utilized for the numerical simulation of the experimentally measured reflection spectra is described.

TH-2572_156121026

TH-2572_156121026

Chapter 3

Ambient Condition Dependent ENZ Plasmon Resonance Properties of PLD ITO Thin Films

PLD can be used to tune the inherent properties of the deposited film by carefully controlling the deposition parameters such as substrate temperature, gas pressure, usage of a variety of gases, target-to-substrate distance, and so on. Amongst these deposition parameters, the background gases serve various important purposes in the PLD chamber environment. To begin with, it contributes to the slowing down of plasma plumes through collisions during the time of flight. In the presence of gaseous environment, the plasma plumes gets slowed down because of the collisions and thereby, can lead to film surface with relatively fewer defects [158]. Thus, it eliminates one of the primary difficulties in thin films deposition via PLD, as discussed in Chapter 1. Additionally, depending upon the atomic mass of the background gases, particulates of different sizes and shapes can be generated [130]. Most importantly, in the case of TCOs, the introduction of gas proves to be the best way to control these oxygen vacancies. These oxygen vacancies, capable of donating free electrons [88], play a crucial role in determining the ENZ wavelength, which varies linearly with the carrier concentration of the film [69]. Wide tuning of this ENZ wavelength over a broad wavelength region greatly enhances the applicability of the thin film based ENZ research. So far, mainly, oxygen partial pressure has been utilized in the literature to achieve tuning of the ENZ wavelength for PLD-ITO films [136-138]. This is because of the fact that the number of oxygen vacancies in ITO thin films can be controlled directly with the oxygen partial pressure. Other PLD parameters such as substrate temperature, target-to-substrate distance, laser fluence, etc., do not offer such kind of flexibility. However, the use of other gases than oxygen could prove to be an alternative way to control the oxygen vacancies in the ITO thin films. However, relatively few reports are available in the literature about the optical, structural, and electrical properties of the ITO thin films deposited under gases like N_2, He, Ar, Xe, etc. [132, 133, 158-161]. Interestingly, these

TH-2572_156121026

reports suggest that deposition under such background gases leads to lower resistivity values at the expense of optical transparency of PLD-ITO thin films. The improvement in electrical properties was linked to the increase in oxygen vacancies in such an oxygen-less gaseous environment. Thus, a detailed study of the effect of background gases on the ENZ wavelength of ITO thin films could be very interesting.

Furthermore, most of the studies in the literature are mainly concerned with the tuning aspect of the ENZ wavelengths. In comparison, the linkage of ENZ wavelengths with the ENZ plasmon resonance has rarely been studied. Chen *et al.* explored, both experimentally and numerically, the effect of Ag inclusion percentages on the ENZ wavelength as well as ENZ plasmon resonance properties of Ag-ITO co-sputtered composite films [97]. In another interesting study, Johns *et al.* reported octave span, controllable tuning of ENZ wavelength of commercial ITO thin films over broad-spectrum by employing a low temperature annealing scheme [162]. They also demonstrated experimentally as well as numerically the excitation of SPPs and ENZ modes separately in ITO thin films of different thicknesses. Though both these reports deal with the connection between ENZ wavelengths and ENZ plasmon resonance, their numerical analysis is devoided of any kind of description about the effect of surface roughness, which is paramount in the case of PLD-ITO thin films, especially under inert gases [159]. In addition to this, electric field enhancement, which is a necessary condition for plasmon resonance ENZ thin films, was not discussed in any of these reports.

In this chapter, tuning of ENZ wavelength is studied systematically in the context of ITO thin films deposited under various PLD background gases such as O_2, N_2, Ar, and He. ENZ plasmon resonance in connection to the ENZ wavelengths is explored experimentally via a simple K-R geometry. A commonly used TMM algorithm is modified to account for the surface roughness effect of the ITO thin films through the application of ABEMA. Local field intensity enhancement factor (LFIEF) is calculated for these PLD-ITO thin films to understand the angular dispersion behavior of the ENZ plasmon resonance.

3.1 Experimental Details and Characterization Techniques

ITO thin films were deposited in a PLD chamber by focusing a *Q*-switch Nd:YAG laser onto the 10 wt% SnO_2 doped ITO pellet. The working pressure in the chamber was maintained at 0.05 mbar during the deposition for all the ambient gases, i.e., O_2, N_2, Ar, and He. Target-

TH-2572_156121026

to-substrate distance and substrate temperature were fixed at 3.5 cm and 400°C, respectively. The deposition time was varied in such a way that the overall thickness remains constant at 70 nm. The detailed procedure of pellet preparation, substrate cleaning, and PLD is given in Chapter 2. Variation of the dielectric constant (both real and imaginary) of PLD-ITO thin films over the wavelength range 220 – 1700 nm was acquired by fitting the SE spectra with the help of an optical model. This model employs a combination of Drude and multiple Lorentzian oscillators to fit the pristine film layer, while the surface roughness layer on top was taken care of by ABEMA. More details about the SE fitting procedure can be found in Chapter 2. Transmission data of the PLD-ITO thin films, which gives an account of the near-infrared absorption, were collected over the wavelength 250 – 2500 nm by a Uv-Vis-NIR spectrometer. Topological characterization, as well as the RMS roughness determination of the samples, were carried out using AFM. FESEM images were used to characterize the ITO thin films morphologically. Crystallographic phase analysis of the ITO thin films deposited under various background gases was achieved by XRD data analysis.

Angular dispersion behavior of ENZ plasmon resonance of PLD-ITO thin films was analyzed by employing a simple K-R geometry in the SE instrument. The incident TM polarized light angle was varied from 50° to 70° at step of 1° and reflection spectra were collected over the wavelength range of 900 – 1700 nm. K-R geometry and the reflection measurement procedure via SE are described in more detail in Chapter 2.

3.2 Results and Discussions

3.2.1 Structural, morphological, optical, and electric properties of PLD-ITO thin films under various ambient conditions

XRD data collected over the 2θ values of 10° to 70° for ITO thin films deposited under different background gases is shown in Figure 3-1. All the crystallographic peaks can be correlated to the cubic bixbyite nature of In_2O_3 crystal (PDF Card No.: 01-089-4598). No extra peaks related to any of the sub-phases of ITO thin films were detected. This indicates that all the PLD-ITO thin films are of pure ITO phase. For the films deposited under O_2 and N_2 gas, a strong preferred orientation along the (222) plane is observed with no signature of the (400) plane. In contrast, films deposited under Ar and He exhibit a clear signature of (400) plane,

TH-2572_156121026

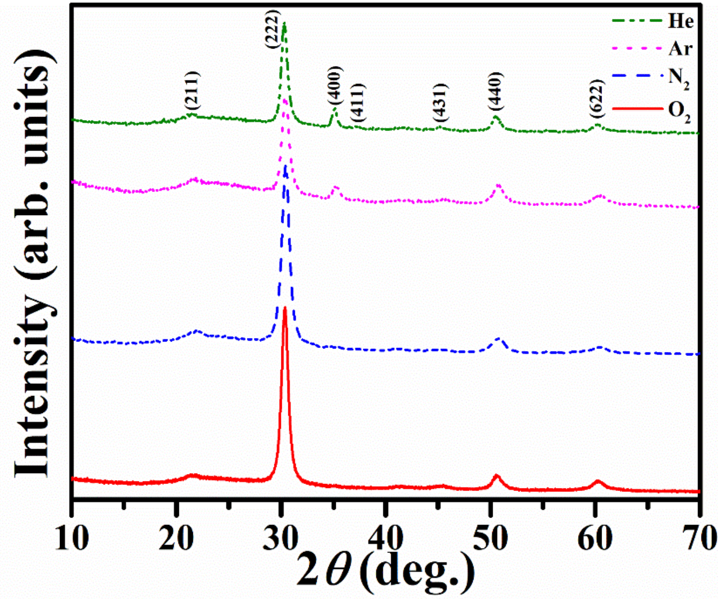

Figure 3-1. XRD pattern of ITO thin films deposited under various ambient conditions: O_2 (solid red line); N_2 (dashed blue line); Ar (dotted magenta line); He (dash-dot olive line).

though the preferred orientation remains along (222) direction. The (400) plane occurrence among the ITO films deposited in inert gases can be corroborated by the increased oxygen deficiency in such films [163]. In the inert gas environment, the presence of gas mainly influences the scattering of the ablated species, while the oxidation state of the plume gets affected negligibly [164]. Thus, the already oxygen-deficient plasma generated from the ITO target maintains its oxidation state which leads to oxygen deficient films.

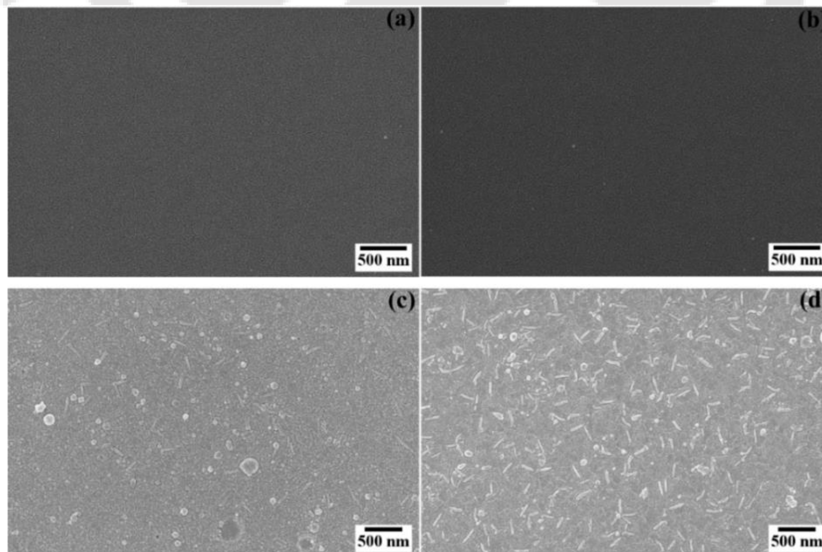

Figure 3-2. FESEM images of ITO thin films under different background gases: (a) O_2; (b) N_2; (c) Ar; (d) He.

TH-2572_156121026

FESEM images of PLD-ITO thin films under various ambient gases are shown Figure 3-2. It is evident that the films deposited under O_2 and N_2 gases are completely smooth without the presence of any particulates on the surface. In a stark contrast, ITO films deposited under inert gases are highly nanostructured in nature. This observation is similar to the previous reports on ITO thin films deposited under an inert gas environment in the PLD system [132, 133, 159].

Figure 3-3 displays the AFM images of the PLD-ITO thin films at different ambient conditions. As shown in these images, the surface topology of the samples is exactly similar to that of FESEM images. RMS surface roughness observed from the AFM analysis found to be to be 1 ± 0.4 nm, 0.9 ± 0.1 nm, 4.8 ± 0.9 nm, and 5.7 ± 0.8 nm for ITO thin films deposited under O_2, N_2, Ar, and He background gases, respectively. Nanostructured film surface in an inert gas environment is responsible for the increase in surface roughness in such films.

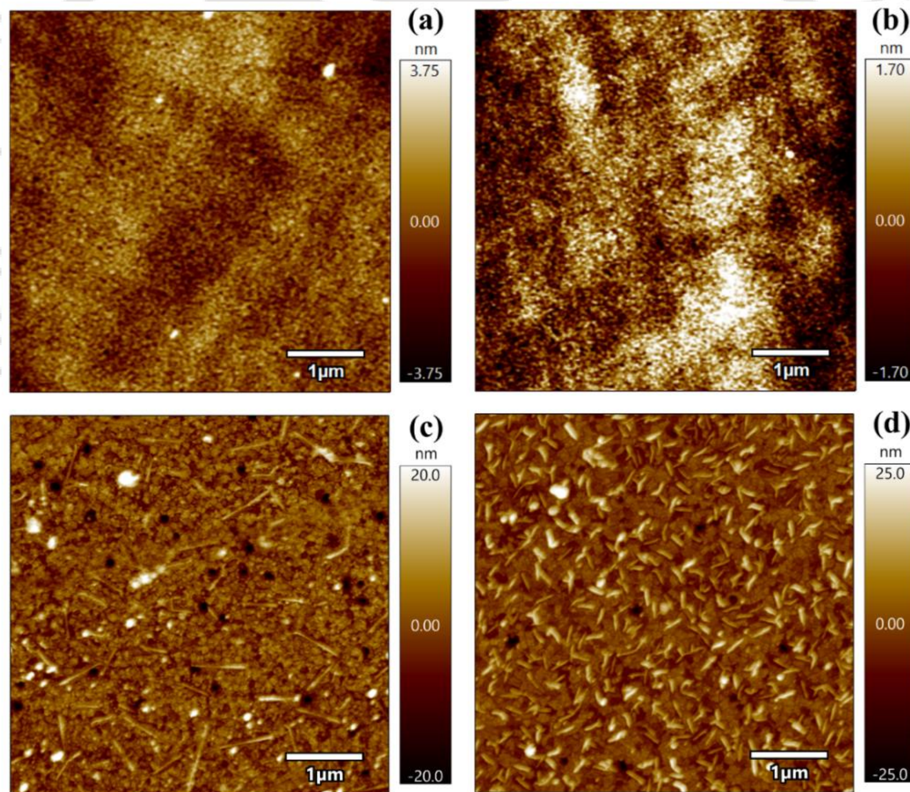

Figure 3-3. 5×5 μm 2D AFM micrograph of PLD-ITO thin films under various ambient conditions: (a) O_2; (b) N_2; (c) Ar; (d) He.

TH-2572_156121026

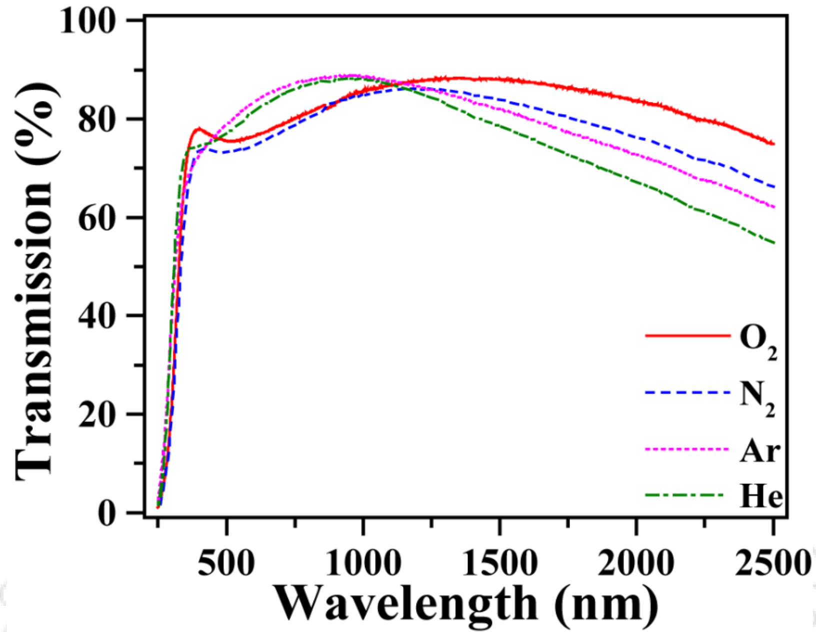

Figure 3-4. Transmission spectra of ITO thin films deposited under various deposition environments: O_2 (solid red line); N_2 (dashed blue line); Ar (dotted magenta line); He (dash-dot olive line).

Transmission spectra of PLD-ITO thin films for different background gases over the wavelength range of 250 – 2500 are as shown in Figure 3-4. All ITO thin films show a visible range transparency value of around 80%. A similar type of transparency value was observed in an earlier report on PLD-ITO thin films deposited under O_2 and inert gases [158]. Interestingly, there is a systematic decrease of NIR range transmission from films deposited under O_2 gas to film deposited under He gas. This behavior can be explained on the basis of free carrier absorption, which dictates the NIR region transparency in TCO thin films [165, 166]. Absorption coefficient (α_{NIR}) in the NIR range is related to the carrier concentration (n_e) and mobility (μ_H) via the following relation [165],

$$\alpha_{NIR} = \frac{C\lambda^2 n_e}{\mu_H} \tag{3.1}$$

where C is a proportionality constant and λ is the wavelength of the incident radiation. Thus, ITO thin films with high carrier concentration and low mobility will show the highest free carrier absorption values in the NIR range. Based on the NIR transmission values, the order of free carrier concertation of the ITO thin films under different background gas appears to be

TH-2572_156121026

$(n_e)_{\mathrm{He}} > (n_e)_{\mathrm{Ar}} > (n_e)_{N_2} > (n_e)_{O_2}$. This observation will be further consolidated in the subsequent sections.

The optical properties of PLD-ITO thin films were mainly explored by SE. An optical model relying on the correct representation of the overall film layer (film + surface roughness) was developed to analyze experimentally obtained SE data. ITO film layer deposited over the substrate was modeled using the Drude model and two Lorentz oscillators. BEMA has been used so far in the literature to model the surface roughness layer on the top of this film layer. But as it is evident from FESEM and AFM images, ITO thin films deposited under different ambient conditions, especially those deposited under inert gases, do not follow a spherical description of commonly used BEMA [148]. Thus, ABEMA, which takes the deviation of spherical surface morphologies into account, is used in such cases. At the same time, normal BEMA was applied to obtain surface roughness for thin films deposited under O_2 and N_2 gases. Figure 3-5 shows the measured and fitted pseudo-dielectric function, both real ($\langle \varepsilon_1 \rangle$) and ima-

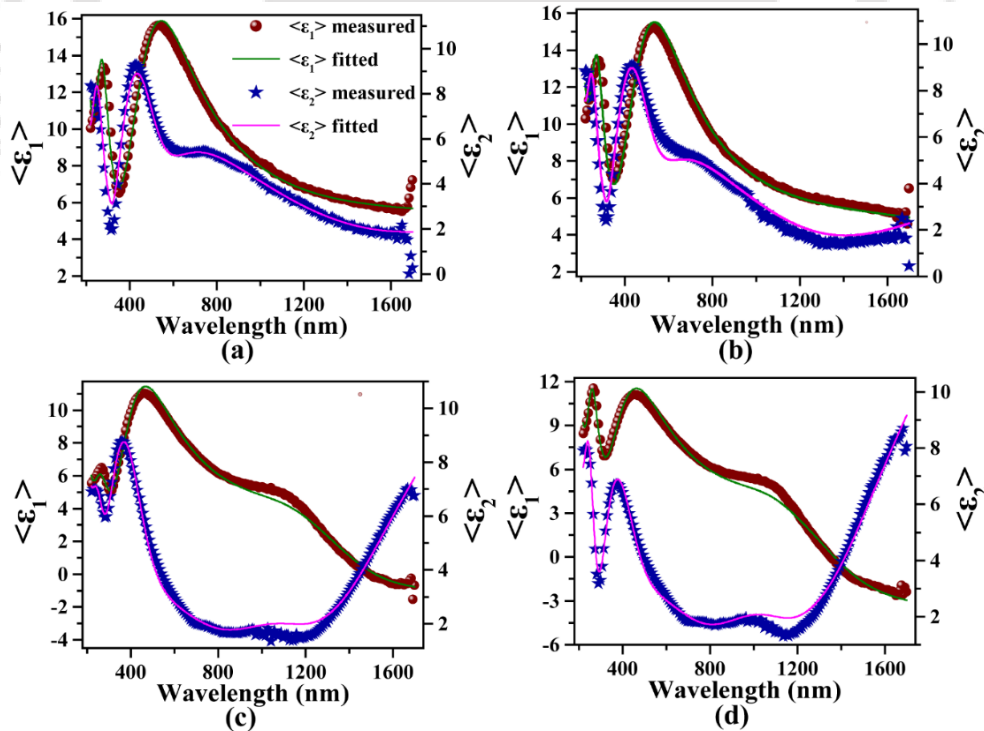

Figure 3-5. Variation of real ($\langle \varepsilon_1 \rangle$) and imaginary ($\langle \varepsilon_2 \rangle$) part of pseudo-dielectric permittivity (geometric dots represent measured data, and solid lines represents fitted) of ITO thin films deposited at different ambient conditions: (a) O_2; (b) N_2; (c) Ar; (d) He.

TH-2572_156121026

ginary part ($\langle \varepsilon_1 \rangle$) for ITO thin films deposited under different PLD chamber ambient over the wavelength range of 220 -1700 nm. It is quite clear that the prescribed optical model can fit the experimentally observed data quite well in all the ITO thin films.

All critical parameters obtained from SE data fitting are listed in Table 3-1. It is to be noted that the overall film thickness remains constant at 70 nm for all the ITO films deposited under various background gases. ITO thin films deposited under O_2 and N_2 background gases follow the standard BEMA description. BEMA includes two major conditions: (i) the volume percentages of void and material is 50% each; (ii) depolarization coefficient (L_z) is equal to 0.333, signifying the spherical nature of the surface constituents [148]. However, in the case of ITO thin films deposited under Ar and He gases, though the 50 - 50 description of BEMA is retained, the value L_z is changed from 0.333 to a higher value. Change in depolarization coefficient from the value 0.333 represents the nanostructured surface of these films, as observed in FESEM and AFM images. Additionally, the surface roughness predicted by these approximations, i.e., BEMA for O_2 and N_2 gases and ABEMA for inert gases, matches quite well with the RMS surface roughness determined by AFM. This close matching of surface roughness values gives a concrete experimental validation to the optical model used in SE analysis.

Now, coming to this DL model parameters, it is observed that the carrier concentration determined by the Drude model increases monotonically from the ITO thin film deposited under O_2 gas to that deposited in He gas. This trend is exactly similar to that predicted in NIR absorption analysis and can be corroborated by the increase of oxygen vacancies in ITO films under inert gas compared to those deposited under O_2 and N_2 gases. The sheet resistance follows a completely opposite trend to that of carrier concentration and decreases gradually from O_2 to He gas. Two Lorentz oscillators at higher photon energy values for all the PLD-ITO thin films signify the band gap absorption occurring in these films. Lastly, low RMSE values are the signature of the good quality fitting of the SE data for all the ITO deposited under various ambient conditions.

TH-2572_156121026

Table 3-1. The list of parameters obtained from SE fitting of ITO thin films deposited under different background gases. Along with the plasma energy (E_P) and broadening (E_Γ), carrier concentration and sheet resistance extracted from the Drude model is also given. In the table, two Lorentz oscillators are designated by 1st and 2nd. Oscillator strength (f), central position (E_0), and width (Γ) is given for each oscillators. Uncertainties associated with different parameters are also reported. Note that, SR stands for surface roughness.

Ambient cond.	Film thick. (nm)	SR (nm)	ABEMA parameters		Drude model				Lorentz oscillators						RMSE
									1st			2nd			
			Depol. coefficient (L_z)	Void %	E_p (eV)	E_Γ (eV)	Carrier conc. × 10^{20} (cm^{-3})	Sheet resistance (Ω/ sq.)	f	E_0 (eV)	Γ (eV)	f	E_0 (eV)	Γ (eV)	
O_2	67	0.8	0.333	50	1.13 ± 0.02	0.37 ± 0.02	2.31 ± 0.09	321.3 ± 31.4	3.46 ± 0.13	8.09 ± 0.13	0.07 ± 0.28	1.15 ± 0.09	5.06 ± 0.03	1.83 ± 0.09	0.325
N_2	64	0.7	0.333	50	1.39 ± 0.01	0.37 ± 0.01	3.52 ± 0.07	220 ± 12.7	3.48 ± 0.13	7.63 ± 0.11	0.10 ± 0.21	1.39 ± 0.12	5.09 ± 0.04	1.94 ± 0.09	0.350
Ar	68.1	3.9	0.406 ± 0.090	50	1.81 ± 0.01	0.23	5.91 ± 0.05	94.6 ± 1.9	3.09 ± 0.06	8.44 ± 0.08	0.89 ± 0.17	0.66 ± 0.06	5.19 ± 0.03	1.54 ± 0.08	0.254
He	56.6	10.3	0.477 ± 0.114	50	1.85 ± 0.01	0.22	6.24 ± 0.05	71.2 ± 1.2	2.84 ± 0.06	7.85 ± 0.08	0.55 ± 0.14	1.00 ± 0.04	5.22 ± 0.04	2.22 ± 0.06	0.226

TH-2572_156121026

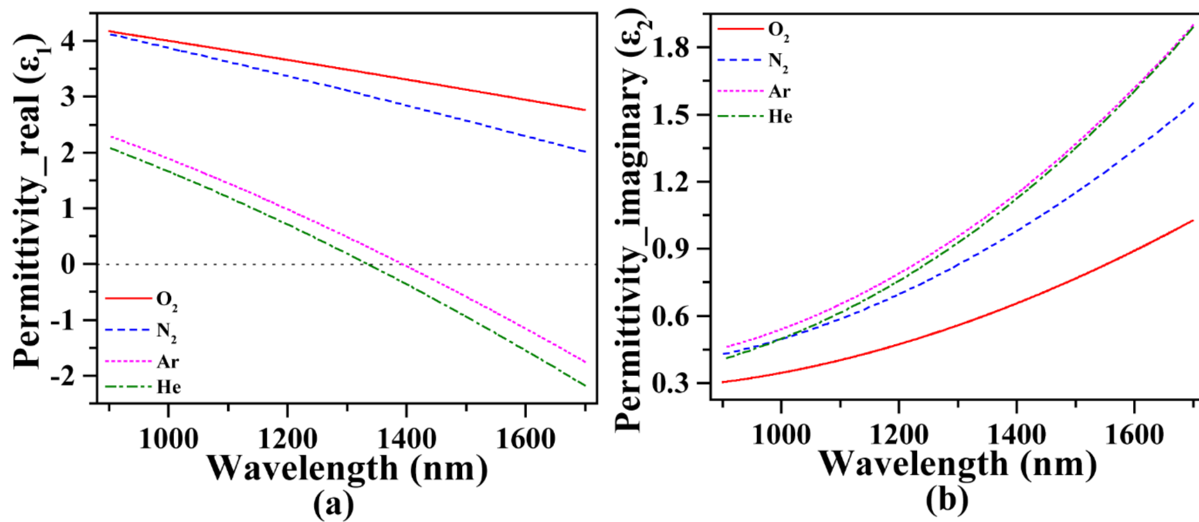

Figure 3-6. Variation of (a) real (ε_1) and (b)imaginary (ε_2) part of permittivity of the PLD-ITO thin film under different background gases: O_2 (solid red line); N_2 (dashed blue line); Ar (dotted magenta line); He (dash-dot olive line).

Figure 3-6 demonstrates the variation of the real and imaginary part of permittivity, as determined by the SE analysis, of all the PLD-ITO thin films over the 900 – 1700 nm wavelength range. Note that this wavelength range is selected since our ENZ plasmon resonance analysis focuses on this wavelength widow only. From the variation of the real part of permittivity, it is observed that ITO thin films deposited under O_2 and N_2 gases do not show any cutoff and remain positive throughout the entire spectrum. In contrast, ITO thin films deposited under both Ar and He environment show clear cutoffs at the wavelength of 1393 nm and 1335 nm, respectively. This observation can be directly correlated to the variation of carrier concentration, as given in Table 3-1. The ITO thin films with higher carrier concentration, i.e., films deposited under Ar and He, demonstrate a distinct cutoff or ENZ wavelength, while the carrier concentration in O_2 and N_2 gases is not high enough to produce a cutoff in the experimentally viable wavelength range. As shown in Figure 3-6 (b), the imaginary part of permittivity of all the PLD-ITO thin films exhibits an upward trend with increasing wavelength. This is typical behavior of Drude-type free carrier absorption [69, 137]. The imaginary part of permittivity signifies the losses in an optical device [69]; the lower the imaginary part in and around the ENZ wavelengths, the better the efficiency of the device. Here, the value of the imaginary part of permittivity at the ENZ wavelength comes out to be 1.13 and 0.99 for ITO thin films deposited at Ar and He gas, respectively. Thus, the ITO film

TH-2572_156121026

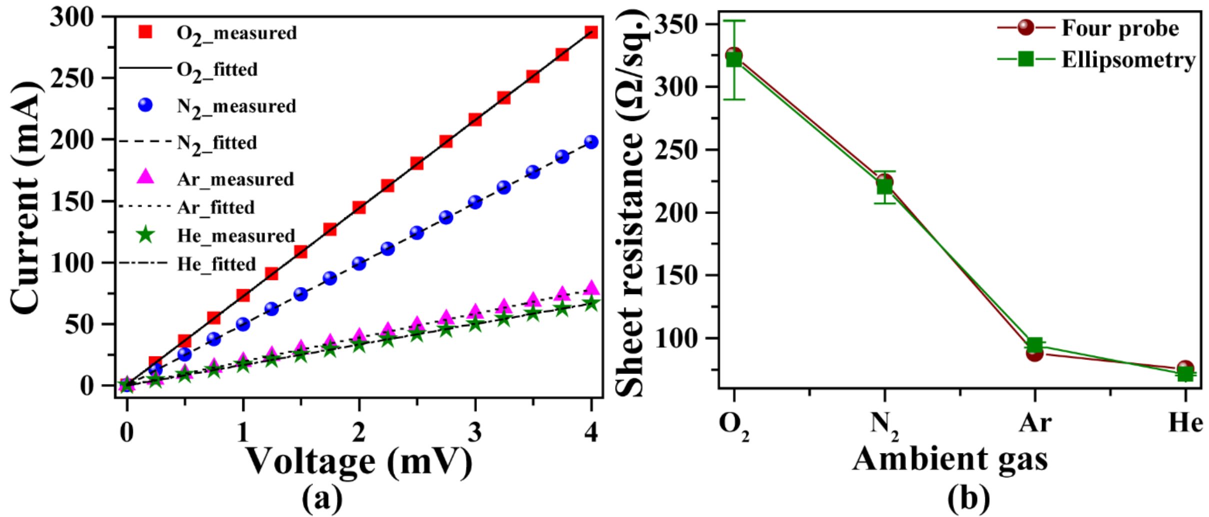

Figure 3-7. (a) Voltage vs. current graph obtained using four probe method; (b) comparison of sheet resistance determined by four probe and ellipsometry method.

deposited at He gas is a certainly a better plasmonic material in terms of loss than the one under Ar gas.

The electrical properties of the samples were analyzed mainly by observing the four probe current vs. voltage graph as shown in Figure 3-7 (a). All the PLD-ITO thin films show the typical ohmic behavior and the observed voltage data at different currents can be fitted perfectly with a linear fit. The sheet resistance obtained from these linear fits is plotted in Figure 3-7 (b). The measured sheet resistance is valued at 324.7 ± 0.43 Ω/sq. for ITO film deposited under O_2 gas. But, in the case of He gas, it decreased rapidly to 75.5 ± 0.07 Ω/sq., though the value is still slightly higher than the commercial ITO coated glass of similar film thickness [167]. The main reason behind the increase in sheet resistance is the existence of nanostructures over the surface in such films, which hinders the electron conduction through scattering [168]. Importantly, the sheet resistance determined by the SE for ITO thin films deposited under different background gases matches reasonably well with that obtained from the four probe analyses. This further validates the optical model used in SE data analysis.

3.2.2 Experimental reflection spectra

Experimentally measured reflection spectra of PLD-ITO thin films over the 900 – 1700 nm wavelength range are displayed in Figure 3-8. The angular dispersion of resonance spectra is analyzed by recording the reflection spectra at various incident angles (outside the prism)

TH-2572_156121026

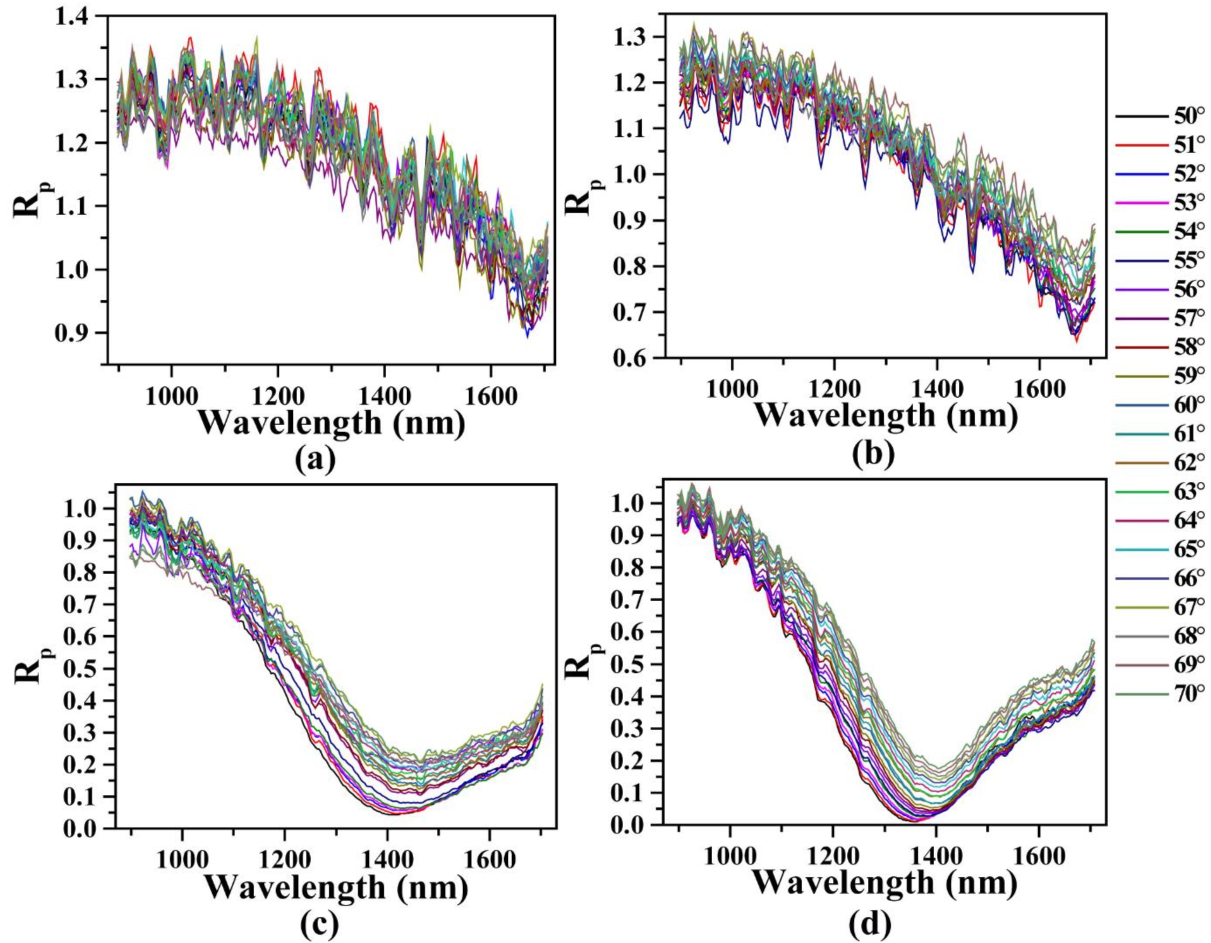

Figure 3-8. Experimentally measured reflection spectra over the wavelength range of 900 – 1700 nm for ITO thin films deposited at different ambient conditions: (a) O_2; (b) N_2; (c) Ar; (d) He. Color codes of various incidence angles (from 50° to 70°) are given over the right-hand side of the figure.

ranging from 50° to 70°. Now, internal angles inside the prism are greater than the total internal reflection (TIR) angle of the glass-air interface, i.e., ~ 42°. Thus, transmission can be neglected while calculating the absorption from the reflection spectra. As expected, ITO films deposited under O_2 and N_2 gases do not show any resonance absorption in the measured wavelength range. However, maximum absorption for each angle, occurring at the highest possible wavelength, i.e., 1700 nm, in the case of ITO film deposited under N_2 gas is much more than the film deposited under O_2 ambient. The observed difference in absorption in such a non-resonant condition can be correlated to the stark difference in the imaginary part of permittivity between these two films, as shown in Figure 3-6 (b). Now, both the ITO thin films deposited under inert gases show a very prominent dip in the reflection spectra, which indicates the existence of very strong resonant absorption. Interestingly, the resonance wavelength position

TH-2572_156121026

is relatively invariant of the incident angles for both the ITO films. This angular invariancy feature is certainly due to the CPs [110, 111], and not due to the SPs. Thereby, such resonance absorption is termed CPR or ENZ plasmon resonance. The highest absorption values observed in the case of PLD-ITO thin film under Ar gas is 95.68% at the wavelength of 1415 nm, and under He gas it is 98.98% at the wavelength of 1359 nm. Both these values occurred at the incident angle of 50°. The absorption in a resonance condition can be understood on the basis of two fundamental damping mechanisms: radiation damping and internal damping [19]. Among these two dampings, the first one, i.e., radiation damping, mainly depends upon the film thickness and thus, remains unaltered for both the ITO thin films having the same film thickness. However, the internal damping can be quantified as the imaginary part of the characteristic wave-vector β of SPs (CPs in this case), as given in eqn. (1.1). The value of imaginary part of β for films deposited under Ar and He gas is found out to be 1.44×10^{-3} nm^{-1} and 1.63×10^{-3} nm^{-1}, respectively. Thus, higher absorption value in ITO film deposited under He gas as compared to that in Ar gas can be explained on the basis of higher internal damping in the former.

3.2.3 Description and Results of Numerical Analysis

For a concrete numerical validation of the experimentally measured ENZ plasmon resonance spectra, a modified TMM method was developed in terms of a MATLAB script. The surface roughness description of the PLD-ITO thin films was incorporated in this modified TMM algorithm with the application of ABEMA. For a prism-film-surface roughness-air medium, substrate and prism are approximated to be one single layer for simplification purpose. The intermediate film layer was modeled using DL parameters given in Table 3-1, while the partial dielectric constants of the anisotropic surface roughness were included by solving the quadratic-natured equation of ABEMA. The modified TMM algorithm and detailed parametrization procedure are meticulously described in Chapter 2.

Numerically simulated ENZ plasmon resonance spectra of PLD-ITO thin films over the wavelength range of 900 -1700 nm is shown in Figure 3-9. It is quite clear that the proposed numerical simulation algorithm successfully recreates the overall features of the experimentally measured reflection spectra of all the ITO thin films deposited under various ambient gases. This agreement with experimental data is significantly better than the previous

TH-2572_156121026

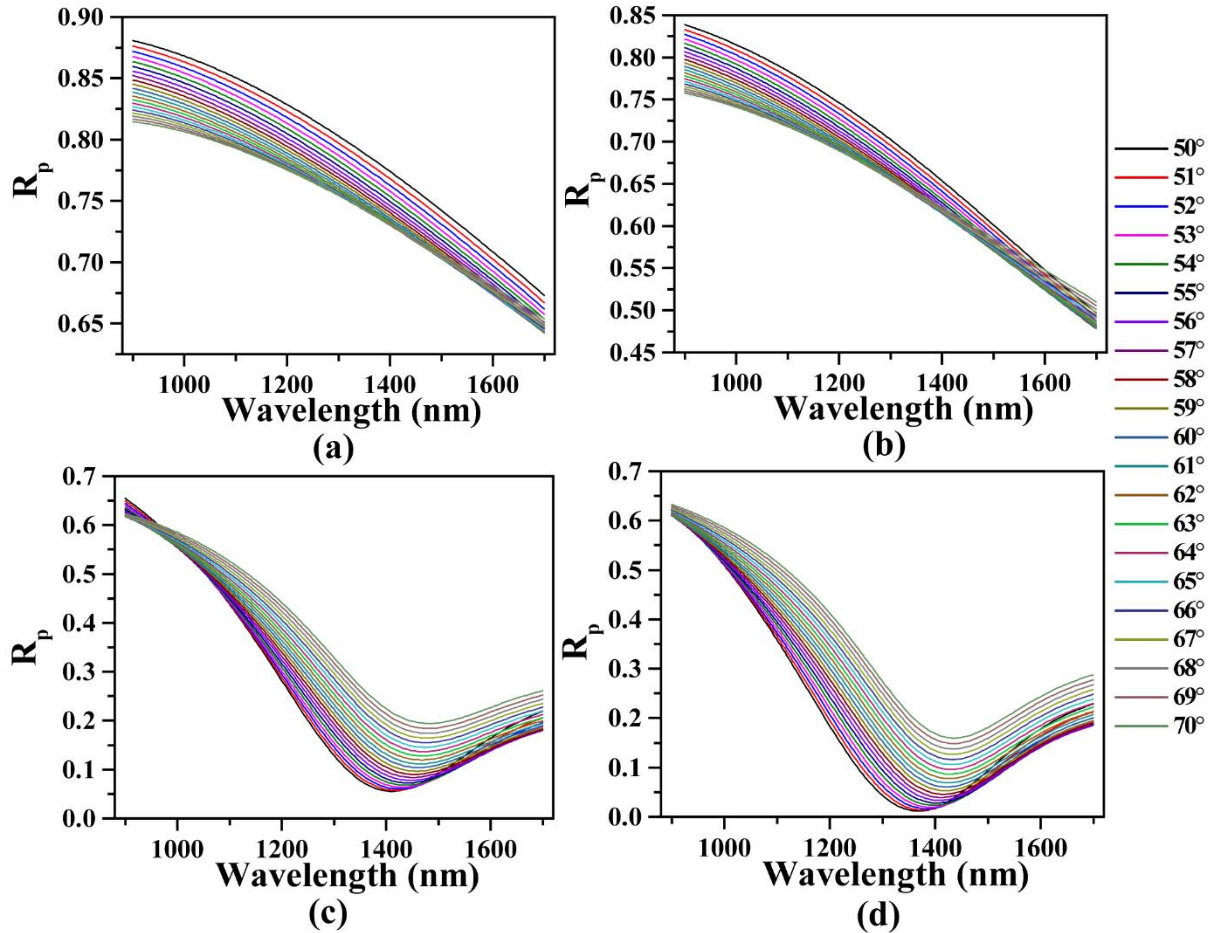

Figure 3-9. Numerically simulated reflection spectra of ITO thin films deposited under different ambient gases: (a) O_2; (b) N_2; (c) Ar; (c) He. The color code for incident angles in the range of 50° to 70° is shown at the right-hand side of the figure.

reports where the surface roughness effect is included in the numerical simulation algorithm [143, 169]. However, numerically determined absorption values are slightly less than the experimental ones, especially for the films deposited under inert gases. Local enhancement of electric field around the nanostructures lying on the surface of such films could be the reason for this slight disagreement in intensity. ABEMA, being an approximation method based on the averaged electric field of the surface constituents, could not take this local enhancement into account.

3.2.4 Results of Electric Field Enhancement Analysis

The local LFIEF was calculated for the ITO thin films deposited under various ambient conditions to understand the physical origin of the observed angular dispersion and absorption

TH-2572_156121026

values from ENZ plasmon resonance. LFIEF is defined as the square of the ratio of the local electric field at the film surface to the incident electric field [154]. The same MATLAB script that was used in the numerical simulation algorithm is applied in the LFIEF calculation. Figure 3-10 depicts the color map of the LFIEF over the 900 – 1700 nm wavelength at different incident angles for PLD-ITO thin films under various ambient conditions. It is observed that for both the ITO films deposited under O_2 and N_2 gas ambient, the LFIEF value is highest at the wavelength of 1700 nm and at the incident angle of 50°. It means that the highest field enhancement occurs beyond the experimentally achievable wavelength or incident angle values. Thus, there is no visible resonance in such films. Now, the highest local field intensity

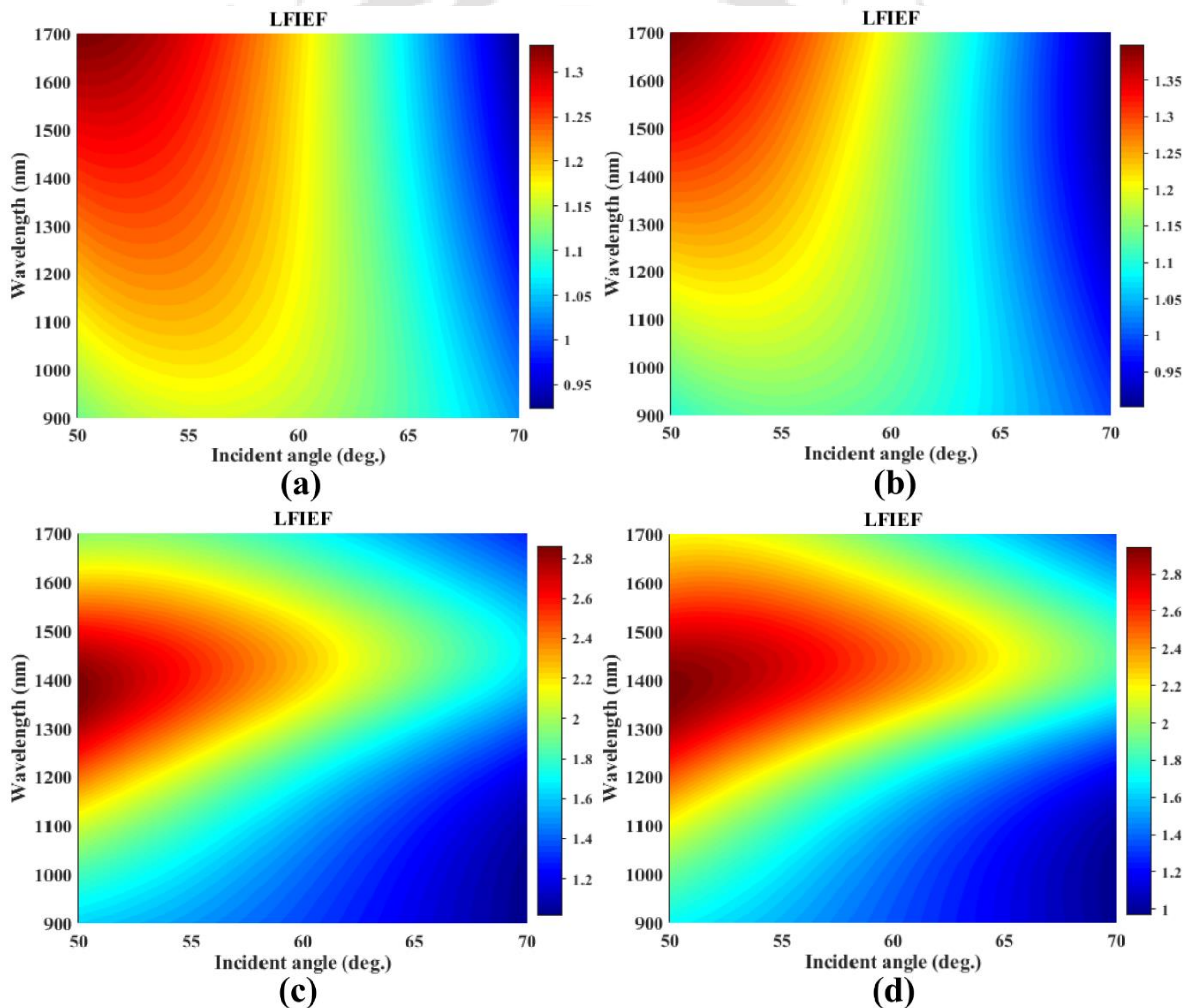

Figure 3-10. Color map of the angular dispersion of LEIEF over the wavelength range of 900 – 1700 nm for PLD-ITO thin under background gases: (a) O_2; (b) N_2; (c) Ar; (c) He. The color bar positioned at the right-hand side of each sub-figures indicates the amplitude of LEIEF.

TH-2572_156121026

is relatively localized in the wavelength domain for films deposited under Ar and He gases. This statement refers to the fact that the highest value of LFIEF for the incidence angle range of 50° - 70° occurs at relatively narrow wavelength domains of 1379 – 1459 nm and 1379 – 1450 nm for the Ar and He ambient, respectively. The angular invariance of the observed experimental ENZ plasmon resonance data for both films can be corroborated to this electric field localization over the resonance wavelengths. LFIEF value for the incident angle 50° at the resonance wavelengths of PLD-ITO thin films under Ar and He gas comes out to be 2.84 and 2.94, respectively. Such an electric field enhancement is responsible for the high degree of resonance absorption in these films. The occurrence of a very high electric field just above the ENZ wavelength is fairly common in ENZ-ITO thin films [105, 106]. The higher value of field enhancement in the ITO thin films deposited under He compared to the one deposited under Ar gas explains the observed absorption intensity difference in these two films.

3.3 Conclusion

In this chapter, tuning of the ENZ wavelength of ITO thin films over a broad wavelength region is achieved experimentally by changing the gas ambient of the PLD chamber. ITO thin films deposited under Ar and He gases exhibited ENZ wavelengths of 1335 nm and 1293 nm, respectively; while films deposited under O_2 and N_2 gas do not show any cutoff over the observed wavelength value. Such behavior is correlated to the increased carrier concentration due to the increase in oxygen vacancies of the ITO thin films as the background gas of the PLD chamber changes from O_2 gas to inert gases. In the same vein with the ENZ wavelengths, no resonance absorption is observed experimentally for either of the films deposited under O_2 or N_2. In contrast, both PLD-ITO thin films under Ar and He shows distinct resonant dips just over the ENZ wavelengths for all the incident angles. However, the ENZ plasmon resonance wavelengths remain relatively invariant to the change in incident angles. This angular invariancy feature of ENZ plasmon resonance is explained on the basis of electric field localization over a narrow wavelength domain. Experimentally observed absorption intensity reached as high as 95.68% and 98.98% for ITO thin films deposited under Ar and He gases, respectively. The difference in the LFIEF values at the resonance wavelengths of these films is responsible for this difference in absorption intensity. Moreover, a modified TMM matrix method that incorporates the surface roughness effect through the application of

TH-2572_156121026

ABEMA is proposed, and thereby, the experimentally observed ENZ plasmon resonance is resolved numerically.

TH-2572_156121026

TH-2572_156121026

Chapter 4

Effect of Surface Roughness on the ENZ Plasmon Resonance Properties of Vacuum-deposited ITO films

Previous chapter discussed the effect different ambient gases, namely, O_2, N_2, Ar, and He on the ENZ plasmon resonance properties of pulsed laser deposited ITO thin films. However, high vacuum (pressure ~ 2×10^{-5} mbar) ambient condition was not included in that chapter because it results in highly rough ITO films, enriched in particulates of random sizes and shapes. As discussed in Section 1.7 of Chapter 1, there are numerous reports on the effect of surface roughness on the SPR properties of metal films [139-144],. In contrast, surface roughness effect is hardly being explored in the context of ENZ plasmon resonance. The main difference between SPR occurring in metals and CPR occurring in ENZ materials is that the latter group of materials have significantly less permittivity value than the former. Thus, the necessary approximations on permittivity that goes into the derivations related to the surface roughness effect on the metallic films will not be applicable here. Javani *et al.* have pointed out the stark difference between the observed loss function in plasmonics resonances for both these situations [170]. They also added that singularly enhanced loss inside the ENZ material negates the field intensity localization factor, which is paramount in the case of rough metallic surfaces [19]. Though this standalone report presents some remarkable insights based on theoretical grounds, a detailed experimental demonstration of the effects of the surface roughness on the resonance response of the ENZ media is not well reported in the literature. Experimental studies on surface roughness modified ENZ modes could reveal fascinating physical insights to this exciting field. Such an eye-catching prospect acts as a strong motivating factor in studying the evolution of ENZ modes through the increasing surface roughness in-depth.

TH-2572_156121026

The primary hurdle for any research based on the electromagnetic resonance response of rough films is to hand-pick a scrupulous numerical model that can accurately describe the experimentally obtained data. Moreover, in the case of randomly rough surface, complicacy of the problem increases manifold due to the electromagnetic scattering driven dissimilarities to the normal Fresnel description. In this regard, numerical simulation algorithms like finite difference time domain method (FDTD) [171], finite-element method (FEM) [172], rigorous coupled-wave analysis (RCWA) [173], 2.5D technique [174],etc., have been employed to describe the optical response of randomly rough surfaces. Despite the fact that these simulation algorithms provide an exact solution to Maxwell's equations, they are computationally intensive. In contrast, effective medium approximations (EMAs) offers a more computationally inexpensive solution to the problem while maintaining a reasonable level of accuracy [153, 175]. Among two of the widely popular EMAs, i.e., Maxwell-Garnet [176] and Bruggeman effective medium approximation (BEMA) [177], the later one, when collabed with the anisotropic description of the constituents (termed as ABEMA), is found to be very effective in characterizing highly ordered roughness of slanted columnar thin films [151]. Though, ABEMA was developed originally for these ordered surface features, it is found very useful in describing the optical features of gratings with randomly rough edges [153]. Thus, ABEMA could prove to be an extremely effective tool for optical characterization of randomly rough ITO thin films, especially in the case of SE data fitting.

As discussed in subsection 1.5.3 of Chapter 1, PA of an electromagnetic wave has many exotic applications, and thus has been focus of intense research for over two decades now. PA has been demonstrated in plathora of material platforms such as metamaterials [178, 179], metal-dielectric-metal stacks [180], low permittivity ENZ films [105, 106], etc. But such a high value of directional absorption is particularly unlikely in rough thin films; be it metallic or the ENZ ones. Scattering is expected to take over as the dominating mechanism as for the light-matter interaction of the highly rough film is concerned [181].

In this chapter, the surface roughness dependent ENZ plasmon resonance response of ITO films deposited at different deposition time under vacuum environment of PLD is explored and an absorption value of 99.75% is demonstrated for the film deposited for highest deposition time. The SE data of the vacuum-deposited ITO thin films having high degree random surface

TH-2572_156121026

roughness has been successfully modeled by employing this ABEMA model. Subsequently, a modified TMM formulation, taking into the ABEMA contribution, has been developed for the faithful numerical recreation of the experimental reflection data obtained from the randomly rough ITO thin films. Layer-by-layer analysis of electric field enhancement and absorption loss density presented in connection to this helps in interpreting the underlying physics behind such a strong absorption observed in the vacuum deposited samples. In addition to this, the revised ENZ mode description for four-layer system, in which surface roughness is included as an anisotropic layer along with the isotropic thin film layer, is presented and the PA is identified as the outcome of the crossover between internal and radiation damping contributions that come out as the byproduct of this modified dispersion relation.

4.1 Experimental Details and Characterization Techniques

10 wt.% SnO_2 doped ITO pellets were used to deposit thin films of different thicknesses under a high vacuum environment (pressure ≈ 2×10^{-5} mbar) by varying the deposition time. Substrate temperature and target-to substrate distance were kept at 400°C and 3.5 cm, respectively. Other important aspects of deposition procedure are discussed in details in Chapter 2. The nomenclature of three sets of samples is done based on different deposition times; namely, film deposited for 20 min is termed as S1, 40 min as S2, and 80 min as S3.

A combination of Drude model and Lorentz oscillators was used to model the SE data in order to obtain the dielectric permittivity over the wavelength range of 220 – 1700 nm. Film thickness and surface roughness values determined from the same analysis were then used throughout the work. More details about the ellipsometric modeling are discussed in subsequent sections. Root-mean-square (RMS) roughness determined by the AFM is being utilized to verify surface roughness values obtained from SE analysis. Surface behavior of the films were studied by analyzing FESEM images. Quantitative crystallographic phase analysis was achieved by performing Rietveld refinement operation over the XRD data. Conductivity and carrier concentration of the films were determined by four-probe method and Hall measurement, respectively. The experimental measurement of ENZ plasmon resonance signal was done in SE instrument by employing K-R geometry. The schematic of the K-R setup is shown in the inset of Figure 2-9 and other important details are enumerated in Section 2.3 of Chapter 2. The incident angle outside the prism was varied from 50° to 70° in a step of 1°, and

TH-2572_156121026

the reflected data was collected using a NIR detector over the wavelength range of 900 – 1700 nm.

4.2 Experimental Results and Retails of Ellipsometry Analysis

4.2.1 Structural, morphological and electrical properties of vacuum-deposited ITO thin films

Figure 4-1 depicts the observed XRD pattern for all the samples. It is clear that all the samples are polycrystalline with the preferred orientation along (222) direction. Most of the peaks are assigned to the pristine ITO phase (PDF Card No.: 01-089-4598) that corresponds to cubic bixbyite nature of In_2O_3 crystal. However, there is one extra peak at 32.9°, which is identified as the peak for the metallic indium phase (PDF Card No.: 01-070-2888). As discussed in Chapter 1, the presence of metallic indium phase is nothing new for oxygen deficient ITO films and it is already being reported for pulsed deposited ITO thin films under vacuum environment [134, 135]. Double phase Rietveld refinement operation was performed to extract each phase's contribution quantitatively. As can be seen from the figure, the calculated and observed pattern matches quite well. The metallic indium percentage increases

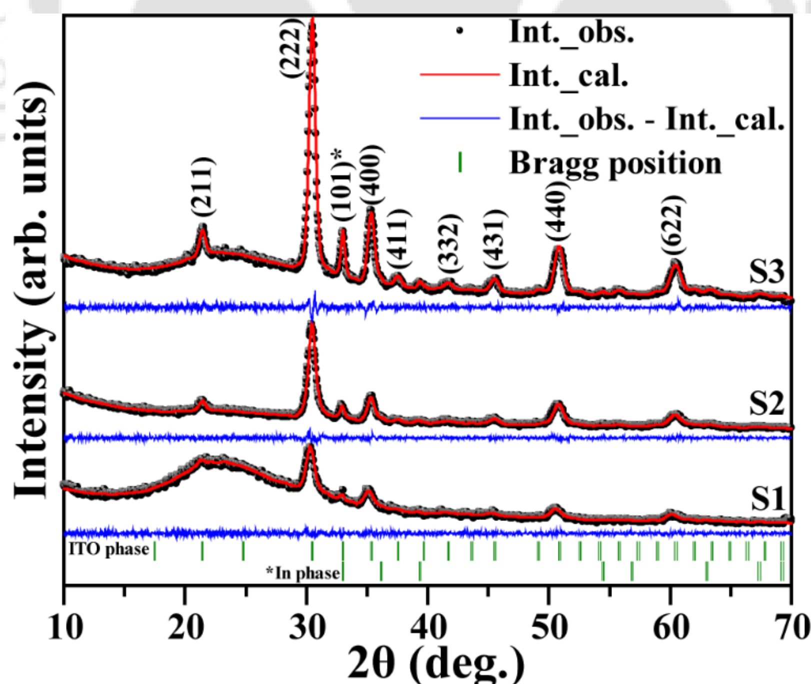

Figure 4-1. Rietveld refined the XRD pattern for all the samples in the range of 2θ values from 10° to 70°.

TH-2572_156121026

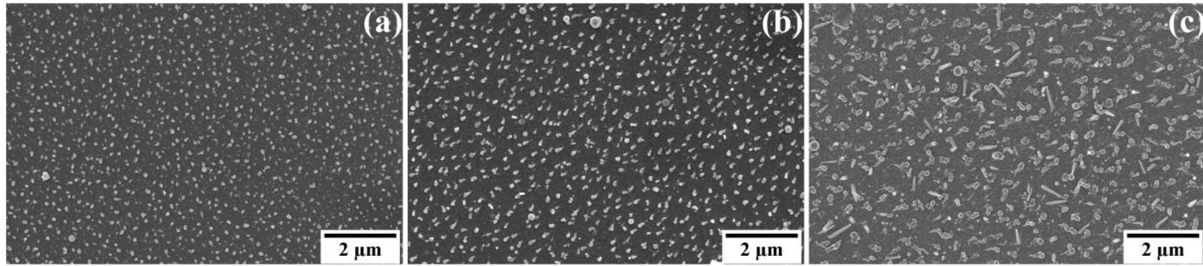

Figure 4-2. Acquired FESEM images of vacuum-deposited ITO thin films for different deposition times: (a) S1 (20 min); (b) S2 (40 min); (c) S3 (80 min).

monotonically from (3.11 ± 1.89) % to (8.48 ± 0.29) % for sample S1 to S3. This value is certainly not negligible; hence metallic indium contribution should be kept in mind while discussing any physically observable quantity from the vacuum-deposited ITO films.

FESEM images of all samples, presented in Figure 4-2, revealed the presence of particulates of different sizes and shapes. Sample S1, having the lowest overall thickness, mostly consisting of spherical particulates formed inherently from solidified liquid ejecta. As the deposition time is increased, more and more random sized particulates start to appear; especially sample S3 is enriched with particulates having variety of size and shape, ranging from rods to agglomerated spheres distributed over all kinds of random orientations. Such peculiar surface features can be explained on the basis of two competing mechanisms – (i) solidification of liquid droplets formed due to the exertion of recoil pressure on the transient melt just below the laser focus spot, and (ii) ejection of sub-micrometer sized particulates due to the repeated irradiation of the target over a long period of time, a process termed as "exfoliation" [146]. In a high vacuum environment, plasma plume containing highly energetic particles/particulates reaches the substrate without encountering any severe collisions on the way [130]. Thereby, only the substrate heating can modify the size and shape of the particulates by invoking coalescence and surface diffusion processes.

AFM images of all the vacuum-deposited ITO thin films are shown in Figure 4-3. (a) – (c). It is clearly observed that these micrographs are in perfect harmony with the surface images of the samples acquired by FESEM. The particulates size and shape distribution changes abruptly with the deposition time. In this context, RMS surface roughness increases linearly from 17.6 ± 3.2 nm to 29.7 ± 6.2 nm and then to 58.1 ± 14.4 nm from lowest to highest deposition time for ITO films deposited under vacuum environment.

TH-2572_156121026

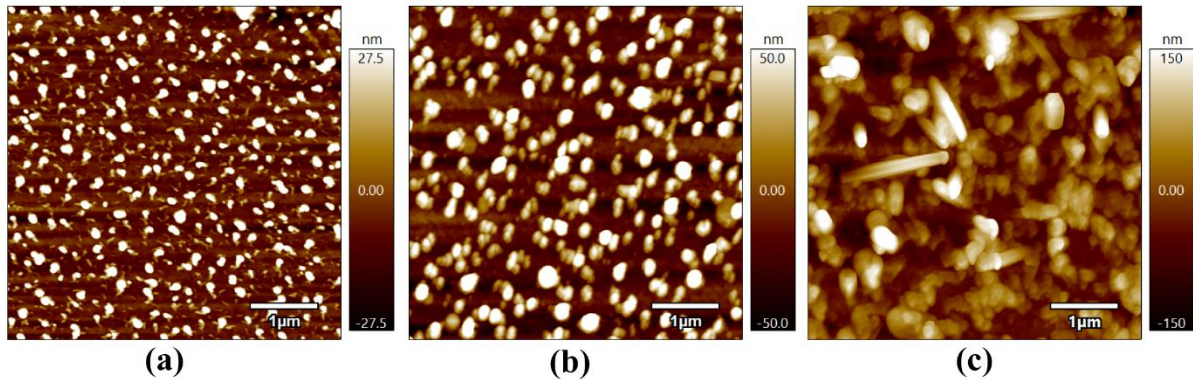

Figure 4-3. 2D view of AFM micrographs taken over a surface area of 5×5 μm for ITO films at different deposition times: (a) S1 (20 min); (b) S2 (40 min); (c) S3 (80 min).

Figure 4-4 depicts the Hall resistance (R_{xy}) measured at different applied magnetic fields for the S3 sample. To compare the results with the standard material, we have also taken Hall measurements for Silver (Ag) film (Sputtered film at room temperature, thickness: ~ 50 nm) and pure ITO film (pulsed laser deposited film at 400°C under N_2 gas pressure of 0.01 mbar, thickness: 70 nm) and included in Figure 4-4. It is observed that all the films have *n*-type conductivity, and hence electron is the primary carrier. The Hall resistivity of the metallic

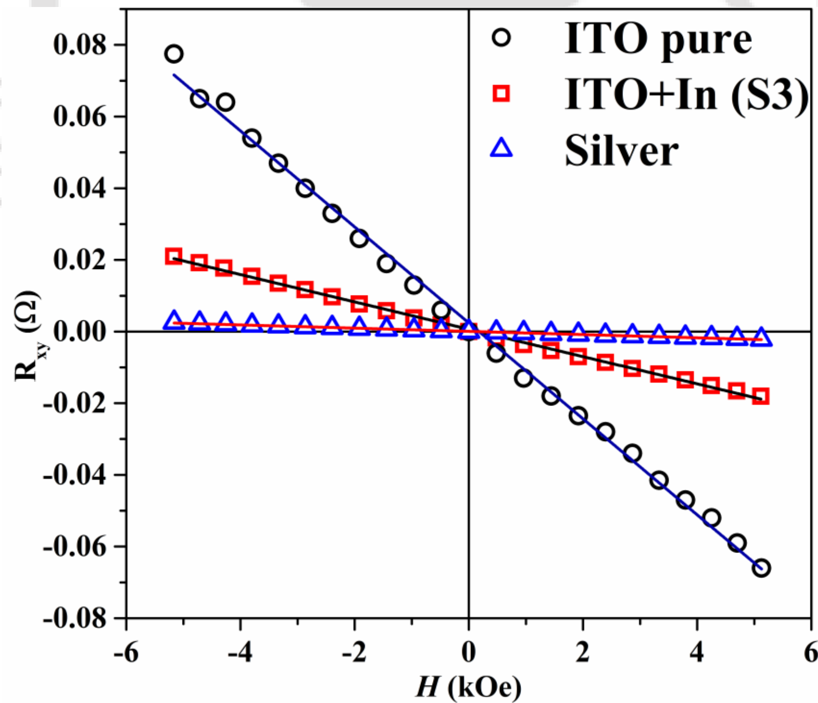

Figure 4-4. Variation of Hall resistance, Rxy with the applied magnetic field for ITO pure (black circle), sample S3 (red square), and silver film (blue triangle).

TH-2572_156121026

indium-rich ITO films is considerably deviated from the pure ITO film and tends to be quite similar to the Ag film. The calculated carrier concentration turns out to be $2.78\times10^{21}/cm^3$, $2.34\times10^{21}/cm^{3,}$ and $6.66\times10^{20}/cm^3$ for Ag, indium rich ITO (S3), and pure ITO films, respectively. Similarly, the carrier concentration of other vacuum-deposited ITO films is around $2.35\times10^{21}/cm^3$ for S1 and $3.15\times10^{21}/cm^3$ for S2. All the metallic indium-rich ITO films have nearly one order higher carrier concentration than pure ITO film. The large number of free electrons generated from the oxygen vacancies is responsible for such a high value of carrier concentration. Additionally, the sheet conductivity value of these metallic indium-rich ITO films is around 3.76×10^5 S/m (S1), 4.35×10^5 S/m (S2), and 6.71×10^5 S/m (S3). Thus, almost metal-like conductivity is achieved in these vacuum deposited ITO films despite having a very high degree of surface roughness, which is known to adversely affect the electron conduction inside the film through electron scattering [168]. Even for rough metallic films and metallic nanostructures, conductivity values are usually in the range of ~10^5 S/m [182, 183], which is reasonably less than the bulk values (~ 10^6 S/m).

4.2.2 Experimental reflection spectra of randomly rough ITO film surface

Experimentally observed ENZ plasmon resonance for vacuum-deposited ITO thin films at different deposition time is as shown in Figure 4-5. (a)–(c). It is clear that the resonance dip position for all the samples remains fairly constant within 1330 to 1340 nm and the overall features are also relatively invariant to incident angles. These two arguments, i.e., invariancy

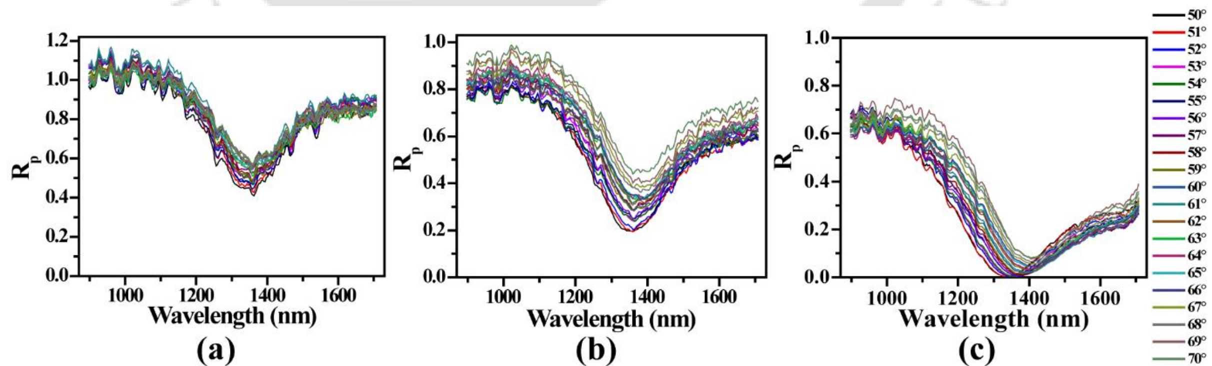

Figure 4-5. Experimentally measured reflection spectra over the wavelength range of 900 – 1700 nm for the samples: (a) S1; (b) S2; (c) S3. Color codes of various incidence angles (from 50° to 70°) are given over the right hand side of the figure.

TH-2572_156121026

to incident angles and size/shapes of particulates, establish that the observed resonance behavior in randomly rough ITO thin films used in the present work is governed by CPs; not due to SPs or localized surface plasmons (LSPs) [111, 184]. Consequently, the dip observed in the reflection spectra is the manifestation of the excitation of these CPs (ENZ plasmons), termed as CPR (ENZ plasmon resonance). Note that the available literature on ENZ plasmon resonance is for smooth films [110] or nanostructures [111] with flat interfaces on each side. In the present work, however, vacuum-deposited particulates having random sizes and shapes are being used for the analysis. Thus, the existence of plasmons, specifically CPs, in such randomized structures may sound somewhat surprising. However, these individual particulates can be considered as distinct capacitors such that the charge stored in such local capacitors gives rise to CPs; in spite of the fact that one of the plates (upper surface of particulates) is not ideal but has random termination. Coming back to the reflection spectra for pulsed laser deposited ITO films, it is observed that the depth of the resonance increases monotonically with the deposition time. The transmission (T) in K–R geometry can be neglected since it is based on the attenuated total reflection (ATR) condition. Thus, the absorption (A) inside the film can be written in terms of reflection (R) as, $A = 1 - R$. Now, it is observed that sample S3 with highest overall thickness exhibits about 99.75% absorption at the wavelength of 1335 nm for the incidence angle of 50°, while the sample S1 and S2 shows absorption values of 55.20% at 1337 nm and 80.24% at 1341 nm, respectively for the same incidence angle. Maximum plasma absorption in sample S3 is in line with the concept of local capacitors. The number of CPs are expected be maximized for larger surface areas of bigger particulates. In order to gather sufficient physical insight into the ENZ response of the randomly rough ITO thin films, a numerical simulation method containing the information about the complicated surface features as an effective medium is developed. All the basic features of the numerical approach and the inevitable assumptions that comes with it will be discussed in great detail in the following section.

4.2.3 Ellipsometry modeling

It is quite a tedious task to effectively frame the structural skeleton of these randomly rough films, having such a high degree of surface non-uniformities, in commonly used Jones matrix-based SE. In this context, Mueller matrix ellipsometry proves to be an efficient

TH-2572_156121026

characterization tool for randomly rough surfaces [185, 186]. However, it requires special skillsets to handle and extract valuable information from Mueller matrix-generated data. In addition to that, formulation of a numerical model around these matrices that can effectively simulate the reflection and transmission coefficients obtained from a multilayered structure is a tough ask itself. Contrary to this, a simple optical model is developed, bearing two major approximations, for an accurate assessment of the regular ellipsometric data in the case of highly rough ITO thin films. Firstly, randomly sized and shaped particulates (viewed as local capacitors as per the concept of CPR) are approximated as perfect electrical conductor (PEC) individually. This approximation is based on the fact that ITO films are rich in metallic indium. In the present work, Rietveld refined XRD data for all the films (Figure 4-1) provides a concrete testimonial about the indium phase inclusion in the ITO matrix. Indium (In), being a group IIIA metal, exhibits plasma wavelength (E_p) deep into the UV ($E_p \approx 11.6$ eV (93560 cm^{-1})), and thus, behaves as a perfect reflector to ITO having plasma wavelength ≈ 2 eV (16131 cm^{-1}) in the context of excitation of CPs over the NIR region. A similar approach was also followed by Franzen *et al.* while explaining the complete dominance of CPR of ITO in an ITO-Au hybrid structure [110]. This scenario is indeed true in the present work also, where it is observed that the CPR of ITO completely dominates the reflectivity spectra of metallic indium-rich ITO films. Note that here it is not claimed that PEC condition is valid for vacuum-deposited ITO films as a whole, which it is surely not, as suggested by the electrical measurements presented in Subsection 4.2.1. But, instead, the argument is that PEC is applicable to the discretized particulates of metallic indium-rich ITO hybrids, separated by voids. The second assumption is that particulates of random size and shape scattered all over the surface are approximated to be elongated ellipses of the same size equally distributed to form the surface roughness layer. As discussed earlier, the electric field is relatively averaged out over the rough surface in an idealized ENZ film [170]. Thus EMA, based on the concept of field averaging led homogenization principle [187], seems to be quite a reasonable starting ground for understanding the optical response of randomly rough ITO thin films. Having said that, commonly used BEMA is relatively unproductive in describing the nonspherical size aspect of the surface roughness constituents. In this regard, ABEMA was applied to take into account the random size effect of the particulates. The mathematical representation of ABEMA is given in eqn. (2.12) and parameters are described in section 2.2 of Chapter 2.

TH-2572_156121026

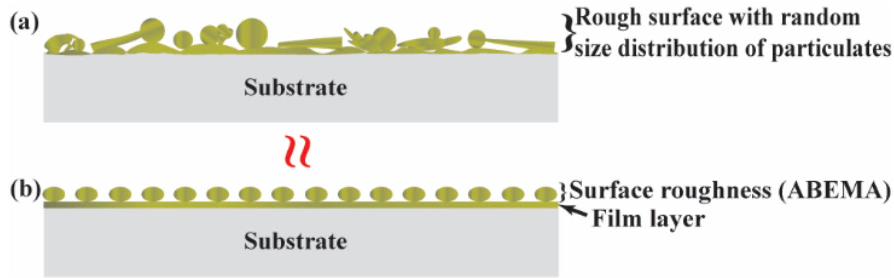

Figure 4-6. (a) Pictorial representation of the random sized and shaped particulates observed in the FESEM image of the sample S3; (b) The simplified version of the structure in figure (a) is obtained through the application of the ABEMA model.

Figure 4-6 represents a schematic of the structural approximation procedure that goes into the ellipsometer modeling of such films. A rough surface with a random size distribution of the particulates is approximated as a combination of two layers: one interface layer and the other is surface roughness layer determined by ABEMA. As shown in Figure 4-7, the proposed ellipsometer model of film + surface roughness layer is able to fit the experimentally observed real and imaginary part of pseudo dielectric permittivity perfectly. Pseudo-dielectric permittivity ($\langle \varepsilon \rangle$) is a common representation of SE data [148] and is given in equation 2.6. Here, the ellipsometry data is fitted over the whole wavelength range permitted by the instrument, i.e., 220 – 1700 nm, not in the NIR region only in order to extract maximum information as accurately as possible.

All critical parameters extracted from the SE analysis and the corresponding parameters of DL model [148] are listed in Table 4-1. Zero value of the Drude scattering frequency (E_Γ) ensures the pre-applied PEC conditions to individual particulates through the application of

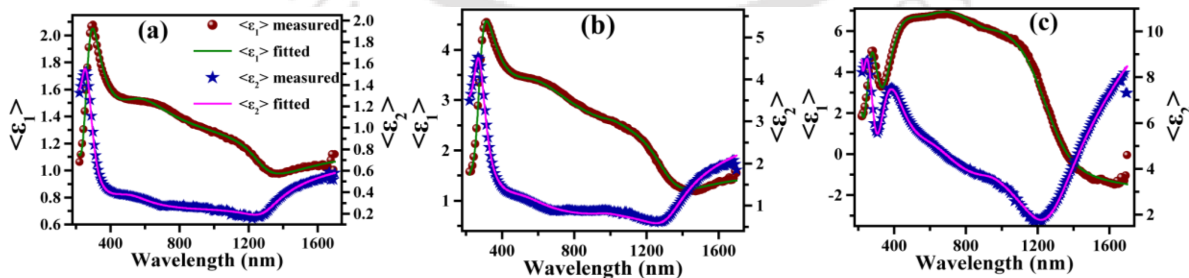

Figure 4-7. Variation of the measured and fitted spectra of the real ($\langle \varepsilon_1 \rangle$) and imaginary ($\langle \varepsilon_2 \rangle$) part of pseudo-dielectric permittivity over the wavelength range of 220 – 1700 nm for vacuum-deposited at different deposition times: (a) S1 (20 min); (b) S2 (40 min); (c) S3 (80 min).

TH-2572_156121026

Table 4-1. The list of parameters acquired from SE data fitting for all the vacuum deposited ITO thin films. The last 3 rows are SE fitting parameters for sample S3 at different Drude scattering frequency values, i.e. E_Γ =0, E_Γ =0.05, and E_Γ =0.1. In the table, four Lorentz oscillators are designated by 1st, 2nd, 3rd, and 4th. Oscillator strength (f), central position (E_0), and width (Γ) is given for each oscillators. Uncertainties associated with different parameters are also reported. Note that, SR stands for surface roughness.

Name	Film thick. (nm)	SR (nm)	ABEMA parameters		Drude model		Lorentz oscillators												RMSE
			Depol. coefficient (L_z)	Void %	E_p (eV)	E_Γ (eV)	1st			2nd			3rd			4th			
							f	E_0 (eV)	Γ (eV)	f	E_0 (eV)	Γ (eV)	f	E_0 (eV)	Γ (eV)	f	E_0 (eV)	Γ (eV)	
S1	×	15.8	0.325 ± 0.021	26	2.04 ± 0.05	0	2.69 ± 0.13	6.89 ± 0.11	5.48 ± 0.42	0.73 ± 0.06	4.59 ± 0.02	1.41 ± 0.04	0.94 ± 0.06	2.16 ± 0.01	1.46 ± 0.05	×	×	×	0.014
S2	×	26.1	0.441 ± 0.010	16	1.94 ± 0.03	0	2.56± 0.11	7.75 ± 0.20	5.81 ± 0.58	0.81 ± 0.06	4.61 ± 0.02	1.46 ± 0.05	0.81 ± 0.06	2.24 ± 0.02	1.84 ± 0.08	0.07 ± 0.01	1.25 ± 0.01	0.26 ± 0.03	0.041
S3	19.7	49.7	0.406 ± 0.007	43	1.88 ± 0.02	0	0.33 ± 0.04	5.85 ± 0.02	0.56 ± 0.07	2.60 ± 0.06	4.82 ± 0.01	1.99 ± 0.03	0.49 ± 0.05	1.98 ± 0.02	1.41 ± 0.08	0.11 ± 0.02	1.30 ± 0.01	0.38 ± 0.04	0.127
	22	50.4	0.398 ± 0.009	42	1.75 ± 0.02	0.05	0.39 ± 0.04	5.93 ± 0.03	0.67 ± 0.10	2.29 ± 0.06	4.82 ± 0.02	1.99 ± 0.03	0.27 ± 0.06	1.98 ± 0.02	1.11 ± 0.11	0.09 ± 0.02	1.30 ± 0.01	0.33 ± 0.05	0.140
	25.3	50	0.399 ± 0.012	40	1.62 ± 0.03	0.10	0.53 ± 0.06	6.07 ± 0.04	0.99 ± 0.15	1.92 ± 0.08	4.79 ± 0.02	1.92 ± 0.04	0.15 ± 0.06	2.00 ± 0.02	0.89 ± 0.17	0.07 ± 0.02	1.30 ± 0.01	0.28 ± 0.06	0.164

TH-2572_156121026

ABEMA; bearing in mind that E_Γ is inversely related to the conductivity (σ) via the relation: $\sigma = \frac{\varepsilon_0 E_P^2}{E_\Gamma \hbar}$, where ε_0 is the free space permittivity, E_P is the plasma energy and $\hbar$ is the reduced Plank's constant. In EMA, only the metallic part among a heterogeneous mixture (air + metallic indium-rich ITO in the present case) is considered while applying the Drude model. Thereby, taking $E_\Gamma = 0$ for these local capacitors does not mean that $E_\Gamma = 0$ is valid for the whole film. Thus, PEC approximation in discrete local capacitors does not violate any physical restriction like the existence of finite mobility in a material [188]. By further analyzing the Lorentzian part of the DL model, the definite presence of the oscillators in and around the energy values 1.3 and 2 eV are linked to the metallic indium-related interband absorptions [189, 190]. In addition to that, two Lorentzian oscillators situated at the UV range represents the bandgap absorption region of the dominating ITO phase [191]. It is observed that the films with low deposition time, i.e., S1 and S2, does not show any uniform buffer layer. In contrast, two-layer system, consisting of a thin interface layer and surface roughness layer on top of it, is being considered for the film deposited for the highest time, i.e., S3. This particular surface growth characteristic mimics the metallic film growth mechanism via PLD [130]. It transforms from Volmer-Weber to layer-plus-island type as the deposition time is increased further. Surface roughness values predicted from ellipsometry nearly resemble the one obtained from AFM measurement, as shown in Figure 4-3.

Another interesting thing to note from ellipsometry analysis is that the depolarization coefficient, L_z changes from 0.325 to 0.441 for sample S1 to S2, indicating a distinct shift from spherical nature. As the deposition is increased further, L_z takes a slight dip, though the value is considerably away from the spherical one, i.e. 0.333. Also, the void percentage in the films is strikingly different from the 50-50 description of BEMA [191]. FESEM and AFM images provide a visual confirmation of the change in structural characteristics with the deposition time. Figure 4-8 depicts the variation of the real and imaginary part of the permittivity for all films over the wavelength range of 300 – 1700 nm. Almost similar ENZ wavelength for samples S1 and S2 indicates towards the saturation of the number of oxygen vacancies that act as main contributor to the free electron density in the vacuum deposited films [88]. In contrast, sample S3 exhibits a slightly lower cutoff at 1278 nm, though the number of oxygen vacancies

TH-2572_156121026

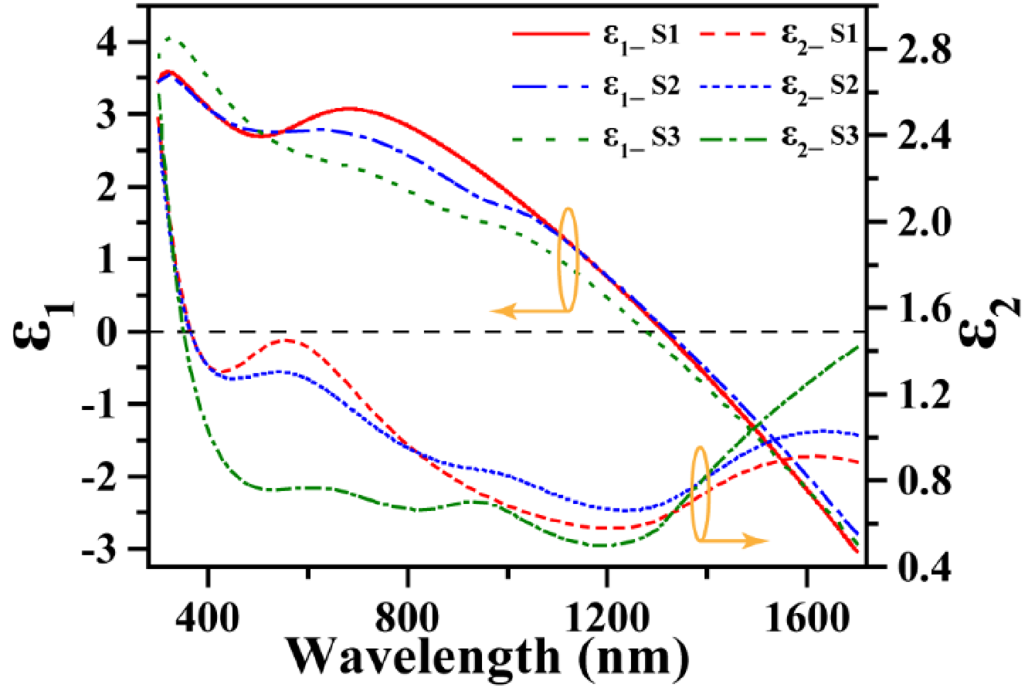

Figure 4-8. Variation of the real (ε_1) and imaginary part of the permittivity (ε_2) in the wavelength range of 300 – 1700 nm with the deposition time for the vacuum deposited ITO films. The black dashed line along the middle represents the zero value of the real part of the permittivity.

should be the same for all the samples theoretically. This may be due to the more metallic indium richness of sample S3 compared to other samples. Almost similar value of the imaginary part of permittivity observed at the ENZ wavelength for all the samples may look confusing, especially considering the fact that these samples have a widely variable degree of absorption as shown in Figure 4-5. Note that the imaginary part of the permittivity only controls the internal absorption inside the thin film. However, for similar internal absorption values of all the samples, the total absorption due to the ENZ plasmon resonance is mainly influenced by the back-scattered field [19]. This backscattered radiation loss in the film-air interface decreases as the film thickness increases. Thereby, the coupling between the incident field and ENZ plasmon also increases. Thus, the absorption due to the resonance increases significantly as the thickness of the sample increase from S1 to S3. Low value of the imaginary part of the permittivity in and around the cutoff region indicates the superiority of these films as ENZ-based platforms [70]. Additionally, the peaks related to the metallic indium generated inetrbands are also quite evident from the variation of the imaginary part of the permittivity in the visible range.

TH-2572_156121026

4.3 Description and results of numerical analysis

Details of theoretical formulation for numerical simulation are described meticulously in Chapter 2. Discussion for TM-polarized light given in that chapter is applicable for the analysis of ENZ plasmon resonance. The excitation geometry in this case consists of as many as five layers; namely, prism, substrate, film, surface roughness layer, and air, which are represented pictorially in Figure 2.10. However, in the actual Matlab script, substrate and prism, both having almost identical refractive index values, were assumed to be one single layer of BK-7 glass as a whole for the sake of simplification. Reference *nk*-file of the BK-7 glass, available in the SEA software (*SEA v1.0.4*) library, was applied to reproduce the dispersion behavior of the same. The ITO film layer was modeled using the values given in Table 4-1 for the DL model. The surface roughness of the film was integrated into the simulation as a continuous medium of ABEMA layer with a thickness equal to the surface roughness value, as determined by ellipsometry analysis. All three partial dielectric constants of this anisotropic layer were calculated numerically by treating Eq. (2.4 as quadratic in nature. The dielectric constant of air was taken as unity.

In Figure 4-9. (a), three plausible numerical models have been explored for fitting the experimentally measured ENZ plasmon resonance spectra at the incident angle of 50° for the sample S3. The first model consists of anisotropic surface roughness on top of the isotropic thin film layer, as discussed in the subsection 4.2.3. The possibility of any thin film layer is discarded in the second consideration and the sample S3 is treated as an island film (similar to S1 and S2) modeled by applying ABEMA. The parameters used for ellipsometer modeling of sample S3 as an island film are listed in Table 4-2. In the numerical model proposed by Katsidis *et al.* [192], surface roughness was incorporated into the transfer matrix as a partially coherent

Table 4-2. SE fitting parameters for the sample S3 considering only the surface roughness layer.

Sample name	SR (nm)	ABEMA parameters		Drude model		Lorentz oscillators central energy (eV)				
		Depolarization coefficient (Lz)	Void %	Ep (eV)	$E\Gamma$ (eV)	1st	2nd	3rd	4th	5th
S3	92.5	0.451 ± 0.005	37	1.96 ± 0.02	0	5.98 ± 0.03	4.82 ± 0.02	3.24 ± 0.01	2.00 ± 0.02	1.36 ± 0.02

TH-2572_156121026

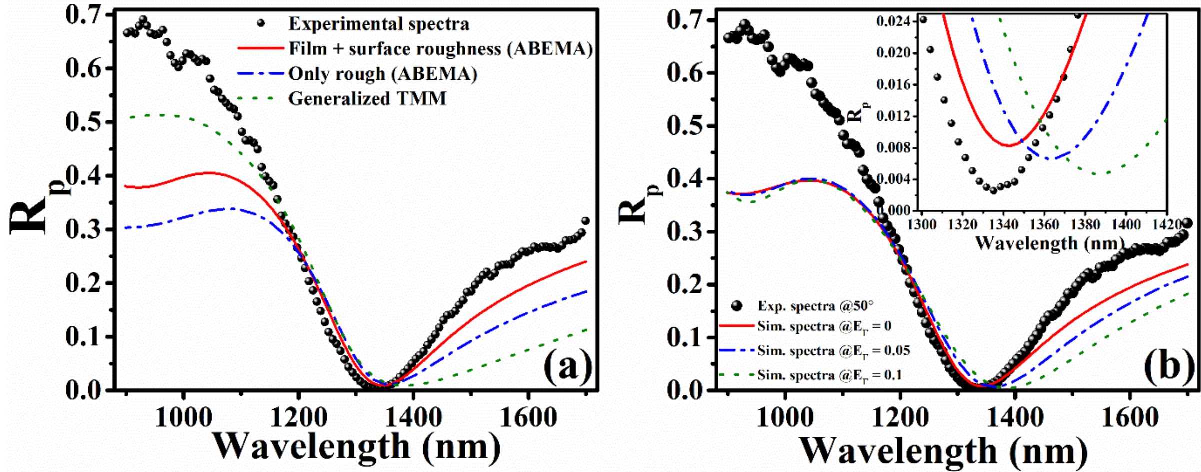

Figure 4-9. (a) Comparison of the experimentally measured reflection spectra (black solid spheres) with the simulated spectra for the sample S3 at the incidence angle 50° using three plausible fitting arguments: (i) film + surface roughness (solid red line); (ii) single surface roughness layer described by ABEMA (parameters are given in Table SI1) (dash-dot blue line); (iii) Film + surface roughness layer simulated by employing the procedure described in the ref. [192] (dotted olive line); (b) Comparison of experimental (black sphere) and simulated ENZ plasmon resonance spectra for sample S3 at different Drude scattering frequency values: $E_\Gamma = 0$ (red solid curve), $E_\Gamma = 0.05$ (blue dash-dot curve), $E_\Gamma = 0.1$ (dotted olive curve). Inset shows the expanded view of the experimental vs. simulated spectra near resonance values.

layer having Gaussian-shaped irregularities. As evident from Figure 4-9. (a), model used in the present work performed very well in describing the overall features of the experimentally obtained spectra as compared to the other ones. In order to explore the effect of the Drude scattering frequency (E_Γ) on the fitting quality of the numerical model, the numerical fits at the E_Γ values: 0, 0.05, and 0.1 eV is compared with the experimental ENZ plasmon spectra in Figure 4-9. (b). It is observed that PEC approximation applied on the Drude scattering frequency for the individual particulates performs much better in terms of overall fit quality with the experimental data compared to other E_Γ values. For higher values of E_Γ, though the intensity agreement with the experimental data improves slightly, the resonance dip position red-shifts significantly. This investigation supports the inherent approximation that goes into the numerical analysis of the ENZ resonance response for randomly rough ITO thin films.

TMM derived simulated resonance spectra for all the vacuum-deposited films are presented in Figure 4-10. A very good agreement between the experimental and numerically simulated spectra is established. However, experimentally measured ENZ plasmon resonance

TH-2572_156121026

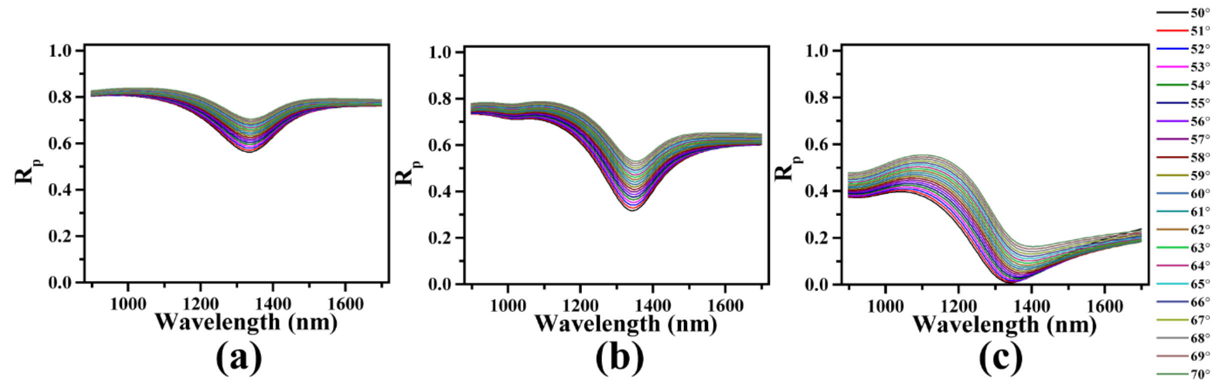

Figure 4-10. Numerically simulated reflection spectra for all the samples over the wavelength range of 900 – 1700 nm obtained by following the film + surface roughness (ABEMA) model: (a) S1; (b) S2; (c) S3. The color code for various angles is pasted on the right hand side of the figure.

for all the films are more profound than the simulated ones. This slight disagreement might be from the metallic inclusion of indium which is responsible for the slight enhancement of local field around the particulates [19]. ABEMA being a quasistatic approximation neglects any significant point-to-point variation of the electric field inside the layers [187], and thereby, unable to cope with these local field enhancements.

It is observed from both the experimental and numerical reflection data that the reflection (R) decreases, and thus the absorption (A) increases monotonically with the incident angle. Thereby, the absorption reaches its maximum at 50°. So there is a distinct possibility of even higher absorption for angles lower than 50°, though it is not viable experimentally in the present setup. Thus, the theoretical discussion must be extended to include the absorption features at lower angles. In this context, numerically simulated spectra over the incident angles 42° to 70° are replotted as a contour map in Figure 4-11. It is evident that absorption increases with the deposition time, as established earlier. Also, a far higher value of absorption compared to the experimentally measured one in the sample S3 is realized at an angle of 44.32°. An absorption value of 99.87% is observed at this angle at a considerably red- shifted wavelength of 1302 nm compared to the experimentally observed data, whereas, the highest absorption values achieved for the samples S1 and S2 are 45.22% and 73.08% at the wavelengths 1322 and 1330 nm, respectively at the incident angle of 42°. Investigation beyond this juncture is not meaningful because of the TIR requirement for the BK7 glass. Numerically obtained absorption values could be even higher in an actual experiment performed at exactly the same angle since the simulated absorption spectra lag behind the experimentally measured one in

TH-2572_156121026

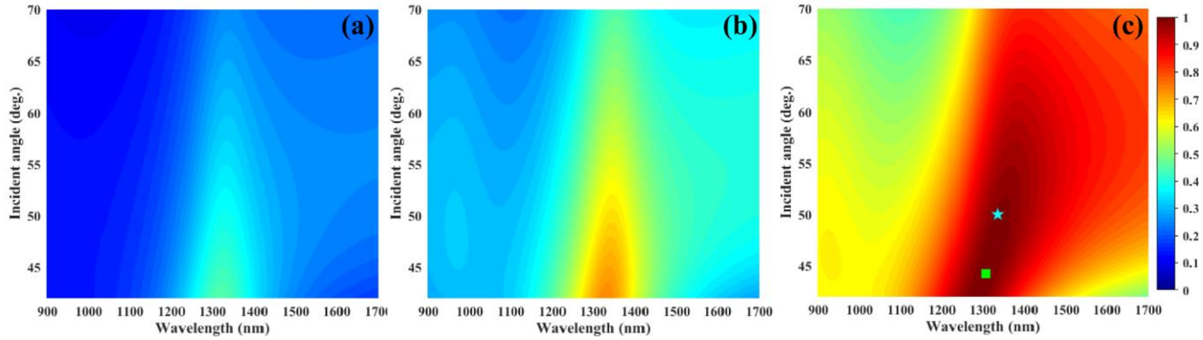

Figure 4-11. Color maps of the wavelength and angular dependency of absorption intensity (1 – reflection intensity) for the samples: (a) S1; (b) S2; (c) S3. The color bar stationed on the extreme right side of the figures represents the absorption intensity. In figure (c), the cyan star at the wavelength 1335 nm and green square at the wavelength 1306 nm imply the experimentally and numerically obtained PA points at the incident angle 50° and 44.32°, respectively, for the sample S3.

terms of intensity. It is quite captivating to note that this huge surge in surface roughness with the deposition time only affects the depth of the resonance while the peak position remains relatively unchanged. These results are clearly in great disparity with the previous reports on the consequence of surface roughness in metallic films, where a significant change in the position and the width of SPR was observed [19]. However, when it comes to metallic nanoparticles [193], a case study that is certainly more analogous to ours, random surface roughness was relatively ineffective in altering the absorption peak position related to the SPs. Such variation was attributed to the averaging out of the SPs over the random height fluctuations leading to smaller net effect. The same logic applies in the present work also. Next, the focus is shifted on understanding the physical origin of the PA in sample S3.

4.4 Origin of the PA in randomly rough ITO thin films

In order to gain deeper physical insights into the ENZ plasmon mediated PA in this highly rough film, layer-by-layer electric field distribution is depicted in Figure 4-12. (a). Strong enhancement of the electric field inside the film is realized in the vicinity of ENZ wavelength, a common feature in an ultrathin ENZ media [105, 106]. However, the highest electric field enhancement takes place almost exactly at the PA wavelength, which is in stark contrast with the earlier reports [105, 194]. This discrepancy is due to the presence of surface roughness on top of the pristine layer. Surface roughness having low but variable dielectric constant, as opposed to the typical air superstrate, heavily reshapes the electric field distribu-

TH-2572_156121026

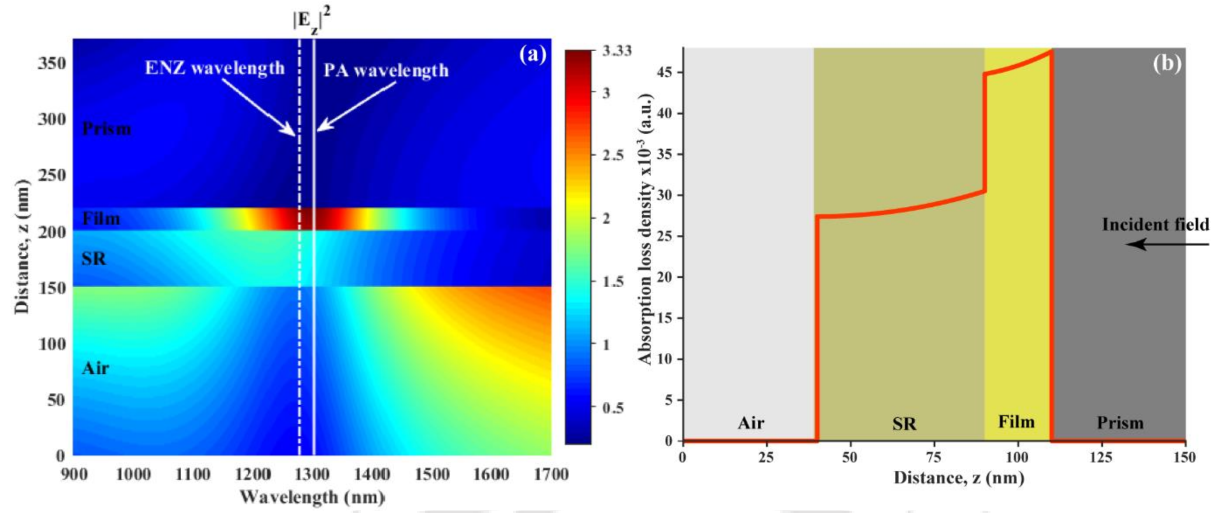

Figure 4-12. (a) Color map of the spatial distribution of the square of the amplitude of the electric field intensity along the z-direction over the wavelength range of 900 – 1700 nm for the sample S3. The dashed and solid white vertical lines represent the ENZ wavelength and numerically acquired PA wavelength, respectively. The color bar positioned at the right hand side indicates the value of the squared electric field amplitude. (b) Spatial distribution of the absorption loss density.

tion inside the film by exerting displacement continuity condition ($\varepsilon_{ITO} E_z^{ITO} = \varepsilon_a^z E_z^{SR}$). It is noteworthy that there is hardly any localized enhancement throughout the surface roughness layer, which once again consolidates the field averaging feature of EMA. High electric field enhancement observed in the longer wavelength is quite similar to that observed in the literature concerning excitation of ITO films via plain ATR geometry, without the use of any metallic backing plate [106]. To understand the source of PA, absorption loss inside every layer with surface area S is calculated as [195],

$$A_{LD} = \frac{\pi}{\lambda} \int_S Im\left\{ \varepsilon \left(|E_x|^2 + |E_z|^2 \right) \right\} dS \tag{4.1}$$

where *Im* denotes the imaginary part of the entire second bracketed term ε, the dielectric permittivity of each layer, is valued as ε_{ITO} and ε_a^z in the case of thin film and surface roughness layers, respectively. E_x and E_z are the electric fields in the *x*- and *z*-components of the electric field, respectively. The spatial variation of the absorption loss density calculated using Eq. (4.1) is shown in Figure 4-12. (b). Prism and air being dielectric materials, exhibit a flat line along the zero value. PA in the sample S3 can be understood in terms of the total area under the absorption loss density curve. For sample S3, the total area is 2.341 in arbitrary units. In comparison, the area under the absorption loss density curve for samples S1 and S2, as

TH-2572_156121026

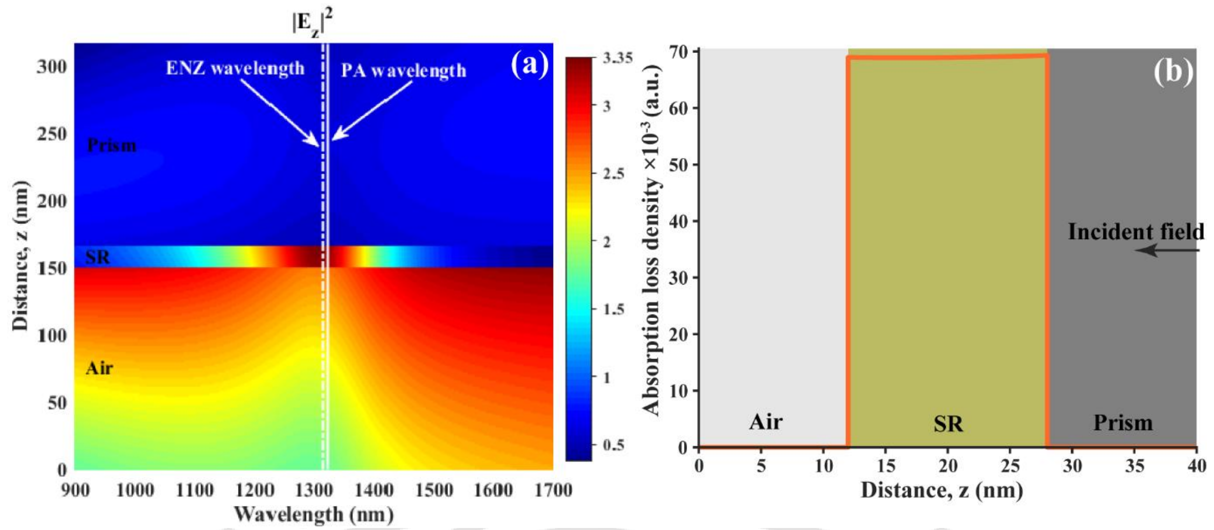

Figure 4-13. (a) Color map of the wavelength-wise and spatial distribution of the square of the amplitude of the electric field intensity along the z-direction for the sample S1. (b) Spatial distribution of the absorption loss density.

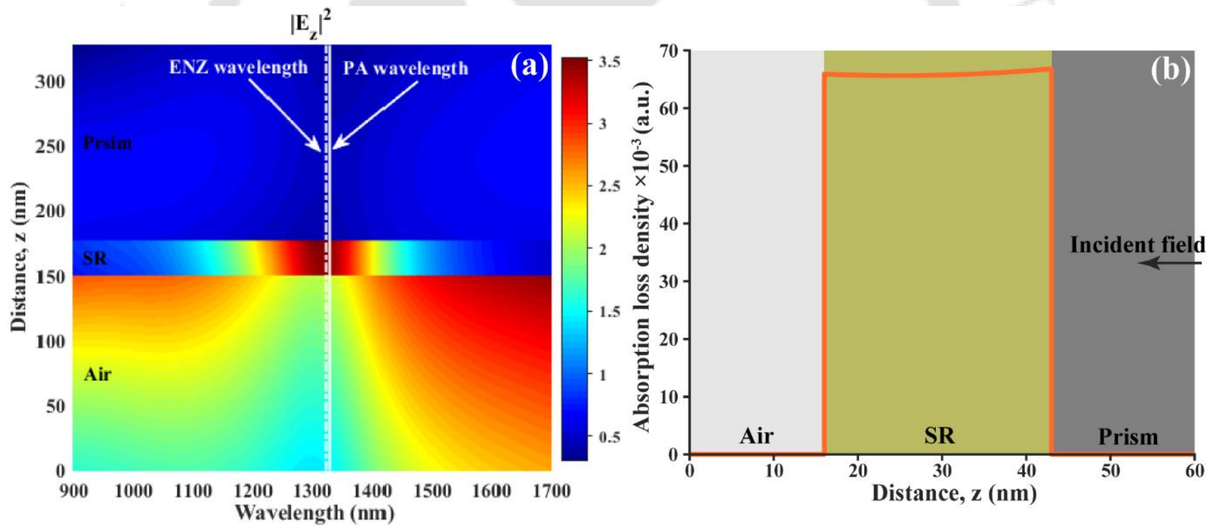

Figure 4-14. (a) Color map of the wavelength-wise and spatial distribution of the square of the amplitude of the electric field intensity along the z-direction for the sample S2. (b) Spatial distribution of the absorption loss density.

shown in Figure 4-13 and Figure 4-14, comes out to be 1.092 and 1.745, respectively. Thus, the sample with the maximum absorption loss exhibits the highest absorption values. But the most crucial part is that absorption loss is not exclusively limited to the ITO thin film layer, as suggested in the earlier work on ENZ plasmon mediated PA [105]. In fact, the maximum contribution to the total absorption loss (~61%) in the combined system occurs through the surface roughness path. Surface roughness acts as a supporting mechanism to the film layer

TH-2572_156121026

for absorption loss dissipation and helps immensely in achieving PA in highly rough ITO thin films. Besides, the gradual decline of the absorption loss density after crossing the interface for both film and surface roughness is in accordance with the earlier results [105, 196]. Electric field and the absorption loss density calculations were done with an open-sourced rigorous coupled wave analysis (RCWA) script [195].

4.5 Modified ENZ mode dispersion

Accurate interpretation of the electromagnetic *modes*, defined as the solution set for characteristic Fresnel equation in the absence of any kind of excitation, is an extremely powerful tool for understanding PA in ultra-thin films [105]. Mode description for the three layer ENZ film structure is well documented in the literature [197]. However, this straightforward equation needs to be modified in order to tackle the presence of an anisotropic surface roughness layer. In this context, the modified mode equation characterizing the ENZ behavior of a rough film is given by [198],

$$\begin{aligned}\frac{k_z^4}{\varepsilon_4}+\frac{k_z^2}{\varepsilon_2} &= i\tan\left(k_z^a d_3\right)\left(\frac{k_z^2 k_z^4}{k_z^a}\frac{\varepsilon_a^x}{\varepsilon_2\varepsilon_4}+\frac{k_z^a}{\varepsilon_a^x}\right)\\ &-\exp\left(2ik_z^2 d_2\right)\left[\left(\frac{k_z^2}{\varepsilon_2}-\frac{k_z^1}{\varepsilon_1}\right)\left(\frac{k_z^1}{\varepsilon_1}+\frac{k_z^2}{\varepsilon_2}\right)^{-1}\right]\left[\left(\frac{k_z^2}{\varepsilon_2}-\frac{k_z^4}{\varepsilon_4}\right)-i\tan\left(k_z^a d_3\right)\left(\frac{k_z^2 k_z^4}{k_z^a}\frac{\varepsilon_a^x}{\varepsilon_2\varepsilon_4}-\frac{k_z^a}{\varepsilon_a^x}\right)\right]\end{aligned} \tag{4.2}$$

where the sign convention is as per the ref. [199]. k_z^i and $k_z^{a,TM}$ are almost identical to that of Eq. (2.12); the only difference is that wave vector k_x and angular frequency ω are not known here and needs to be solved as a pair. 1 to 4 nomenclature are in a sequence from prism to air. The thickness of the film and surface roughness layers are designated as d_2 and d_3, respectively. Direct numerical solution of this complicated equation results in unphysical mode solutions irrespective of the choices made on real and complex values of k_x and ω [105]. In contrast, the analytical solution of Eq. (4.2) is already demonstrated in the literature with, of course, involvement of some degree of approximations [198, 199]. To the first order of d_2/λ and $\left|\exp\left(2ik_z^1 d_1\right)\right|$, complex-valued k_x can be calculated for real valued ω as [198],

$$k_x = k_{EP} + k_r + k_t \tag{4.3}$$

with

TH-2572_156121026

$$\left.\begin{aligned}
k_{EP} &= \left(\frac{\varepsilon_2\varepsilon_4}{\varepsilon_2+\varepsilon_4}\right)^{1/2}\frac{\omega}{c}\\
k_r &= \frac{\omega}{c}\left[\frac{k_z^2\varepsilon_1 - k_z^1\varepsilon_2}{k_z^2\varepsilon_1 + k_z^1\varepsilon_2}\right]_{k_x=k_{EP}}\left(\frac{2}{\varepsilon_4-\varepsilon_2}\right)\left(\frac{\varepsilon_2\varepsilon_4}{\varepsilon_2+\varepsilon_4}\right)^{3/2}\exp\left(i\frac{4\pi d_2}{\lambda}\frac{\varepsilon_2}{\left(\varepsilon_2+\varepsilon_4\right)^{1/2}}\right)\\
k_t &= i\left(\frac{2\pi d_3}{\lambda}\right)\left(\frac{\omega}{c}\right)\left(\frac{\varepsilon_2\varepsilon_4}{\varepsilon_2+\varepsilon_4}\right)^2\frac{1}{\left(\varepsilon_2\varepsilon_4\right)^{1/2}\left(\varepsilon_2-\varepsilon_4\right)}\left(\varepsilon_a^x+\frac{\varepsilon_2\varepsilon_4}{\varepsilon_a^z}-\varepsilon_2-\varepsilon_4\right)
\end{aligned}\right\} \quad (4.4)$$

where k_{EP} is the ENZ plasmon dispersion relation for the interface between semi-infinite film and air layer, k_t is the finite film thickness correction term, and k_r is the additional term coming from the surface roughness. Eq. (4.3) serves as a dispersion relation template for smooth ENZ film covered with a anisotropic surface roughness layer. Now using the dispersion relation, the two basic damping contributions, i.e., internal and radiation damping can be estimated for the Lorentzian description of the absorption curve [106, 116]:

$$A(\lambda)=\frac{4\Gamma_i\Gamma_{rad}}{\left[\left(k_x\right)_\lambda-\left(k_x\right)_{\lambda_{ENZ}}\right]^2+\left(\Gamma_i+\Gamma_{rad}\right)^2} \quad (4.5)$$

with damping terms are defined as,

$$\begin{aligned}
\Gamma_i &= Im\left(k_{EP}+k_t\right)\\
\Gamma_{rad} &= Im\left(k_r\right)
\end{aligned} \quad (4.6)$$

where internal damping, Γ_i accounts for the internal losses occurring in the medium due to the de-excitation heating of the electron-hole pairs driven by the electromagnetic field of the ENZ plasmons, and the surface roughness led attenuation loss of ENZ plasmons [19]. On the other hand, back-coupled radiation loss, coming from the finite thickness of the film layer, manifests as the radiation damping term, Γ_{rad}. At $\lambda=\lambda_{ENZ}$, the first squared term in the denominator of the Eqn. (4.5) vanishes. As evident, the maximum of the absorption, i.e. A = 1, can be obtained for the equal values of the internal and radiation damping. In this context, using the Eqn. (4.5), we have calculated the values of Γ_i and Γ_{rad} are calculated at the numerically evaluated PA point, i.e., at the wavelength 1302 nm and incident angle of 44.32°. These values are around be 2.44×10^{-3} and 2.42×10^{-3}, respectively. Physically, this almost-equaled values of internal and radiation damping means that a complete destructive interference transpires between the antiphase radiation and incoming field amplitude [19]. In the wavelength region where these

TH-2572_156121026

damping terms are equaled, a maximum value of one in the absorption spectra is manifested, and PA is achieved.

4.6 Conclusion

In essence, the effect of the gradually increasing surface roughness on the ENZ plasmon resonance properties of PLD-ITO thin films under high vacuum environment is demonstrated both experimentally and theoretically. Increasing the surface roughness in the vacuum-deposited films resulted in the deepening of the experimentally measured reflectivity spectra and subsequent observation of near-perfect absorption in the sample with the highest surface roughness. Ellipsometric modeling of randomly rough metallic indium-rich ITO thin films containing particulates of random size and shapes is accomplished via DL model and ABEMA. The analysis is also accompanied with the approximation that PEC is applicable to the individual vacuum-deposited particulates. Furthermore, a leap beyond the experimentally plausible realm, with the aid of the numerical tools in hand, demonstrated more profound absorption values for all the samples at some lower angle of incidence. Among the samples investigated, sample S3 showed the signature of PA, with a value of 99.87% (expected to be significantly higher in the actual experiment), just above the ENZ wavelength for the incident angle 44.32°. The strong enhancement of the electric field intensity at the PA wavelength is established as the main reason behind such a high degree of enhancement. Additionally, rigorous scrutiny into the absorption loss density variation led to the conclusion that the surface roughness, as an effective medium layer, plays a crucial role in absorption loss dissipation and serves as subsidiary machinery to the pristine layer in attaining PA. Modification of the ENZ mode dispersion in the presence of a surface roughness layer is also discussed, and observed PA is recognized as the outcome of the crossover between the internal damping and radiation damping terms.

TH-2572_156121026

Chapter 5

Ambient Condition Dependent LMR Response of PLD ITO Thin Films

The last two chapters, i.e., Chapter 3 and Chapter 4 discussed ENZ plasmon resonance in the context of pulsed laser deposited ITO thin films. Interestingly, ITO, being metal oxide, can generate LMR, which is relatively less explored compared to SPR. LMR is a consequence of the resonance excitation of lossy modes inside a thin film waveguide by an evanescent wave. LMR offers some crucial advantages over the most widely used SPR phenomenon, such as the leverage of using both polarizations for excitation, the multiplicity of resonances through careful tuning of the coating thickness, etc. [41]. Noble metals or metal oxide with sufficiently high carrier concentration are used for SPR excitation. In contrast, the requirement of a comparatively large and positive real part of permittivity has forced LMR to be a dielectric-material-only phenomenon [41, 200]. Till now, LMRs have been preferably excited through a fiber optics configuration due to the extreme grazing angle requirement of the excitation [6, 41, 47]. For the thin film based geometry, Del Villar *et al.*, in their pioneering work, demonstrated LMR experimentally in ITO thin films by applying a modified Kretschmann–Raether (K-R) setup [44]. However, after this work, only a handful of experimental studies have been done in thin film configuration [117, 201]. Such a demoralizing trend can be corroborated by two major difficulties associated with this thin film based K-R geometry: very weak LMR signal and low RI sensitivity compared to the fiber optics configuration. The first problem, i.e., low intensity compared to fiber optics, can be solved by taking account an important design rule suggested by Del Villar *et al.* [145]. It states that the increase in the extinction coefficient in material will potentially lead to a deeper resonance response. But the main problem with the dielectric materials used for LMR generation is that they have very low extinction coefficients in the wavelength region of interest. In this context, metals, initially thought to be futile in the case of LMR, could prove to be extremely useful with their interbands positioned at the visible range [202], which results in enhancement of the extinction coefficient. Thus , dielectric thin films encapsulated with right amount of metal could prove

TH-2572_156121026

to be an excellent material candidate for generating a very high degree of LMR response.

This chapter compares the LMR response of pulsed laser deposited ITO thin films at different ambient conditions, namely, O_2, N_2, Ar, He gases, and high vacuum. Unlike the modified setup employed by Del Villar *et al.* requiring an all-side-polished prism, the present used simple K-R geometry to probe the LMR response of these films. All the details about thin film deposition and characterization techniques are listed in Chapter 2. This work could achieve −14.3 dB for transverse electric (TE) and −6.4 dB for transverse magnetic (TM) polarization for vacuum-deposited ITO thin films, while films deposited under various gaseous environment exhibits very low attenuation values. Metallic indium generated interbands was established as the main catalyst behind such a high degree of LMR response in vacuum-deposited ITO thin films. A modified TMM, which takes into account the surface roughness of the films through the application of the ABEMA, is developed to realize the experimental LMR spectra numerically.

5.1 Experimental details and Characterization techniques

ITO thin films were deposited from lab-made 10 wt.% SnO_2 doped In_2O_3 pellet via the PLD technique. For films under a gaseous environment, 0.05 mbar pressure of O_2, N_2, Ar, He gases were used, while the other film was deposited under a high vacuum of pressure ~2×10^{-5} mbar without the use of any ambient gases. Deposition temperature and target-to-substrate distance were kept fixed at 400°C and 3.5 cm, respectively. The deposition time was varied in such a way that the overall thickness remained relatively constant at 70 nm. All the minute details of the PLD procedure are enumerated elaborately in Chapter 1.

Further, two more ITO films with different metallic indium percentages but the same surface roughness value were deposited under a high vacuum environment to consolidate the claim that metallic indium is the main source behind a high degree of LMR response. The target-to-substrate distance for samples designated as A and B was 3.5 cm and 3 cm, respectively. The deposition time was adjusted in such a way that the surface roughness is similar for these two samples. The other deposition parameters remained similar to the ITO thin films deposited under various ambient conditions.

TH-2572_156121026

Film thickness and surface roughness of the samples were evaluated from ellipsometric analysis by employing an optical model consisting of Drude and Lorentzian oscillators. Surface roughness evaluated from SE was confirmed by AFM, which gives the RMS surface roughness value of the PLD-ITO thin films. Surface morphologies of all the films were characterized by FESEM images. The presence of metallic indium sub-phase inside vacuum-deposited ITO thin films was confirmed by XRD, and the percentage of the metallic indium inclusion was calculated by performing Rietveld refinement operation over the XRD data.

LMR spectra over the wavelength range of 400 – 900 nm were recorded using a spectroscopic ellipsometer. A simple K-R configuration, where both incident and reflected light travels through the diagonal faces of the right-angle BK7 glass prism, as shown in Figure 2.10, was applied for this purpose. Note that the present setup is relatively more straightforward than that used in Ref. [44]. In their K-R configuration, the light beam was incident over the lateral faces of a customized all-side-polished prism. Minute details of the simple K-R setup used for LMR spectra of PLD-ITO films are given in section 2.4. In the present work, the incident angle outside the prism was fixed at 89.95° for all measurements. In order to understand whether whole of the elongated light beam, at an extreme grazing angle like 89.95°, interacted with the sample through the prism, it is important to have a look at the experimental procedure involved in LMR measurement at such grazing angles.

The SE system used in this study has an ultra-microspot arrangement, not the normal microspot. The Ultra-microspot spot size is 70 × 70 μm at 75°, while for normal microspot, it is 365 × 470 μm for the same angle. Microspot doublet lens of focal length 40 mm focusses the light beam of diameter 3 mm onto the sample, as shown in Figure 5-1. Therefore, the aperture angle comes out to be ~ 4° with respect to the given beam diameter. As the arc of the lamp is horizontal, the shorter dimension of it will be elongated by the change in angle of incid-

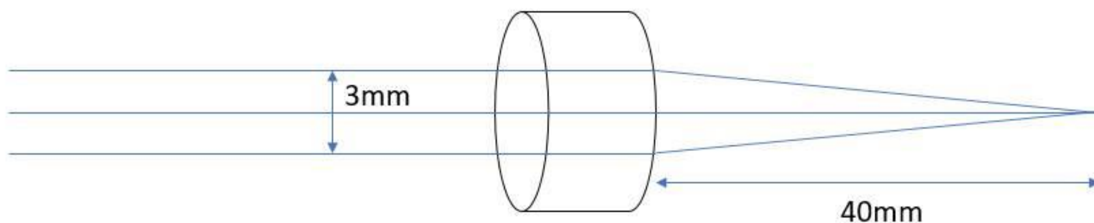

Figure 5-1. Ray diagram of the microspot doublet lens used LMR measurement via ellipsometer.

TH-2572_156121026

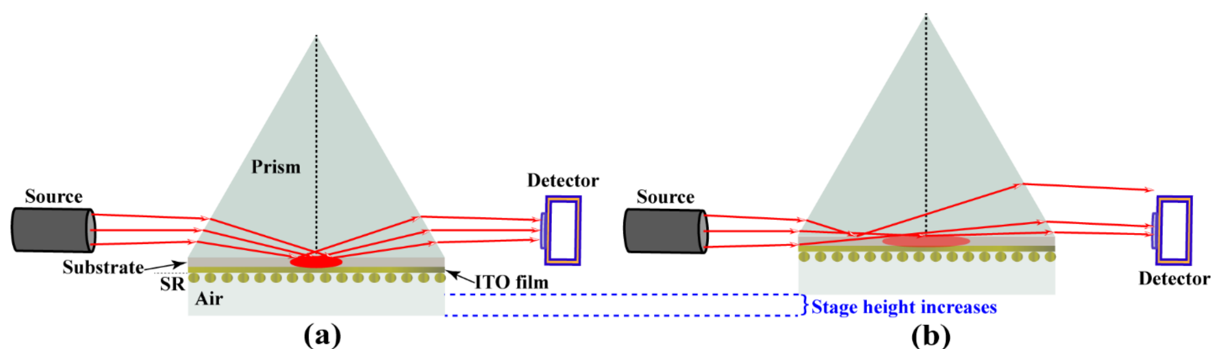

Figure 5-2. An illustration of the interaction of the incident beam with the K-R set-up: (a) at an optimal height; (b) at a slightly different height.

ence. Thus, the light beam diverges significantly from the original 70 × 70 µm size as the light impinges 89.95°. But the substrate dimensions were chosen large enough such that whole of the beam falls onto the sample. It is also to be noted that K-R setup was kept on a height-adjustable stage which has a precision of 0.01 mm. Before each measurement, the height of the stage was adjusted and the intensity on the detector was monitored simultaneously. At a certain height, the intensity maximum is observed. With deviation from the optimal height, a huge intensity drop is observed. Both the situations are picturized as accurately as possible in Figure 5-2. For an optimal case, the incident beam only passes through the refracting surface of the prism and not through the lateral side of the sample. Thus, this setup is clearly different from the one used in the ref. [45] where the beam was incident laterally on the sample.

5.2 Results and Discussions

5.2.1 Structural, morphological and optical properties of PLD-ITO thin films under different ambient

XRD pattern of the PLD-ITO thin films under different ambient gases over the diffraction angle range $10^o \leq 2\theta \leq 70^o$ is as shown in Figure 3-1. At the same time, Rietveld refined XRD pattern of the vacuum-deposited ITO thin film (denoted as S3 in Chapter 4) is shown in Figure 4-1. It is evident that all the films are polycrystalline in nature with preferred orientation along the (222) direction. This is a signature of the pure ITO phase (PDF Card No.: 01-089-4598). Interestingly, ITO film deposited in the vacuum environment shows one extra peak at the 2θ value 32.9°. This additional diffraction peak has been linked to the (101) phase of the metallic indium (PDF Card No.: 01-070-2888), which is found to be omnipresent in the

TH-2572_156121026

case of ITO films deposited under extreme oxygen-reducing conditions [134]. In the present work, a pure ITO (10 wt% SnO_2 doped) pellet was used to deposit ITO films via PLD. Thus, the ITO films deposited under gaseous environments have a pure ITO phase only. In contrast, for the vacuum-deposited ITO film, a phase separation takes place due to the oxygen-deficient conditions inside the PLD chamber and thus metallic indium nanoclusters are formed as a byproduct [134]. In order to extract the exact amount of this metallic indium phase, Rietveld refinement is performed over the XRD data. As shown in Figure 4-1, the XRD pattern of vacuum-deposited ITO film is accurately refined by a double-phase Rietveld refinement operation. From this analysis, the metallic indium percentage inside the vacuum-deposited ITO film is determined to be 8.48%.

FESEM images of the ITO films deposited under different background pressure is shown in Figure 3-2, while that of sample S3 is shown in Figure 4-2. A widely variable surface morphology of the PLD-ITO films with the change in ambient condition is quite apparent from these images. ITO film deposited under vacuum environment are enriched with particulates of different sizes and shapes distributed all over the film surface. Such random structures can be attributed to the two competing mechanisms that take center stage for pulsed laser deposition in a high vacuum environment [146]. Firstly, just after the laser irritation, transient melts come out from the target and these liquid droplets shaped melts solidifies due the exertion of recoil pressure. This process results in random size particulates in plasma plume, which get deposited onto the substrate without facing any severe collisions along the way. Secondly, repeated laser shots over a long time result in the sub-micrometer-sized particulates ejection. As inert gases such as Ar and He is purged into the PLD chamber, though particulates size reduces, but the nanostructured shape remains prevalent. Such an observation is similar to the earlier reports of PLD-ITO films deposited under an inert gas environment [133, 159]. For heavier gases like O_2 and N_2, films are almost particulates free. An increase in collision probabilities between plasma plume constituents with the increasing molecular weights of the gases and, thereby, the gradual reduction of particulates size is responsible for such surface behavior [130].

AFM images of the ITO films deposited under ambient gases is shown in Figure 3-3 and the vacuum-deposited ITO thin film (S3) is shown in Figure 4-3. AFM micrographs of PLD-ITO thin film deposited at different ambient condition exhibit similar surface structures as the one observed in FESEM images. The surface roughness of the ITO films increases

TH-2572_156121026

monotonically from 1 ± 0.4 nm to 58.1 ± 14.4 nm as we go from gaseous ambient (O_2 gas) to high vacuum environment. This trend of surface roughness in gaseous environment can be correlated to the nano-structuring of the ITO thin films under inert gases, while in the case of high vacuum, collision-less particulates of random size and shape are responsible for such high value of surface roughness.

Measured and fitted SE spectra for the real ($\langle \varepsilon_1 \rangle$) and imaginary ($\langle \varepsilon_2 \rangle$) part of pseudo-dielectric permittivity for the ITO samples deposited under different background gases and under high vacuum are as shown in Figure 3-5 and Figure 4-7, respectively. A combination of Drude and multiple Lorentz oscillators was used to model the pristine film layer over the wavelength range 220 – 1700 nm. In addition to this, ABEMA was used to model the surface roughness over-layer. As evident from the FESEM and AFM images, ITO films, especially the vacuum-deposited ones via PLD, are enriched in particulates of various sizes and shapes distributed randomly over the surface. Thus, ABEMA is preferred over the commonly used BEMA for the description of the surface roughness of such films. As can be seen from Figure 3-5 and Figure 4-7, the prescribed optical model is able to fit the experimental data excellently for ITO films deposited in gaseous as well as high vacuum environment.

All the important parameters acquired from the ellipsometry analysis of ITO films deposited gaseous and high vacuum environment are given in Table 3-1 and Table 4-1, respectively. It is evident that the overall film thickness of the ITO films is almost constant at ~ 70 nm for various ambient conditions. Surface roughness of PLD-ITO films increased monotonically from 0.8 nm to 49.7 nm as the deposition condition changed from gaseous to high vacuum ambient. The RMS roughness calculated from the AFM matches quite well with that predicted from the ABEMA model. The gradual increase in Drude plasma energy (E_p) from O_2 to He gas and then to a high vacuum environment can be correlated to the oxygen deficiencies. These oxygen vacancies are responsible for the increment of free electron densities via the injection of two extra free electrons [88]. The zero value of Drude scattering frequency (E_Γ) in the case of vacuum-deposited ITO film comes from the PEC approximation, i.e., applicable to the individual particulates, as discussed in subsection 4.2.3 of Chapter 4. Coming to the Lorentz oscillators, it is to be noted that the oscillators situated at higher energies can be corroborated to band gap absorption of the ITO thin films [203]. The significance of

TH-2572_156121026

these parameters is discussed more elaborately in Chapter 3 and Chapter 4. Importantly, the main takeaway from the ellipsometry analysis is the presence of two extra oscillators at energy values of 1.3 eV and 1.98 eV in the case of vacuum-deposited film. These two oscillators are a clear signature of the interbands related to the metallic indium [189, 190]. The occurrence of these oscillators is in line with the observation of distinct peak related to the metallic indium in XRD analysis.

Variation of the refractive index and extinction coefficient of all the samples over the wavelength range 400 – 900 nm is plotted in Figure 5-3. The variation of refractive index over the wavelength range 400 – 900 nm for different PLD-ITO presented here are in line with previous reports [131, 203-205], where it was reported that increase in plasma energy leads to the decrease in the overall refractive index values. It can be seen that the ITO thin films deposited under a gaseous environment mimic the dielectric-type behavior of the TCOs in the visible range [203-205], i.e., these films have a low extinction coefficient. However, vacuum-deposited ITO film exhibit very high value of extinction coefficient in the wavelength studied here. Basically, metallic indium-related interbands distributed over this wavelength window elevate the extinction coefficient in the vacuum-deposited ITO film.

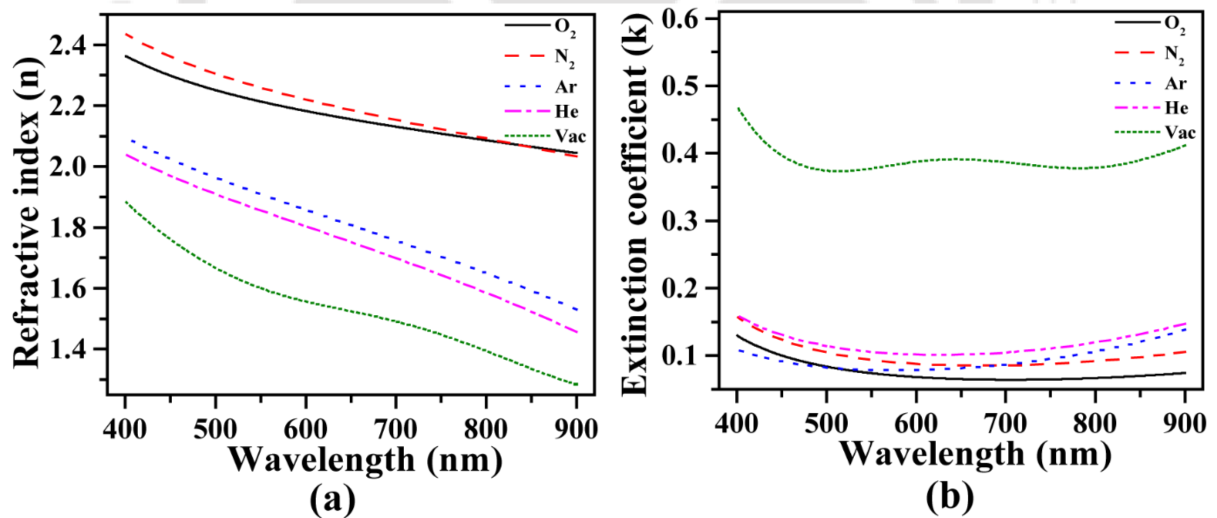

Figure 5-3. Variation of (a) refractive index and (b) extinction coefficient with the incident wavelength for ITO thin films deposited at various ambient condition.

TH-2572_156121026

5.2.2 LMR spectra of PLD-ITO thin films under various ambient conditions

In Figure 5-4, the experimentally obtained LMR response of the vacuum-deposited ITO film is compared to the ITO films deposited under various gaseous environments. The vacuum-deposited film exhibited − 14.3 dB attenuation at the wavelength of 625 nm for TE polarization and − 6.4 dB attenuation at 470 nm for TM polarization. In comparison, ITO film deposited under the He gas ambient, the best performing film among the gaseous ones, showed mere − 1.4 dB attenuation for TE polarization. At the same time, there is no signature of LMR in any of the films deposited under gaseous environments for TM polarization. Such a high degree of LMR signal, i.e., attenuation of − 14.3 dB for TE and − 6.4 dB for TM polarizations, is unprecedented in the case of K-R geometry for which the highest achievable LMR attenuation until now was ≈ − 0.6 dB and ≈ − 0.5 dB for TE and TM polarizations, respectively [44]. These attenuation values observed in vacuum-deposited ITO film are certainly comparable to those obtained from complicated D-shaped fiber geometries [200, 206]. It is quite captivating to note that, using a simple K-R setup, almost 25-fold and 13-fold enhancement is accomplished in LMR signal for TE and TM polarizations, respectively, when compared with the reported values in Ref. [44], for similar film thickness. However, it is acknowledged that their modified prism geometry is highly advantageous for LMR generation due to the possibility of achieving extreme grazing angles. Thereby, the vacuum-deposited ITO thin film is expected to have an

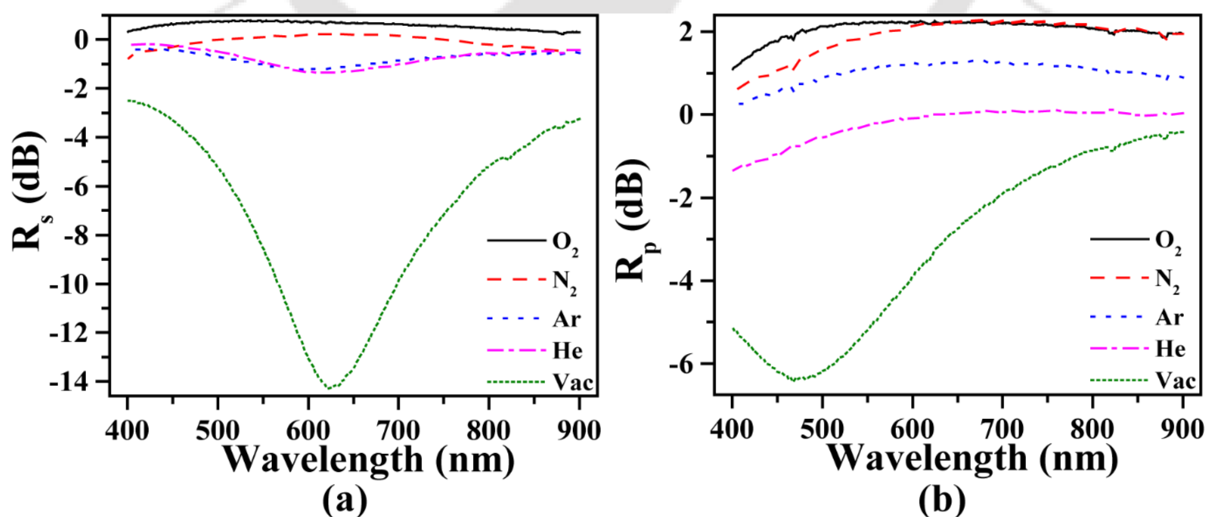

Figure 5-4. Experimental LMR spectra of ITO films deposited at various ambient conditions over the wavelength range 400 – 1700 nm for (a) TE polarization and (b) TM polarization.

TH-2572_156121026

even higher LMR response in such specialized K-R geometry. A very high value of the extinction coefficient compared to the gaseous films, as shown in Figure 5-3. (b), is the main reason behind very high enhancement of the LMR depth in vacuum-deposited ITO film. However, the LMR position does not follow the linear redshifting with an increase in the refractive indices of the films, as predicted earlier [145]. In contrast, the resonance dip position remains relatively unaltered for all three samples showing LMR, though their refractive indices are quite apart from each other. In addition to that, it may seem plausible that the LMR dip position is only dependent on the overall thickness since all the PLD-ITO films have the same thickness. However, this argument also will be refuted in the subsequent sections. Thus, the anomalous behavior of the LMR position not following the variable refractive index or thickness is unexplained at the moment and needs further scrutiny.

5.2.3 Results of the numerical analysis

The numerical analysis was done with the help of a modified TMM method which takes the surface roughness into account with the help of ABEMA. All the details about the theoretical framework of this numerical simulation algorithm and its implementation in MATLAB script were discussed in earlier chapters. The same four-layer system is employed, i.e. prism-film-surface roughness-air by approximating substrate and prism as a single layer. DL parameters for different ambient conditions, which is applied to the film layer applied to the pristine film layer, is taken from Table 3-1 and Table 4-1. The other layers are simulated by following the exact same procedure as discussed in Chapter 4.

Numerically simulated LMR spectra over the wavelength range 400 – 900 nm for all the samples is as shown in Figure 5-5. As can be seen that the proposed numerical model almost accurately reproduces the overall resonance features for both polarizations in case of all the PLD-ITO thin films. However, numerically simulated LMR spectra has significantly larger than depth the experimentally observed one. Here, it is to be noted that while building a framework for the numerical simulation in this case, the broadening of the impinging light beam was neglected, which is paramount in near-parallel incidence [41]. This is the main reason behind the discrepancy in LMR intensities.

TH-2572_156121026

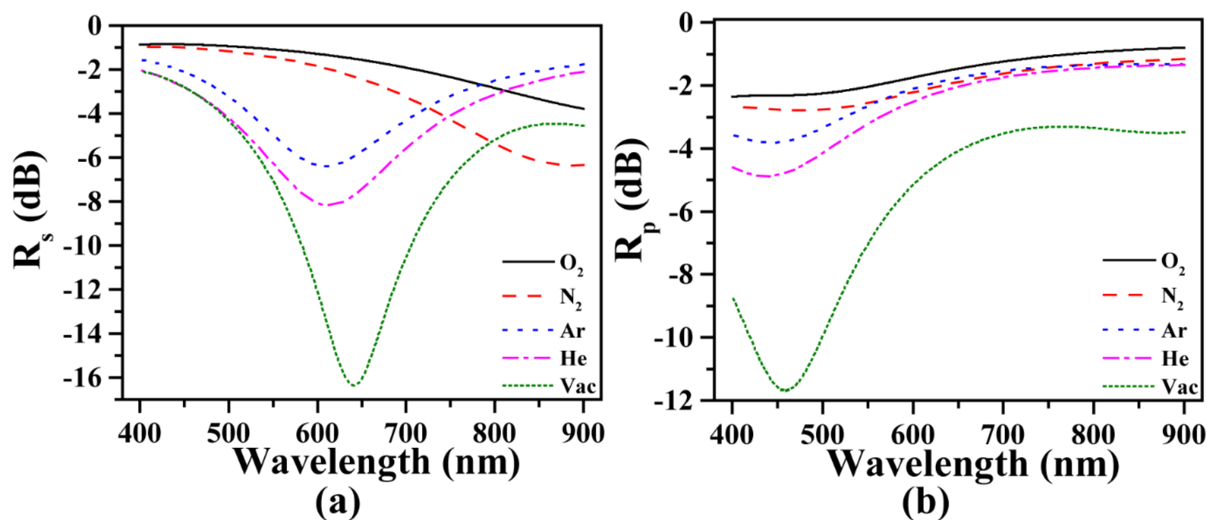

Figure 5-5. Numerically simulated LMR spectra of ITO films deposited at different ambient conditions over the wavelength range 400 – 1700 nm for (a) TE polarization and (b) TM polarization.

5.2.4 Origin of high degree of LMR response in vacuum-deposited ITO films

The surface roughness of the PLD-ITO thin films jumps abruptly to a very high value as we go from the gaseous environment to a complete high vacuum environment, as is evident from AFM images and SE analysis. Interestingly, experimental as well as theoretical LMR intensity follows the exact same trend. Thus, there is a strong possibility that these two properties are correlated in some way. In this regard, to concretely establish indium metal as the main deciding factor for anomalously enhanced LMR intensity in comparison to the surface roughness, two ITO films were deposited as sample A and B with the same surface roughness but different metallic indium inclusion and measured their LMR spectra at an incidence angle 89.95°.

Rietveld refined XRD pattern for sample A and sample B is as shown in Figure 5-6. As expected, being vacuum-deposited ITO films, samples A and B exhibits the coexistence of pure ITO phase and metallic indium sub-phase. However, the relative intensity of (101) peak is increased significantly from sample A to sample B. Metallic indium inclusion in sample A comes out to be 3.11%, while in sample B, it is 8.03%. It is to be kept in mind that the target-to-substrate distance for samples A and B is 3 cm and 3.5 cm, respectively, as described in the experimental section of the current chapter. Thus, the higher percentage of metallic indium in sample B can be understood because the probability of indium traversing a shorter distance and getting deposited onto the substrate is much higher than larger target-to-substrate distance.

TH-2572_156121026

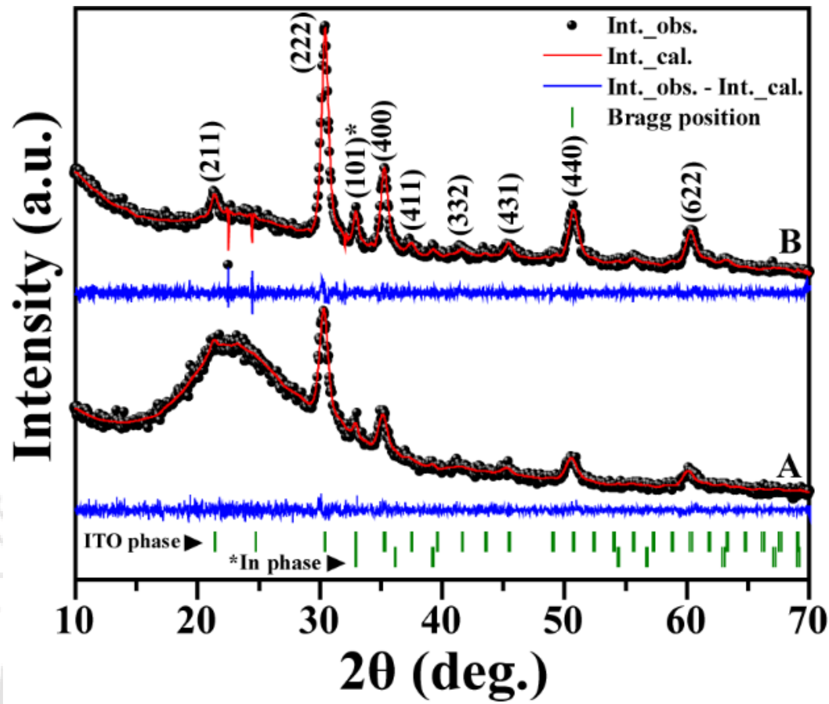

Figure 5-6. Rietveld refined XRD pattern of the samples A and B in the range of 2θ values from 10° to 70°.

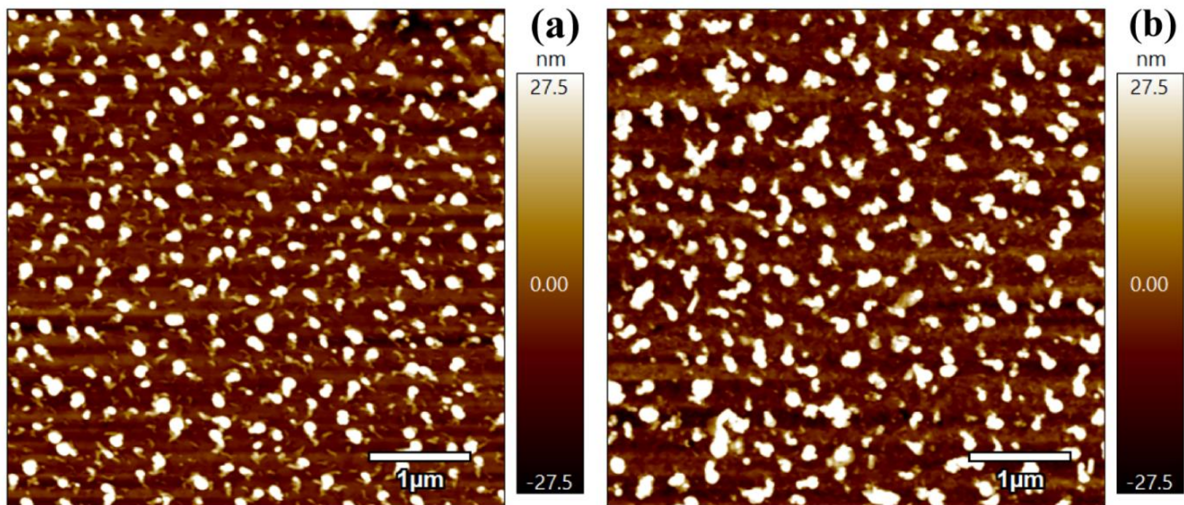

Figure 5-7. 2D AFM micrographs of the samples (a) A (In: 3.11%) and (b) B (In: 8.03%) taken over the surface area of 5×5 μm.

AFM images of these two samples are shown in Figure 5-7. RMS surface roughness value of sample A and B comes out to be 17.7 nm and 17.6 nm, respectively. Thus, samples A and B

TH-2572_156121026

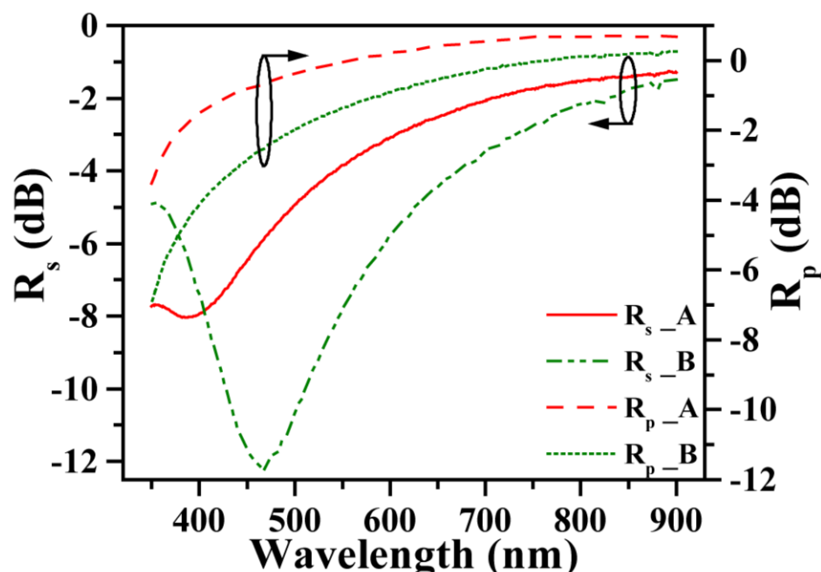

Figure 5-8. Experimental LMR spectra for samples A (In: 3.11%) and B (In: 8.03%) for TE (solid line) and TM (dotted line) polarization.

have different metallic indium inclusion percentages but the same overall thickness (only surface roughness in this case).

Experimentally measured LMR spectra for samples A and B over the wavelength range of 350 – 900 are shown in Figure 5-8. Though there is no signature of LMR for TM polarization in either of these samples, both the sample shows distinct LMR dips in the case of TE polarization. Sample B with a higher metallic indium percentage exhibited much deeper LMR for TE polarization than sample A having lower indium content. Thus, it is evident that just by tuning the indium percentage in ITO films, one can effectively control the LMR depth. Another important thing to note is that samples A and B have their LMR position quite separated from each other even though both of these samples have the same overall thickness, i.e., surface roughness in this case. Thus, the LMR position in this case does not exactly follow either the film thickness or the refractive index, which is distinctly different from the earlier reports [51, 145] and needs more attention.

5.3 Conclusion

To conclude, a novel idea of utilizing dielectric material mixed with a small dosage of metallic inclusion for efficient LMR generation is given in this chapter. In this context, PLD-ITO thin film under a high vacuum environment has been used as a coating material in a simple

TH-2572_156121026

K-R geometry based setup to demonstrate LMR attenuations as high as −14.3 dB for TE polarization and −6.4 dB for TM polarization. LMR response in vacuum-deposited ITO thin film at par with fiber optics geometry was archived without the using specialized prism geometry. LMR spectra of vacuum-deposited ITO thin film is compared to the films deposited at the gaseous environment to firmly establish the superiority of the former. The presence of metallic indium with strong interbands situated at the visible range is established as the main deciding factor for such a high degree of LMR signal enhancement. The experimental LMR spectra is described numerically with a reasonable level of accuracy by employing an effective simulation algorithm based on modified TMM. The novelty of this work lies in the fact that the LMR signal could be tuned by changing the metal inclusion percentage in a single-step process rather than doping metal separately in a dielectric medium.

Indian Institute of Technology Guwahati

TH-2572_156121026

TH-2572_156121026

Chapter 6

Thickness Dependency of LMR Response in Vacuum-deposited ITO Thin Films and Exploration of Refractive Index Sensing as an Application

Previous chapter established vacuum-deposited ITO thin films as one of the most effective material platform for LMR studies. Using vacuum-deposited ITO thin films, attenuation values that are unprecedented in the literature so far was achieved. In this chapter this novel study on vacuum-deposited metallic indium-rich ITO thin films is further extended by exploring the thickness dependency and refractive index sensing capabilities of these films.

As discussed in Chapter 1, film thickness plays a pretty vital part in determining the cutoff condition for LMR excitation corresponding to a particular waveguide mode. In the case of fiber optics, which is the most-studied geometry so far in the literature for LMR excitation, the effect of film thickness has been explored both numerically and experimentally in several reports [41, 51, 145, 207]. In stark contrast, there is no report, neither numerical nor experimental in nature, on film thickness dependency of thin based K-R geometry. The extremely low intensity of LMR intensity in thin film geometry is the reason behind this scarcity. However, metallic indium-rich ITO films deposited via PLD solve this intensity problem emphatically. It would be quite interesting to study the film thickness dependency of these vacuum-deposited ITO thin films with the help of experimental and numerical means. In this chapter, ITO thin films were deposited using PLD under a high vacuum environment for different deposition times. LMR spectra were recorded at several incidence angles via K-R geometry. A numerical simulation algorithm based on the modified TMM (modified with the application of ABEMA) is utilized to simulate the experimental LMR spectra for all the vacuum-deposited ITO thin films.

TH-2572_156121026

For a fixed film thickness value, the surrounding medium refractive index (SMRI) dictates the position of the LMR. Therefore, monitoring the LMR position for different SMRI values will give a measure of the RI sensitivity of the device. Though there are several reports available on fiber optics based refractive index sensors [47, 208], there are only one or two significant reports on refractive index sensing using K-R geometry. Torres *et al.* first demonstrated LMR-based ITO thin film refractometer experimentally by employing modified K-R geometry and achieved the highest refractive index sensing values of 700 nm/RIU and 1200 nm/RIU for transverse electric (TE) and TM polarizations, respectively [117]. More recently, Saini *et al.* applied prism/lithium fluoride (LiF)/zinc oxide structures to reach maximum sensitivities up to 61.92°/RIU for TE-polarization and 68.80°/RIU in angular interrogation mode [201]. But, these values lag pretty far behind the best possible optical fiber sensors based on LMR [209]. In this chapter, the refractive index sensing capabilities of metallic indium-rich ITO thin films have been tested and a highly sensitive refractometer is demonstrated for this novel material platform.

6.1 Experimental Details and Characterization Techniques

10 wt% ITO pellets were used to deposit ITO thin films via a PLD system. Target to substrate distance and substrate temperature was kept fixed at 3.5 cm and 400°C, respectively. PLD chamber was evacuated to a base pressure of ~ 2×10^{-5}, and this pressure was maintained throughout the deposition process for all the films. Detailed procedure of pellet preparation, substrate cleaning, and thin film deposition procedure is discussed in great detail throughout Chapter 2. Four sets of samples were deposited for different deposition times, and their nomenclatures were according to the deposition times: 20 min (S1), 40 min (S2), 80 min (S3), and 120 min (S4).

SE was employed for the optical characterization of these randomly rough vacuum-deposited ITO films. Important parameters like film thickness, refractive index, and extinction coefficient were estimated by analyzing ellipsometry spectra over the wavelength range 220 – 1700 nm with the help of an optical model consisting of Drude and multiple Lorentz oscillators. Particulates of random size and shapes over the film surface are modeled as surface roughness by applying ABEMA. More details about the ellipsometry fitting procedure, along with the equation and other factors of ABEMA formulation, can be found in Chapter 2. Surface

TH-2572_156121026

morphology and topology of the vacuum-deposited ITO thin films were analyzed by inspecting FESEM and AFM images, respectively. Rietveld refinement operation was performed over the XRD data to get an idea about different crystallographic phases present in the vacuum-deposited ITO films.

LMR spectra of vacuum-deposited ITO thin films over the wavelength range 350 – 900 nm have been recorded by conventional K-R geometry. The K-R setup was employed in SE in SE instrument which is capable of recording reflection data for both TE and TM polarization. For measuring the angular dispersion of the LMR spectra, the incidence angle was varied from 80° to 89.95° at a step of 1° (0.95° for the last step). The details of K-R geometry utilized for LMR measurement are given in-depth in Chapter 2. Refractive index sensing measurement was done by employing a K-R setup, as shown in Figure 6-1, modified to accommodate the sensing apparatus. An acrylic sheet of height 3 mm is cut into a squared piece of size 15×15 mm. Next, a circular hole of diameter 10 mm and depth 1.4 mm is drilled in the middle of this squared piece with the help of a mechanical pillar drilling machine. Glycerol (Alfa Aesar, ultrapure, HPLC Grade) is mixed with water (Alfa Aesar, ultrapure, HPLC Grade) in appropriate volume percentages to obtain solutions of varying refractive index values. The refractive index value of these solutions was determined using a digital refractometer (*HANNA* instruments - HI96800). All together 6 solution sets were made with increasing glycerol

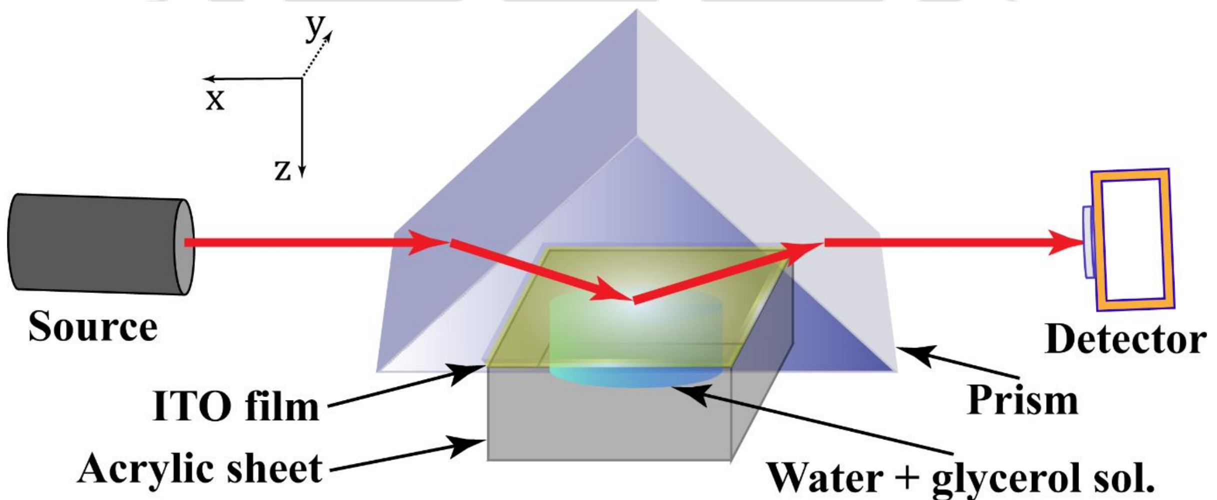

Figure 6-1. 3D representation of the K-R geometry based set up for refractive index sensitivity measurement. A right-handed coordinate system is placed at the left hand side to describe the direction propagation with respect to the sample plane.

TH-2572_156121026

percentage in water: 0% (RI = 1.3325), 20% (1.3622), 40% (1.3914), 60% (1.4165), 70% (1.4315), and 80% (1.4459). These solutions were placed onto the circular hole of the acrylic sheet with the help of a variable volume pipette (Model: *ACCUPIPETTE - T200*; Make: *Tarsons*). As little as 110 μL solution is needed for effective measurement of refractive index variation. Now, the K-R setup is placed over the solution-filled acrylic sheet, and both TE- and TM-polarized light is sent through the prism at an angle of 89.95°. Both CCD and OMA NIR detectors were used in tandem to cover a wavelength of 400 – 1700 nm.

6.2 Details of the Numerical analysis

LMR spectra of vacuum-deposited ITO thin films were numerically simulated by developing a MATLAB script based upon the modified TMM method. In this modified simulation algorithm, a commonly used TMM method is modified to include the surface roughness of the samples with the application of ABEMA. All theoretical aspects of the modified TMM are presented in great detail in Chapter 2. Herea five-layer system is proposed, as shown in the inset of Figure 2-10. The first two layers, i.e., prism and substrate, are approximated to be one single layer of semi-infinitesimal thickness extended in the negative z-direction and subsequently modeled with *nk*-file of BK-7 glass. DL model (parameters given in Table 4-1 and Table 6-1) is applied to reconstruct the dispersion behavior of the vacuum-deposited ITO thin film layer. Partial dielectric constants of the surface roughness layer on top of the films are retrieved by solving the Eqn. (2.12), and the same values were used for modeling the layer. The Air layer was also taken semi-infinite as the first, and its dielectric constant was taken as unity.

6.3 Results and Discussions

6.3.1 Structural, morphological and optical properties of PLD-ITO thin films under different ambient

As described in earlier chapters, PLD-ITO thin films deposited under a vacuum environment are highly rough and are enriched in randomly shaped particulates. FESEM and AFM images of sample S1 to S3 is shown in Figure 4-2 and Figure 4-3, respectively. Figure 6-2 shows the combined FESEM and AFM images of sample S4. These morphological images

TH-2572_156121026

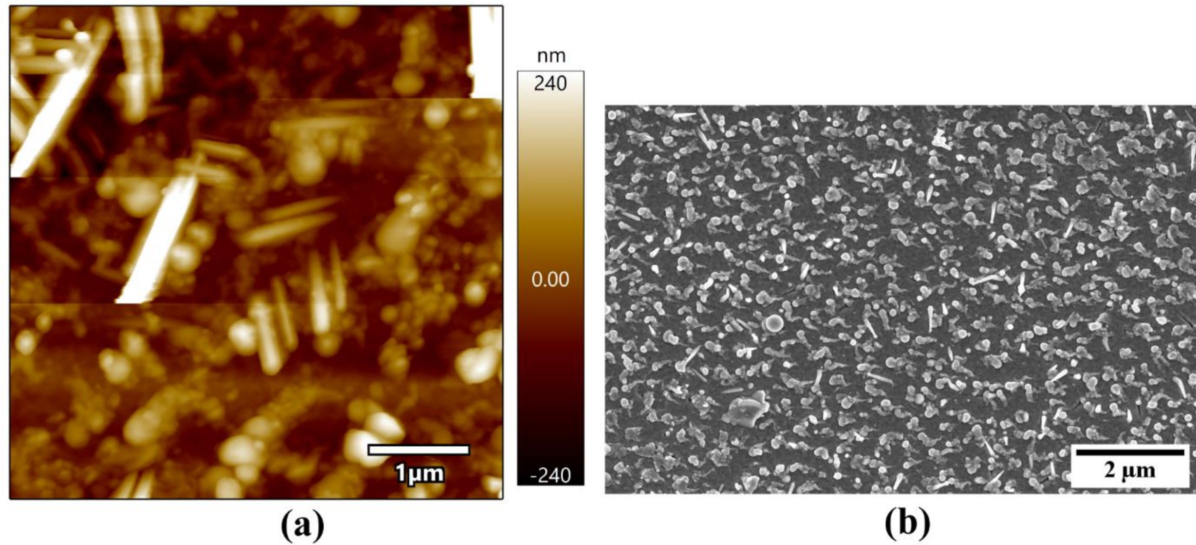

Figure 6-2. (a) AFM and (b) FESEM images of PLD-ITO thin film under vacuum environment for different deposition time of 120 min (S4).

establish the structural complexities associated with the vacuum-deposited ITO films. While the overall spherical nature exists among the films deposited for lower deposition time (S1 and S2), films deposited for higher deposition time (S3 and S4) are enriched in randomly sized and shaped particulates which are distributed all over the film surface. Spherical particulates in the first case are a consequence of the solidification of the liquid ejecta coming out from the target after laser ablation [130]. In the second case, i.e., for the formation of randomly shaped particulates at higher deposition times, the film growth is governed by two fundamental processes: deposition from solidified liquid ejecta and irregularly shaped particulates generated via repeated laser ablation over longer times [146]. The higher substrate temperature also influences the surface features, which are responsible for coalescing and surface diffusion. The surface roughness of the vacuum-deposited ITO films, as determined by AFM, is given by 17.6 ± 3.2 (S1), 29.7 ± 6.2 (S2), 58.1 ± 14.4 nm (S3), and 97.6 ± 29.0 nm (S4).

Information about different crystallographic phases present in the vacuum-deposited ITO films was retrieved by analyzing the XRD spectra. Rietveld refined XRD for same S1 to S3 is shown in Figure 4-1, while that of sample S4 is shown Figure 6-3. The Cubic bixbyite structure of the ITO phase (PDF Card No.: 01-089-4598) remains as the main crystallographic phase. However, an additional phase of pure metallic indium (designated by the (101) peak at the 2θ value of 32.9°; PDF Card No.: 01-070-2888) can be clearly observed in all the films. In

TH-2572_156121026

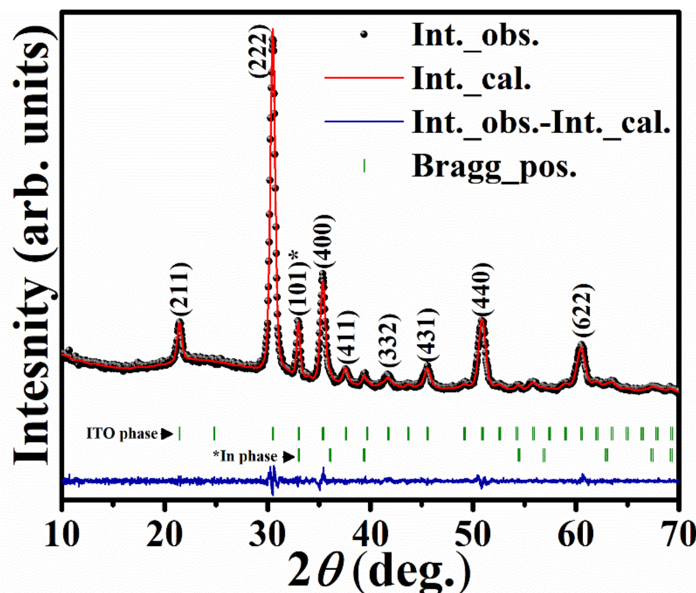

Figure 6-3. Rietveld refined XRD pattern of sample S4.

vacuum-deposited ITO films, phase separation occurs due to the oxygen-deficient conditions inside the PLD chamber. Thus metallic indium nanoclusters are formed as a byproduct [134, 135]. A Rietveld refinement operation was carried out over the XRD data to quantify this metallic indium percentage in the vacuum-deposited ITO films. Metallic indium percentage in the samples comes out to be S1: 3.11% ± 1.89%., S2: 4.58% ± 0.38%., S3: 8.48% ± 0.29%., and S4: 7.72% ± 0.63%.

Variation of the measured and fitted ellipsometry data for sample S1 to S3 over the wavelength range of 220 – 1700 nm is depicted in Figure 4-7. Figure 6-4 shows the variation measured fitted pseudo-dielectric permittivity for sample S4. It is evident that the proposed optical model based on film + surface roughness layer fits the experimental data for all the samples quite excellently. All the parameters obtained from SE fitting by following the film + surface roughness (ABEMA) optical model for sample S1 to S3 are listed in Table 4-1 and the same for sample S4 is listed at Table 6-1. As expected, the overall thickness of the films increases monotonically with the deposition time. The surface roughness values determined from ABEMA matches quite well with those obtained from AFM measurement. In addition to this, there is no presence of a uniform film layer for samples S1 and S2, i.e., the films deposited at lower deposition times. With increasing the deposition time, bigger particulates coalesced with each other to form a uniform film layer underneath. Meanwhile, coalescing of smaller-

TH-2572_156121026

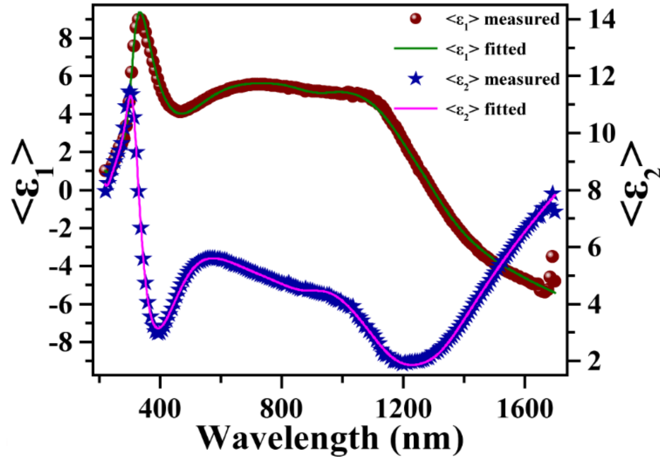

Figure 6-4. Variation of the measured and fitted spectra of the real ($\langle \varepsilon_1 \rangle$) and imaginary ($\langle \varepsilon_2 \rangle$) part of pseudo-dielectric permittivity over the wavelength range of 220 – 1700 nm for the sample S4.

sized particulates form relatively bigger-sized particulates over the film surface, as depicted in morphological images of samples S3 and S4. The film growth process of metallic indium-rich ITO with increasing deposition time is almost analogous to metal film growth in a vacuum environment via PLD. In fact, the metallic indium melts (melting point: 156.6 °C), which inherently forms due to the considerably high substrate temperature, i.e., 400 °C, is partly responsible for the arbitrary shape of the particulates in such films. To effectively describe the ellipsometry data of these randomly rough ITO films using simple Jones matrix-based formalism, PEC approximation was applied to the individual particulates through the application of ABEMA. In this regard, the value Drude scattering frequency (E_Γ), which is connected to the conductivity (σ) through the relation: $\sigma = \frac{\varepsilon_0 E_P^2}{E_\Gamma \hbar}$, is fixed at 0 eV. More insights about the fitting procedure involved in describing the ellipsometry data of these vacuum-deposited ITO films can be found in Chapter 4. Variable depolarization coefficients (L_z) for different films is a concrete testimonial of the fact that surface constituents of such films are deviated from the spherical nature ($L_z = 0.333$). Now, the Lorentzian oscillators used for ellipsometry fitting can be broadly categorized into two subsets: i) oscillators positioned at the UV range, i.e., for energy values greater than 4 eV, represents the bandgap absorption edge of the dominant ITO phase [203], and ii) Additional oscillators at energy values below than 2.25 eV can be corroborated to the metallic indium related interbands [189, 190].

TH-2572_156121026

Table 6-1. The list of parameters acquired from SE data fitting of sample S4. In the table, four Lorentz oscillators are designated by 1st, 2nd, 3rd, and 4th. Oscillator strength (f), central position (E_0), and width (Γ) is given for each oscillators. Uncertainties associated with different parameters are also reported. Note that, SR stands for surface roughness.

Name	Film thick. (nm)	SR (nm)	ABEMA parameters		Drude model		Lorentz oscillators												RMSE
							1st			2nd			3rd			4th			
			Depol. coefficient (L_z)	Void %	E_p (eV)	E_Γ (eV)	f	E_0 (eV)	Γ (eV)	f	E_0 (eV)	Γ (eV)	f	E_0 (eV)	Γ (eV)	f	E_0 (eV)	Γ (eV)	
S4	32.4	84.6	0.432 ± 0.004	33	1.73 ± 0.01	0	2.45 ± 0.02	5.52 ± 0.03	4.79 ± 0.06	0.54 ± 0.01	4.06	0.85 ± 0.02	0.09	1.30	0.32 ± 0.01	×	×	×	0.116

TH-2572_156121026

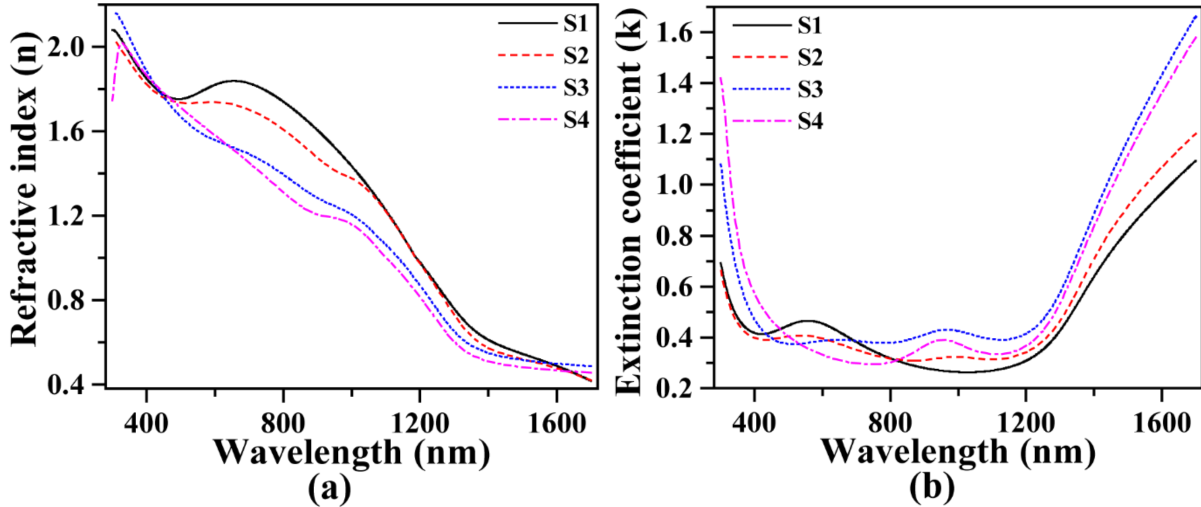

Figure 6-5. Variation of the refractive index (n) and extinction coefficient (k) over the 300 – 1700 nm wavelength range for the vacuum deposited ITO samples.

Variation of the refractive index (*n*) and extinction coefficient (*k*) over the wavelength range of 300 – 1700 nm for the metallic indium-rich ITO films are depicted in Figure 6-5. The variation is quite similar to that observed in the case of pure ITO films, except in the visible and lower NIR wavelengths (up to 1200 nm) [203]. The presence of interbands of metallic indium in this region results in strong absorption peaks in the extinction coefficient. The spectral position of these peaks is in line with the central energies of the Lorentzian oscillators, as reported in Table 4-1 and Table 6-1. The average extinction coefficient value over the visible range for metallic indium-rich ITO films is at least 3-4 times greater than the pure ITO thin films, as shown in Figure 5-3 of Chapter 5. This high value of extinction coefficient is highly beneficial for deeper LMR generation [145].

6.3.2 Experimentally measured LMR spectra of vacuum-deposited ITO thin films

Figure 6-6 and Figure 6-7 presents the experimentally measured LMR spectra for the metallic indium-rich ITO thin films for both TE and TM, respectively, over the wavelength range of 350 – 900 nm. Reflection data were collected for several incidence angles ranging from 80° to 89.95°. To the best of our knowledge, this is the first time angular dispersion of LMR is reported experimentally in the context of thin film based K-R geometry. The depth of the LMR for all the films increases with the increasing incident angle and reaches its maximum

TH-2572_156121026

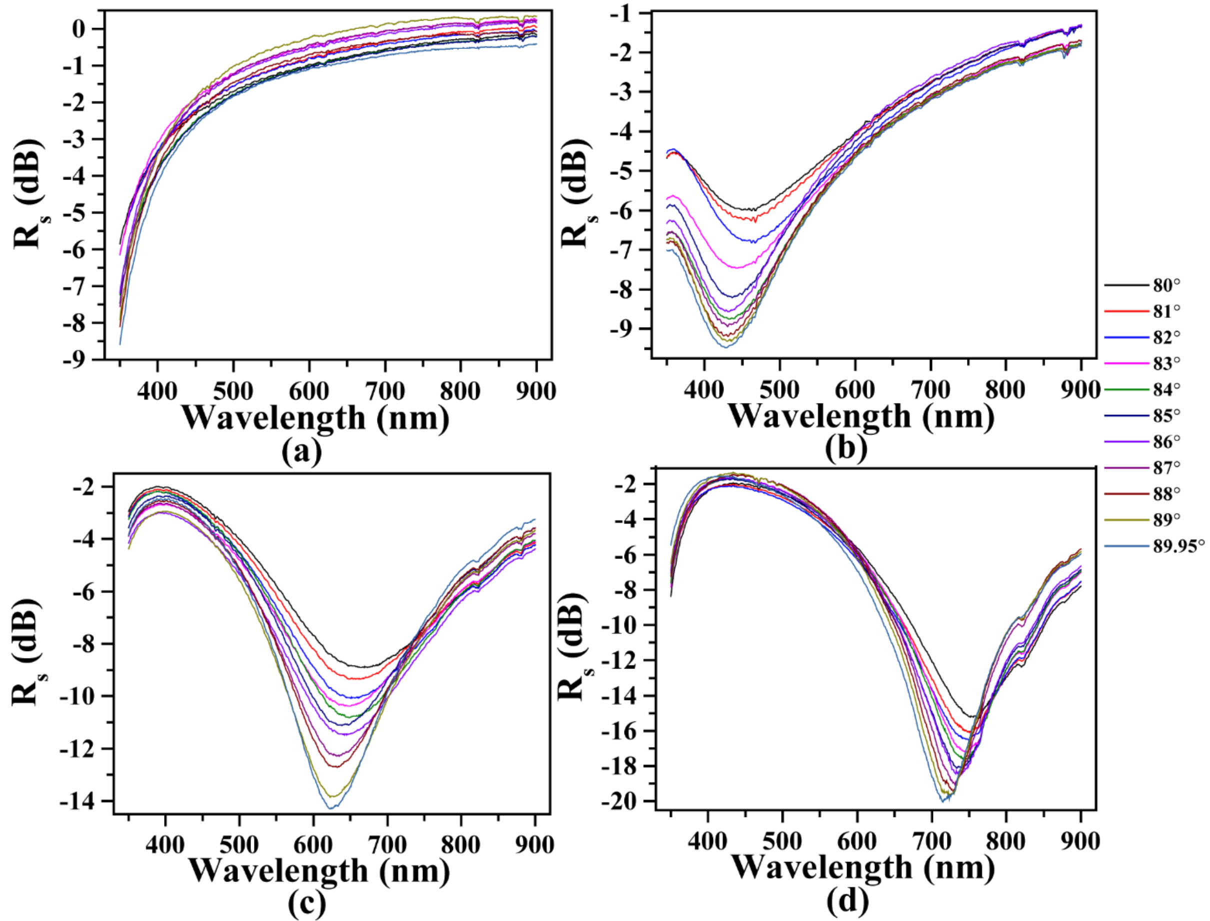

Figure 6-6. Angular distribution of experimentally measured LMR spectra for TE polarization of ITO thin films deposited under vacuum environment at different deposition times: (a) S1 (20 min), (b) S2 (40 min), (c) S3 (80 min), (d) S4 (120 min). The color code used for the incident angles ranging from 80° to 89.95° is pasted at the right-hand side of the figure.

of 89.95°, i.e., the highest possible incident angle. This observation is in accordance with the fact that grazing angle incidence is required for complete excitation of LMR [41]. As we increased the incident angle, a slight blue shift was observed in the LMR dip position. This type of angular dispersion behavior is exactly similar to that observed in the case of SPR phenomena in ITO thin films [95].

A comparison between the experimentally obtained LMR spectra at the incident angle of 89.95° for the vacuum-deposited ITO films with different overall thicknesses is shown in Figure 6-8. Sample S1 does not show any signs of LMR either for TE or TM polarization. But for the other three samples, the depth of the LMR increases significantly with the increasing film thickness for both TE and TM polarization. LMR attenuation as high as – 20 dB (99% in

TH-2572_156121026

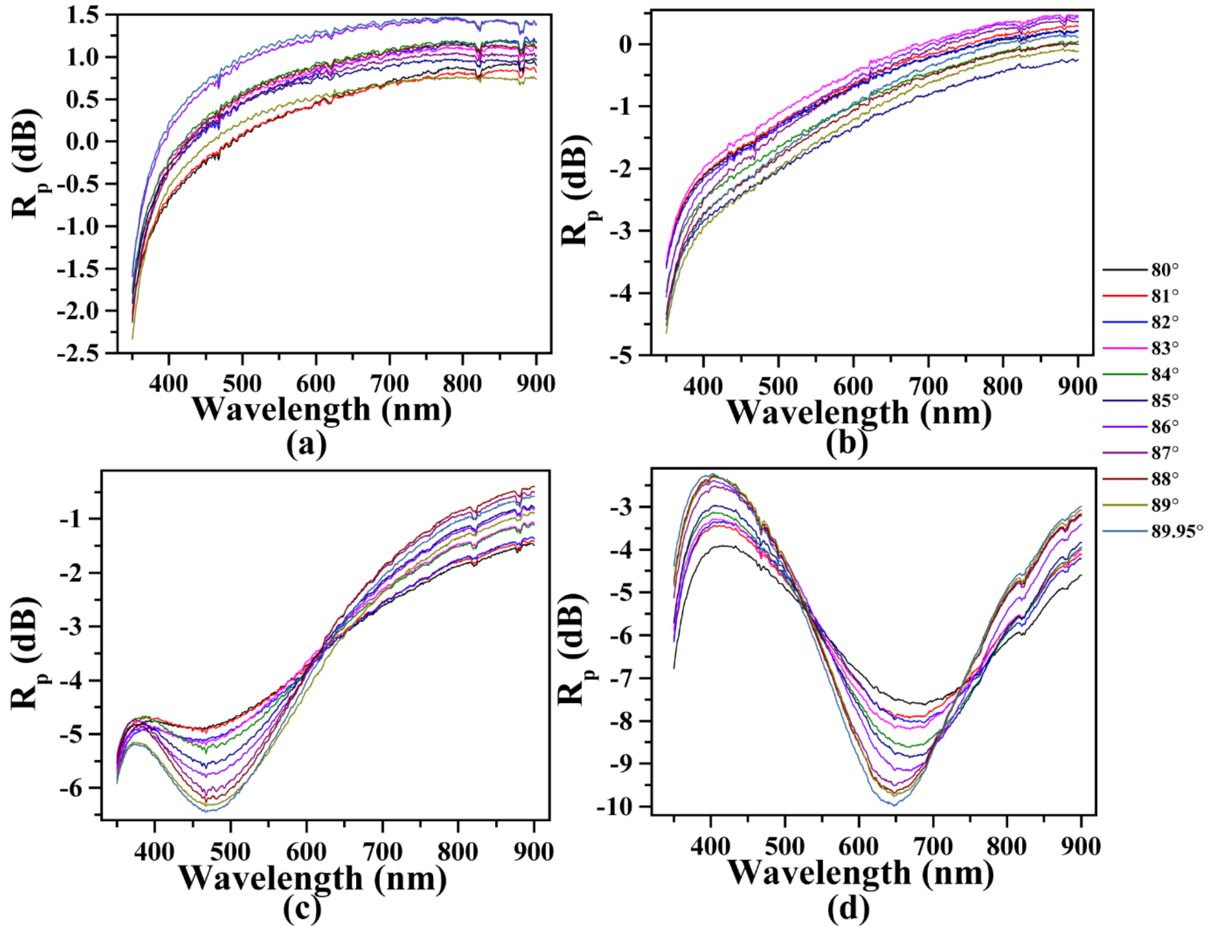

Figure 6-7. Angular distribution of experimentally measured LMR spectra for TM polarization of ITO thin films deposited under vacuum environment at different deposition times: (a) S1 (20 min), (b) S2 (40 min), (c) S3 (80 min), (d) S4 (120 min). The color code used for the incident angles ranging from 80° to 89.95° is pasted at the right-hand side of the figure.

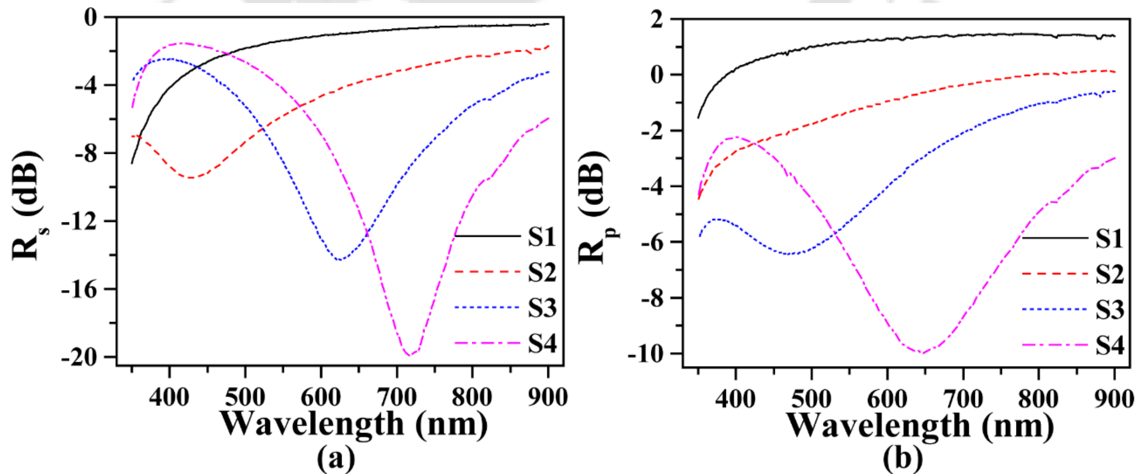

Figure 6-8. Comparison of experimentally measured LMR spectra for (a) TE and (b) TM polarization at the incident angle of 89.95° for different thickness of vacuum-deposited ITO thin films.

TH-2572_156121026

terms of absorption intensity) for TE polarization and -10 dB (90% in terms of absorption intensity) for TM polarization is achieved in the case of sample S4 with the highest overall film thickness. These are certainly the highest reported LMR attenuation values so far, as for the excitation in a thin film configuration is concerned. Metallic indium-related interbands, which resulted in very high extinction coefficient values in the visible region as shown in Figure 6-5. (b), are mainly responsible for this extremely high degree of LMR response in these vacuum-deposited ITO thin films. In addition to this, overall film thickness also plays a vital role in LMR attenuation by providing more lateral volume for the waveguide mode to be guided efficiently [39]. Thus, the substantial enhancement of LMR intensity from sample S1 to S3 can be correlated to the increase in metallic indium percentage and overall thickness. However, sample S4 having a greater overall thickness demonstrates much higher LMR attenuation than sample S3 in spite of the fact that the metallic indium percentage, and thereby, the extinction coefficient (see Figure 6-5. (b)) is slightly lower than the former. Considerably higher overall thickness compensates for a slightly lower extinct coefficient, and thus, producing a very high degree of LMR. Additionally, there is no signature of any other LMR peaks in the measured wavelength region for sample S4. Thus, we can say that the overall thickness of sample S4 is large enough to generate attenuation maxima for the first order of LMR, but it is less than the cutoff thickness of the second-order LMR.

Furthermore, the LMR dip position shifts drastically to higher wavelengths for both TE and TM polarization from samples S2 to S4. LMR position is generally influenced by coating thickness and refractive index (n) for a fixed SMRI value [145]. But, for metallic indium-rich ITO films with comparatively higher extinction coefficient values, it was demonstrated in Chapter 5 that LMR wavelength is insensitive to the coating refractive index (n). Thus, the increasing overall thickness can only explain this substantial red-shift for these vacuum-deposited ITO films.

6.3.3 Numerically simulated LMR spectra of vacuum-deposited ITO thin films

Numerically simulated LMR spectra of the vacuum-deposited ITO films for both TE and TM polarizations at various incident angles ranging from 80° to 89.95° are as shown in

TH-2572_156121026

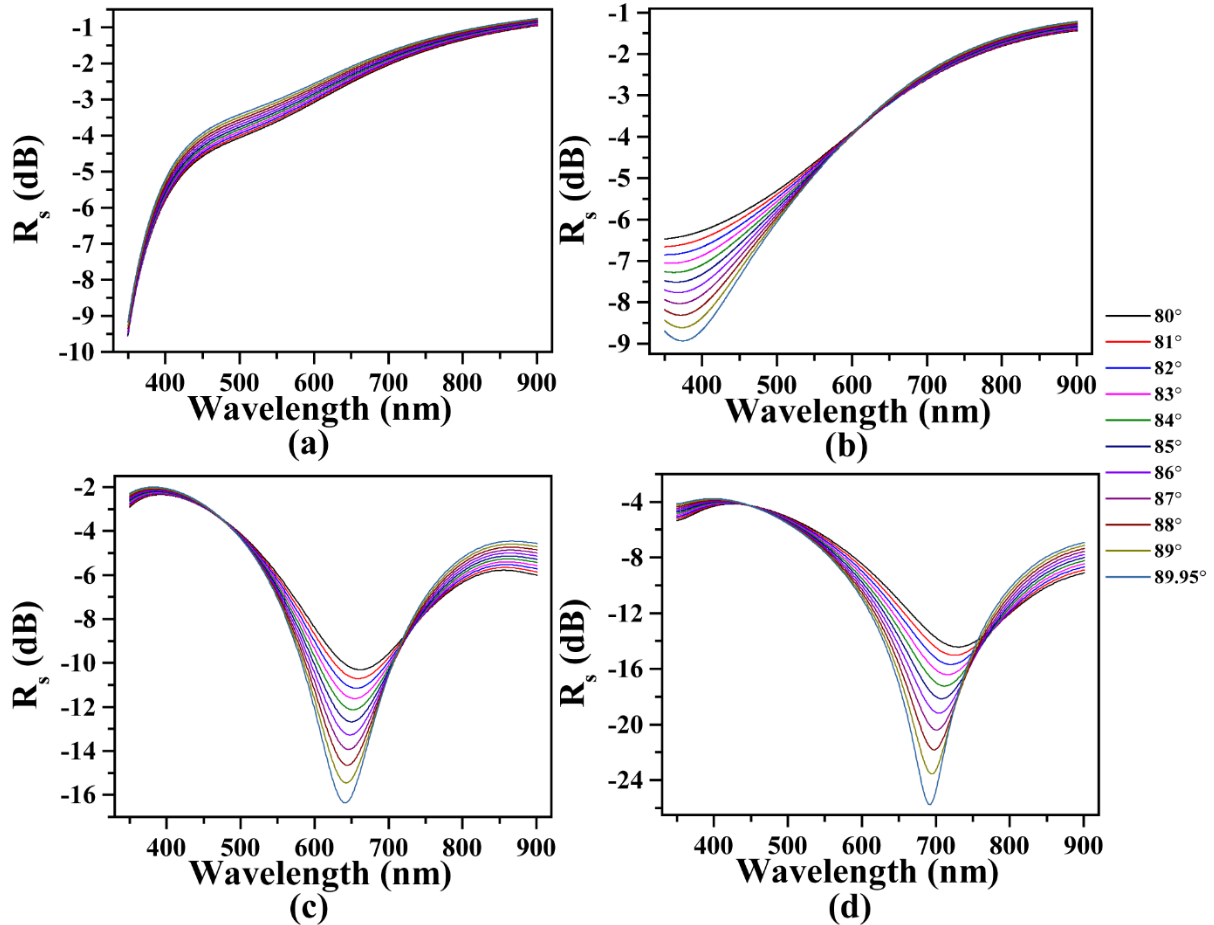

Figure 6-9. Angular distribution of experimentally measured LMR spectra for TE polarization of ITO thin films deposited under vacuum environment at different deposition times: (a) S1 (20 min), (b) S2 (40 min), (c) S3 (80 min), (d) S4 (120 min). The color code used for the incident angles ranging from 80° to 89.95° is given on the right-hand side of the figure.

Figure 6-9 and Figure 6-10, respectively. It is observed that the numerically simulated spectra match quite well with experimentally measured LMR spectra in terms of spectral position and overall resonance features. This further validates the inherent approximations (ABEMA and PEC approximations) involved in the ellipsometric fitting procedure of these randomly rough ITO thin films. The slight difference in intensities of the experimental and numerical LMR spectra can be explained by the broadening of the incident beam at these grazing angles [44], which was not accounted for in the numerical simulation algorithm formulated in this present thesis work.

TH-2572_156121026

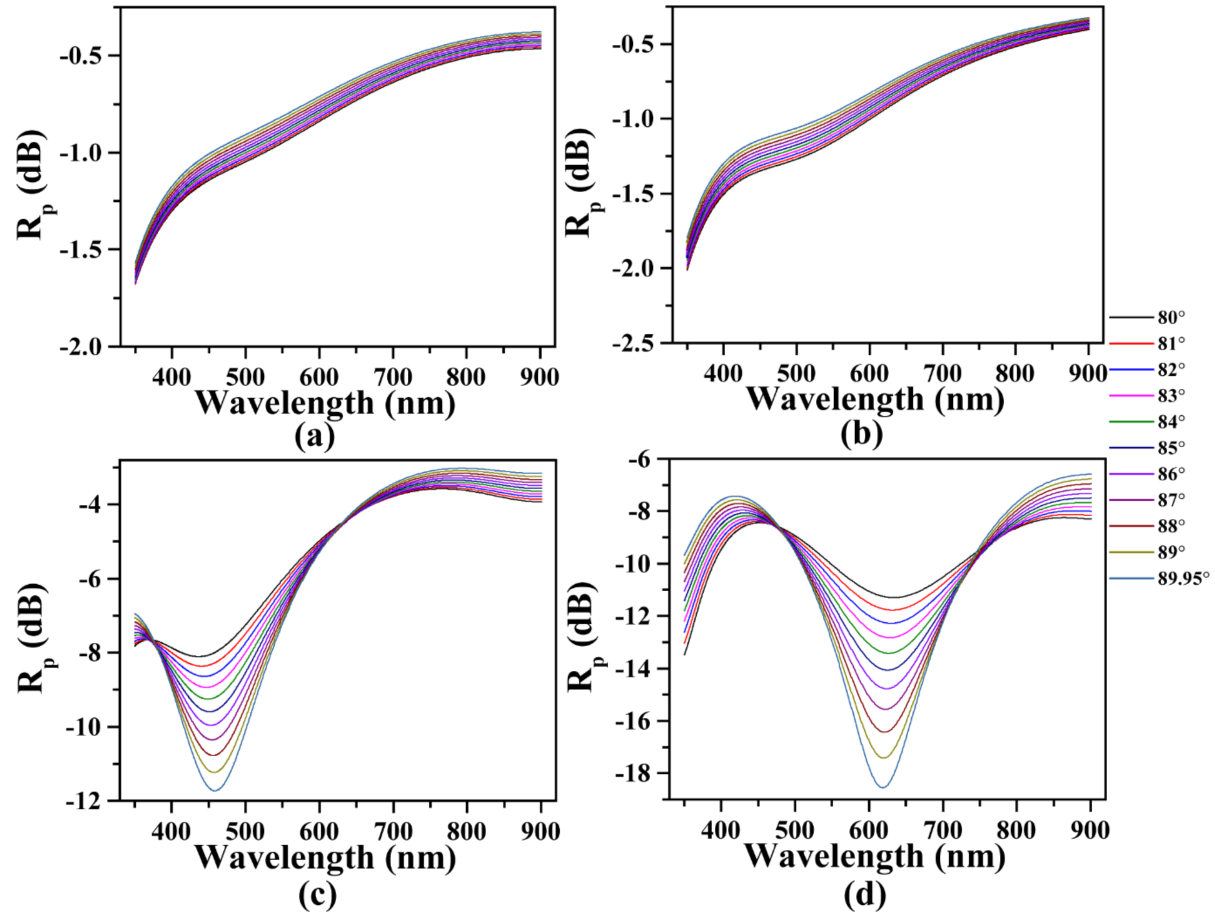

Figure 6-10. Angular distribution of experimentally measured LMR spectra for TM polarization of ITO thin films deposited under vacuum environment at different deposition times: (a) S1 (20 min), (b) S2 (40 min), (c) S3 (80 min), (d) S4 (120 min). The color code used for the incident angles ranging from 80° to 89.95° is given on the right-hand side of the figure.

6.3.4 Refractive index sensing studies

The refractive index sensing potential of the LMR generated by these metallic indium-rich ITO thin films has been explored experimentally by employing the experimental setup presented in Figure 6-1. Sample S4 was used for this purpose since it produces the narrowest LMR response for both TE and TM polarization. Therefore, sample the lowest full-width half-maximum (FWHM) values among all the samples examined here. Lower FWHM value is the primary thing that determines the quality of a refractive index sensor [210]. Experimentally measured LMR response of the sample S4 to different SMRI values for both TE and TM polarizations are as shown in Figure 6-11. (a) and (b), respectively. Slight distortion in experimental at around 972 nm is due to the detector change in ellipsometer from CCD to

TH-2572_156121026

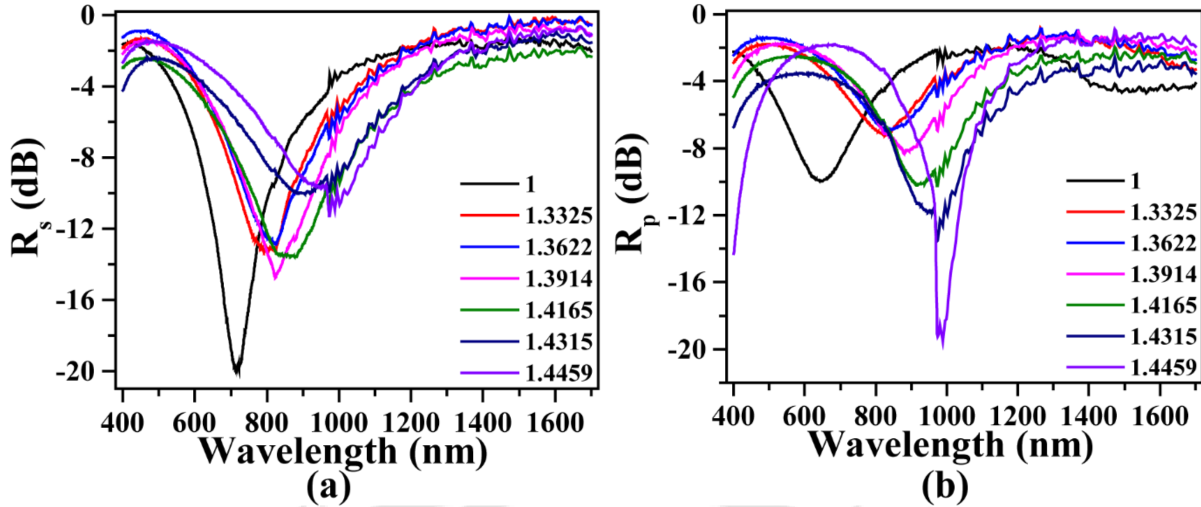

Figure 6-11. Experimentally measured LMR spectra of sample S4 at several SMRI values ranging from 1.3325 (solid black line) – 1.4459 (solid violet line) RIU: (a) for TE polarization, and (b) for TM polarization.

OMA-NIR. A very broad resonance dip located at the NIR wavelength for TM polarization when the surrounding medium is air is a signature of the SPR in sample S4.

Most importantly, for both TE and TM polarizations, considerable red-shift was observed in the LMR wavelength with the increase in SMRI values. Each of these LMR spectra is fitted with a Lorentzian to extract critical information, like FWHM, LMR wavelength, etc. FWHM values of 153 nm for TE polarization and 276 nm for TM polarization observed in the air ambient are the lowest in the thin film based K-R geometry and are in line with the best fiber optics sensors [206] reported in the literature. The low values of the FWHM for TE and TM polarization are testimonials of the effectiveness of metallic indium-rich ITO films as a refractive index sensor. Figure 6-12. (a) – (b) shows the observed LMR wavelengths corresponding to each refractive index value (given in RIU) for both TE and TM polarizations in. Calculated sensitivities ($\text{Sensitivity} = \frac{\Delta\lambda}{\Delta n}$, i.e., the ratio of change in LMR wavelength to the change in refractive index values) are also given in the same figure for each wavelength step. The present work has achieved the highest sensitivities up to 3840 nm/ RIU and 2452 nm/RIU for TE and TM polarization, respectively. These highest sensitivity values are at least six times and two times greater than the previously reported sensitivity for TE and TM polarization, respectively, in the case of K-R geometry based refractometer [117]. Additionally, highest reported sensitivities in this case are almost in line with surface plasmon

TH-2572_156121026

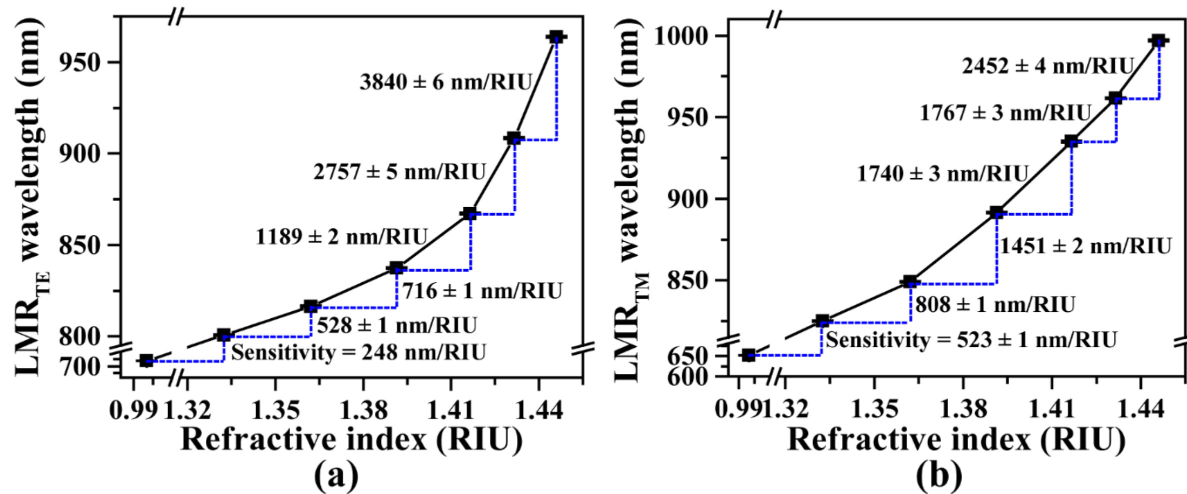

Figure 6-12. Calculated (via Lorentz fitting of the LMR spectra) LMR wavelength at different refractive index values: (a) for TE polarization and (b) for TM polarization. A scale break is given in both figures over the refractive index range of 1.02 – 1.3125 RIU. In the y-axis, a scale break is put at the wavelength range of 750 – 795 nm for figure (a) and 680 – 815 nm for figure (b). The error involved in determining LMR wavelength via Lorentz curve fitting is also indicated in terms of error bar for each LMR wavelength value. The sensitivity of LMR for every refractive index increment step is also given in both figures (a) and (b).

resonance (SPR) based plasmonic sensors, which has typical sensitivity in the range 10^3−10^5 nm/RIU [211]. It is to be noted that the LMR wavelength vs. refractive index curve is nonlinear in the case of TE polarization, and the sensitivity increases considerably at higher refractive index values. Contrary to this, the variation is almost linear for TM polarization. In the case of TE polarization, the whole range of refractive index values was divided into two regions, i.e., region I (1.3325 - 1.3914 in RIU) and region II (1.4165 - 1.4459 in RIU), and both the region linear fitted as shown in the inset of Figure 6-13. (a). While a moderate sensitivity value of 626 nm/ was observed in region I, it reaches as high as 3317 nm/RIU in region II, i.e., at the higher refractive index side. This sensitivity value of 3317 nm/RIU is on par with some of the multimode fibers and complicated D-shaped fiber geometries [208]. However, the linear fit of the LMR wavelength vs. refractive index curve over the whole range for TM polarization, as shown in Figure 6-13. (b), gives a slightly lesser sensitivity of 1133 nm/RIU. It is quite interesting that we have achieved such high sensitivity values in metallic indium-rich ITO films despite the fact it has a considerably higher extinction coefficient, which is known to adversely affect the sensitivity of a refractometer [212], than the pure ITO films. The nanostructured nature of the films can corroborate this peculiar behavior. Previous reports on refractive sensiti-

TH-2572_156121026

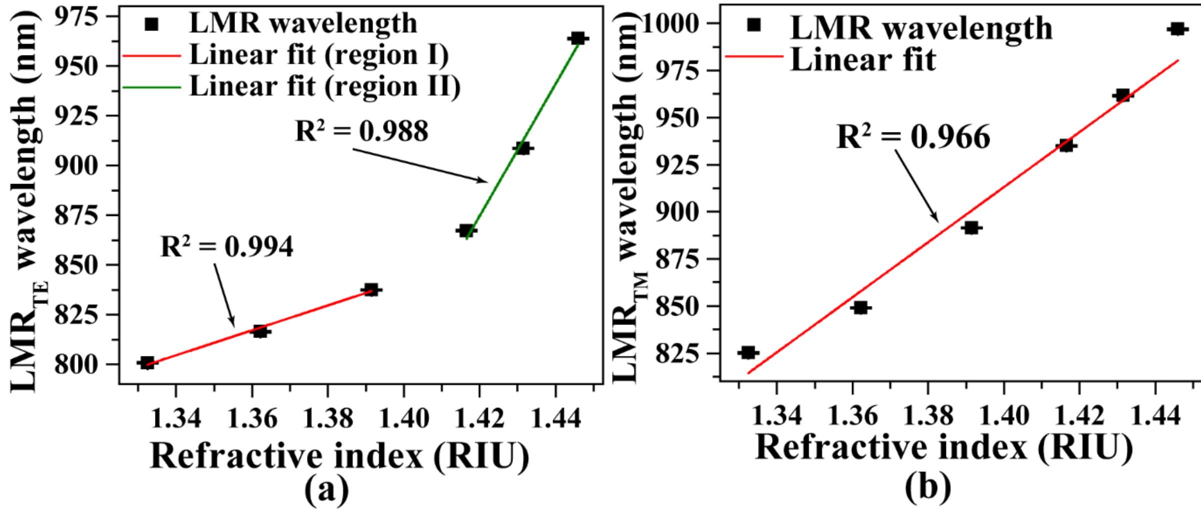

Figure 6-13. (a) linear fit of the LMR wavelengths for TE polarization over the region I (1.3325 - 1.3914; solid red line) and region II (1.4165 - 1.4459; solid olive line) of refractive index values; (b) linear fit of LMR wavelengths for TM polarization over the entire refractive index range (1.3325 – 1.4459).

vity of the LMR also suggest that nanostructuring of the film surface increases the sensitivity quite significantly [72, 213].

6.4 Conclusion

In conclusion, LMR response of PLD-ITO thin films under a vacuum environment having different film thicknesses has been reported both experimentally and numerically. LMR spectra for various incidence angle ranging from 80° to 89.95° is demonstrated experimentally for all the four samples, i.e., sample S1 (lowest thickness) to sample S4 (highest thickness) using simple K-R geometry. As the incidence angle increases, LMR depth increases monotonically, and the dip position also shits to lower wavelengths for all the samples. Additionally, a comparison of the LMR spectra at 89.95° reveals that the depth of the LMR increases, and the LMR position red-shifts significantly with the increasing overall thickness of the vacuum-deposited ITO thin films. A highly intense LMR response with attenuation depth of -20 dB for TE polarization and -10 dB TM polarization is achieved experimentally for the sample S4. The factors identified as the catalyst behind such a high degree of LMR in sample S4 are: the presence of metallic indium and higher overall film thickness compared to other samples. Numerically simulated spectra based on the modified TMM matches quite well the experimental LMR spectra for each sample. Furthermore, refractive index sensing

TH-2572_156121026

capabilities of the metallic indium-rich ITO thin films as an LMR generating platform have been explored experimentally. The highest sensitivities, up to 3840 nm/RIU for TE polarization and 2452 nm/RIU for TM polarization, are achieved in sample S4. These are the highest reported sensitivity values for the K-R geometry based thin film refractometer. Moreover, linear fit in the high refractive index region (1.4165 - 1.4459 in RIU) of the nonlinearly varying LMR wavelength for TE polarization gives a sensitivity value of 3317 nm/RIU, which is in line with the sophisticated fiber optics based refractive index sensors. After establishing metallic indium-rich ITO thin films as a novel material platform for a very high degree of LMR generation in Chapter 5, this Chapter further consolidates the position of this material as a major player in LMR studies with even higher LMR response and very high RI sensitivity values.

TH-2572_156121026

Chapter 7

Conclusion and Future Scope

In the present thesis work, ENZ plasmon resonance and LMR properties of ITO thin films and its metallic indium-rich composites thin film deposited via PLD is studied both experimentally and numerically. PLD-ITO thin films under background gases such as O_2, N_2, Ar and He resulted in the wide tuning of the ENZ wavelength and ENZ plasmon resonance position. In the case of a vacuum environment, however, the surface roughness of the ITO thin films increased manifold compared to the gaseous ones. Thus, a rigorous study has been dedicated to exploring the effect of gradually increasing surface roughness on the ENZ plasmon resonance in the case of vacuum-deposited ITO thin films. In this context, PA has been demonstrated as an application of the ENZ plasmon resonance studies. LMR response of the ITO thin films deposited under different ambient conditions has been compared, and the ITO film deposited under a vacuum environment is established as the superior candidate for LMR generation. The effect of overall film thickness on the LMR properties is investigated in the case of these vacuum-deposited ITO thin films, and RI sensing experiments have been performed as an application of LMR studies.

The 10 wt.% ITO pellet was prepared by sintering the pellets made of the appropriate weight percentage mixture of In_2O_3 and SnO_2 powders at 1400°C for 6 hrs. These pellets were used as a target for depositing ITO thin films via PLD. A second harmonic of *Q*-switched Nd:YAG was focused onto the target to achieve a fixed fluence of 5 J/cm^2. Mainly two sets of samples were deposited: one set was deposited by varying the ambient conditions inside the PLD chamber, and other sets were deposited by varying the deposition time under a high vacuum environment. For all the samples, the target-to-substrate distance and substrate temperature were fixed at 3.5 cm and 400°C, respectively. ENZ plasmon resonance and LMR spectra of the PLD-ITO thin films were collected over the incident angle range 50° – 70° and 80° – 89.95°, respectively, by employing a simple K-R geometry in the SE setup. Important film properties like overall film thickness, surface roughness, complex dielectric constant, refractive index, and extinction coefficient were determined by SE analysis. Surface roughness values obtained from the SE data fitting were also compared with the RMS roughness using

TH-2572_156121026

AFM images. Surface morphologies of PLD-ITO thin films were analyzed by using the FESEM images. Four probe and Hall measurements were carried out to study the electrical properties of the samples. Crystallographic phase analysis of the ITO thin films was done by performing Rietveld refinement over the XRD data.

The effect of background gases, namely, O_2, N_2, Ar, and He gases, on the ENZ wavelength and ENZ plasmon resonance properties of PLD-ITO thin films is studied. The cutoff wavelengths were observed for ITO films deposited only in Ar and He gases over the wavelength range of 900 – 1700 nm. This behavior is corroborated by the increased carrier concertation in such films as compared to the ITO films deposited in O_2 and N_2 gases. The increase in carrier concentration is due to the enhancement of oxygen vacancies, which is also evident from the occurrence of (400) peak in the XRD data of ITO film deposited under Ar, and He gases. The gradual decrease in NIR transmission from the ITO film deposited under O_2 gas to that deposited under He gas is correlated to the increase in free carrier absorption coming from the increase in carrier concentration. Excellent agreement has been established between the RMS surface roughness determined by AFM and sheet resistance measured by four probe measurements to the values predicted by the SE analysis. As expected, no resonance behavior was observed in ITO thin films deposited under O_2 and N_2 gases in the measured wavelength range. For the incident angle of 50°, clear resonance dips were observed at the wavelengths of 1359 nm and 1415 nm for ITO thin film deposited under Ar and He gases, respectively. Furthermore, the resonance positions remain relatively constant with the increase in incident angle, indicating that the resonance is coming from CPs. Electric field localization over a narrow wavelength domain is responsible for this angular invariancy. In addition to this, a greater LFIEF value in the ITO film deposited under He gas as compared to that deposited under Ar gas is responsible for the greater absorption in the former. The experimentally measured ENZ plasmon spectra of each sample are being described to a reasonable level of accuracy with the help of the modified TMM method.

In the case of vacuum-deposited ITO thin films, the increase in deposition time from 20 min (S1) to 40 min (S2) and then to 80 min (S3) resulted in an increase in RMS roughness from 17.6 ± 3.2 nm to 29.7 ± 6.2 nm to 58.1 ± 14.4 nm. With this increase in surface roughness, the absorption due to the ENZ plasmon resonance increased monotonically and reached its maximum value of 99.75% at the wavelength 1335 nm for S3. The randomly rough surfaces

TH-2572_156121026

of vacuum-deposited ITO thin films have been modeled in SE by considering the film + surface roughness layer. While the bottom film layer is modeled by the DL model, ABEMA is applied with the PEC approximation for the upper surface roughness layer. PEC condition is only applicable to the particulates distributed over the surface of such films, and these individual particulates basically act as local capacitors in accordance with the concept of CPR. It is shown that CPs can exist even if one of the capacitor plates has randomly rough termination. The numerical fitting capability of the modified TMM is compared with a well-known generalized TMM method that is applicable to the metamaterial, and it is established that the modified TMM performs much better in handling the ransom surface features of these vacuum deposited ITO thin films. Based on this agreement, the numerical analysis was extended well below the lowest achievable angle by experiments, i.e., 50°. All the samples were found to have much lower absorption values in lower angles, and the maximum absorption of 99.87%, i.e., close to PA, was observed for S3. A high degree of electric field enhancement is responsible for such a high degree of ENZ plasmon-mediated absorption. Surface roughness plays a crucial role in achieving PA in randomly rough ITO thin films, as evident from absorption loss density analysis. The three-layer ENZ *mode* equation for pristine ENZ thin films is updated to a four-layer description to integrate the surface roughness as an anisotropic layer.

LMR response of vacuum-deposited ITO thin films is compared with the films deposited under background gases to establish the outright superiority of the former. LMR response as high as −14.3 dB for TE polarization and −6.4 dB for TM polarization was reported for the vacuum-deposited ITO thin film, while for the ITO film deposited under He gas, best performing ITO film among the film deposited under gaseous environment, the LMR attenuation was merely −1.4 dB for TE polarization. This huge difference in LMR attenuation values among the ITO thin films deposited in vacuum and gaseous environments is correlated to the presence of metallic indium in the vacuum-deposited ITO thin films. Metallic indium, with its strong interbands at the visible range, is responsible for the huge extinction coefficient values in the viable region, increasing the LMR attenuation value manifold. Similar to the previous analyses, the experimental LMR spectra of PLD-ITO thin films are simulated to a reasonable level of accuracy with the help of modified TMM. In addition to this, two films were deposited under a vacuum environment with the same surface roughness value but different metallic indium percentages to further verify the origin of the LMR enhancement in

TH-2572_156121026

vacuum-deposited ITO thin films. It is observed that the ITO thin film with a higher metallic indium percentage has a much deeper LMR response than the film having a lower metallic indium percentage.

The effect of film thickness on the LMR response of metallic indium-rich ITO thin films is studied by varying deposition time under vacuum environment. LMR positon gradually shifted to lower wavelengths as the incident angle was increased from 80 to 89.95°. On the other hand, as the overall thickness increased, the LMR position showed a quite significant red shift for both TE and TM polarization. Also, the LMR intensity increased abruptly from S1 to S4. The experimentally measured LMR attenuation values reached as far as -20 dB for TE polarization and -10 dB TM polarization in the case of S4. This is the highest reported LMR attenuation value in the literature of thin film based K-R geometry. The thing that makes it more outstanding is that such a high value has been achieved in simple K-R geometry without the use of any custom-made all-side-polished prism. Higher overall thickness along with the presence of metallic indium is responsible for such a high attenuation value in S4. Numerically simulated LMR spectra at different incident angles matched quite well with the experimentally measured LMR spectra of the vacuum-deposited ITO thin films. This analysis further reinforces the superiority argument of modified TMM when it comes to the numerical modeling of experimental reflection spectra of PLD-ITO thin films. As an application of the LMR studies, RI sensing experiments were carried out for different concentration of water and glycerol mixture. RI sensitivity as high as 3840 nm/RIU for TE polarization and 2452 nm/RIU for TM polarization was achieved for the highest RI point. These values are at least 6 times higher than previously reported RI sensitivity for TE polarization and 2 times higher for TM polarization.

Future Scopes:

The current thesis is mainly dedicated to studying and understanding the behavior of ENZ plasmon resonance and LMR of PLD-ITO thin films at different ambient conditions and deposition times (under vacuum). PLD-ITO thin films, especially the ones deposited under He gas, could prove to be an excellent material candidate for future ENZ-based devices because of their comparatively low optical losses. In addition to this, He gas pressure inside the PLD chamber could be varied in a systematic way to look for ITO thin films with even better ENZ

TH-2572_156121026

properties. The four-layer ENZ *mode* equation could be extremely helpful in understanding the optical behavior of any real-world ENZ thin film based devices having any degree of surface roughness. Extremely high values of LMR-led absorption in metallic indium-rich ITO thin films indicates the possibility of obtaining wavelength tunable perfect absorber solely based on LMR in the near future. Also, the high RI sensitivity of metallic indium-rich ITO thin films suggests that this material can be applied to enhance the sensitivity of already-existing LMR sensors, especially the fiber optics ones. A future study about the effect of the tin doping concentration and metal (gold, silver, copper, etc.) doping on the LMR response of ITO thin films could be very interesting.

TH-2572_156121026

Bibliography

[1] H.A. Macleod, H.A. Macleod, *Thin-film optical filters*, CRC press, 2010.

[2] N. Gilbert, Touch Screen Indium Tin Oxide (ITO), https://www.azom.com/article.aspx?ArticleID=9634.

[3] Indium-Tin-Oxide, https://www.sciencedirect.com/topics/engineering/indium-tin-oxide.

[4] P.v. Tien, Light waves in thin films and integrated optics, *Appl. Opt.* **10** (1971) 2395-2413.

[5] A.B.S. Leránoz, Study and design of thin-film-deposited optical biosensing devices based on wavelength detection of resonances, in, Universidad Pública de Navarra, 2015.

[6] Q. Wang, W.-M. Zhao, A comprehensive review of lossy mode resonance-based fiber optic sensors, *Opt. Lasers Eng.* **100** (2018) 47-60.

[7] H.A. Atwater, The promise of plasmonics, *Sci. Am.* **296** (2007) 56-63.

[8] S.A. Maier, *Plasmonics: fundamentals and applications*, Springer Science & Business Media, 2007.

[9] L. Novotny, B. Hecht, *Principles of nano-optics*, Cambridge university press, 2012.

[10] E.K. Akowuah, *et al.*, Design and optimization of a novel surface plasmon resonance biosensor based on Otto configuration, *Opt. Express* **17** (2009) 23511-23521.

[11] H.R. Gwon, S.H. Lee, Spectral and angular responses of surface plasmon resonance based on the Kretschmann prism configuration, *Mater. Trans.* **51** (2010) 1150-1155.

[12] M. Seo, *et al.*, Grating-coupled surface plasmon resonance on bulk stainless steel, *Opt. Express* **25** (2017) 26939-26949.

[13] Y. Dai, *et al.*, Experimental demonstration of high sensitivity for silver rectangular grating-coupled surface plasmon resonance (SPR) sensing, *Opt. Commun.* **416** (2018) 66-70.

[14] A.K. Sharma, *et al.*, Fiber-optic sensors based on surface plasmon resonance: a comprehensive review, *IEEE Sens. J.* **7** (2007) 1118-1129.

[15] A. Otto, Excitation of nonradiative surface plasma waves in silver by the method of frustrated total reflection, *Z. Phys. A Hadrons nucl.* **216** (1968) 398-410.

[16] E. Kretschmann, Die bestimmung optischer konstanten von metallen durch anregung von oberflachenplasmaschwingungen, *Z. Phys. A Hadrons nucl.* **241** (1971) 313-324.

[17] J. Homola, *Surface plasmon resonance based sensors*, Springer Science & Business Media, 2006.

TH-2572_156121026

[18] R. Nuster, *et al.*, Comparison of surface plasmon resonance devices for acoustic wave detection in liquid, *Opt. Express* **15** (2007) 6087-6095.

[19] H. Raether, *Surface plasmons on gratings*, in: Surface plasmons on smooth and rough surfaces and on gratings, Springer, 1988, pp. 91-116.

[20] J. Homola, *et al.*, Surface plasmon resonance sensors, *Sens. Actuators B Chem.* **54** (1999) 3-15.

[21] J. Homola, Surface plasmon resonance sensors for detection of chemical and biological species, *Chem. Rev.* **108** (2008) 462-493.

[22] Biacore SPR Systems, https://www.cytivalifesciences.com/en/us/shop/protein-analysis/spr-label-free-analysis/systems.

[23] Reichert 4SPR, https://www.reichertspr.com/products/surface-plasmon-resonance-systems/reichert-4spr/.

[24] XanTec's SPR Biosensors, https://www.xantec.com/products/spr_biosensors/index.php.

[25] R. Pilolli, *et al.*, Advances in biosensor development based on integrating nanotechnology and applied to food-allergen management, *Trends Anal. Chem.* **47** (2013) 12-26.

[26] J. Zhou, *et al.*, Surface plasmon resonance (SPR) biosensors for food allergen detection in food matrices, *Biosens. Bioelectron.* **142** (2019) 111449.

[27] M. Svedendahl, *et al.*, Refractometric sensing using propagating versus localized surface plasmons: a direct comparison, *Nano Lett.* **9** (2009) 4428-4433.

[28] B. Dey, *et al.*, Numerical design of high-performance WS2/metal/WS2/graphene heterostructure based surface plasmon resonance refractive index sensor, *Results Phys.* **23** (2021) 104021.

[29] D. Yang, *et al.*, Surface plasmon resonance of SnO2/Au Bi-layer films for gas sensing applications, *Sens. Actuators B Chem.* **145** (2010) 832-838.

[30] A.K. Mishra, S.K. Mishra, Gas sensing in Kretschmann configuration utilizing bi-metallic layer of rhodium-silver in visible region, *Sens. Actuators B Chem.* **237** (2016) 969-973.

[31] E. Maciak, *et al.*, Effect of humidity on NH3 gas sensitivity of nafion/WO3 sensing structure of SPR sensor, *Molecular Quantum Acoustics* **26** (2005) 205.

[32] J. Mapel, *et al.*, Plasmonic excitation of organic double heterostructure solar cells, *Appl. Phys. Lett.* **90** (2007) 121102.

[33] B. Park, *et al.*, Surface plasmon excitation in semitransparent inverted polymer photovoltaic devices and their applications as label-free optical sensors, *Light Sci. Appl.* **3** (2014) e222-e222.

[34] H. Memmi, *et al.*, Strong coupling between surface plasmon polaritons and molecular vibrations, *Phys. Rev. Lett.* **118** (2017) 126802.

TH-2572_156121026

[35] I. Shlesinger, *et al.*, Strong coupling of nanoplatelets and surface plasmons on a gold surface, *ACS Photonics* **6** (2019) 2643-2648.

[36] M. Specht, *et al.*, Scanning plasmon near-field microscope, *Phys. Rev. Lett.* **68** (1992) 476.

[37] M. Lenner, *et al.*, Field enhancement and rectification of surface plasmons detected by scanning tunneling microscopy, *Phys. Rev. B* **83** (2011) 205428.

[38] T. Heilpern, *et al.*, Determination of hot carrier energy distributions from inversion of ultrafast pump-probe reflectivity measurements, *Nat. Commun.* **9** (2018) 1-6.

[39] M. Marciniak, *et al.*, Analysis of lossy mode cut-off conditions in planar waveguides with semiconductor guiding layer, *IEE proc. J Optoelectron.* **140** (1993) 247-252.

[40] N. Paliwal, J. John, Lossy mode resonance (LMR) based fiber optic sensors: A review, *IEEE Sens. J.* **15** (2015) 5361-5371.

[41] I. Del Villar, *et al.*, Lossy mode resonance generation with indium-tin-oxide-coated optical fibers for sensing applications, *J. Light. Technol.* **28** (2009) 111-117.

[42] Fiber Optic Basics, https://www.newport.com/t/fiber-optic-basics.

[43] I. Del Villar, *et al.*, Optical sensors based on lossy-mode resonances, *Sens. Actuators B Chem.* **240** (2017) 174-185.

[44] I. Del Villar, *et al.*, Experimental demonstration of lossy mode and surface plasmon resonance generation with Kretschmann configuration, *Opt. Lett.* **40** (2015) 4739-4742.

[45] O. Fuentes, *et al.*, Lossy mode resonance sensors based on lateral light incidence in nanocoated planar waveguides, *Sci. Rep.* **9** (2019) 8882.

[46] I. Dominguez, *et al.*, Dually nanocoated planar waveguides towards multi-parameter sensing, *Sci. Rep.* **11** (2021) 3669.

[47] F. Chiavaioli, D. Janner, Fiber Optic Sensing With Lossy Mode Resonances: Applications and Perspectives, *J. Light. Technol.* **39** (2021) 3855-3870.

[48] M. Hernáez, *et al.*, Optical fiber refractometers based on lossy mode resonances supported by TiO 2 coatings, *Appl. Opt.* **49** (2010) 3980-3985.

[49] M. Smietana, *et al.*, Label-free sensitivity of long-period gratings enhanced by atomic layer deposited TiO 2 nano-overlays, *Opt. Express* **23** (2015) 8441-8453.

[50] C.-L. Tien, *et al.*, Lossy mode resonance sensors fabricated by RF magnetron sputtering GZO thin film and D-shaped fibers, *Coatings* **10** (2020) 29.

[51] A. Ozcariz, *et al.*, Is there a frontier in sensitivity with Lossy mode resonance (LMR) based refractometers?, *Sci. Rep.* **7** (2017) 10280.

TH-2572_156121026

[52] J. Ascorbe, *et al.*, High sensitivity humidity sensor based on cladding-etched optical fiber and lossy mode resonances, *Sens. Actuators B Chem.* **233** (2016) 7-16.

[53] D. Bohorquez, *et al.*, Wavelength and intensity based lossy mode resonance breathing sensor, *Opt. Laser Technol.* **140** (2021) 107063.

[54] V. Lioubimov, *et al.*, Effect of varying electric potential on surface-plasmon resonance sensing, *Appl. Opt.* **43** (2004) 3426-3432.

[55] C. Zamarreño, *et al.*, Optical fiber pH sensor based on lossy-mode resonances by means of thin polymeric coatings, *Sens. Actuators B Chem.* **155** (2011) 290-297.

[56] A. Paliwal, *et al.*, Surface plasmon resonance study on the optical sensing properties of tin oxide (SnO2) films to NH3 gas, *J. Appl. Phys.* **119** (2016) 164502.

[57] S.K. Mishra, *et al.*, A lossy mode resonance-based fiber optic hydrogen gas sensor for room temperature using coatings of ITO thin film and nanoparticles, *Meas. Sci. Technol.* **27** (2016) 045103.

[58] M. Hernaez, *et al.*, Graphene oxide in lossy mode resonance-based optical fiber sensors for ethanol detection, *Sensors* **18** (2018) 58.

[59] P. Kuznetsov, *et al.*, Fiber optic Lossy Mode Resonance based sensor for aggressive liquids, *Sens. Actuator A Phys.* **321** (2021) 112576.

[60] F. Chiavaioli, *et al.*, Femtomolar detection by nanocoated fiber label-free biosensors, *ACS sensors* **3** (2018) 936-943.

[61] P. Zubiate, *et al.*, High sensitive and selective C-reactive protein detection by means of lossy mode resonance based optical fiber devices, *Biosens. Bioelectron.* **93** (2017) 176-181.

[62] M. Janik, *et al.*, Electrochemically directed biofunctionalization of a lossy-mode resonance optical fiber sensor, *Opt. Express* **28** (2020) 15934-15942.

[63] F. Yang, *et al.*, Long-range coupled surface exciton polaritons, *Phys. Rev. Lett.* **64** (1990) 559.

[64] G. Bryan-Brown, *et al.*, Prism and grating coupling to long-range coupled-surface exciton–polaritons, *J. Opt. Soc. Am. B* **8** (1991) 765-769.

[65] V. Giannini, *et al.*, Long-range surface polaritons in ultra-thin films of silicon, *Opt. Express* **16** (2008) 19674-19685.

[66] N.B. Grosse, *et al.*, Utilizing strongly absorbing materials for low-loss surface-wave nonlinear optics, *Phys. Rev. A* **97** (2018) 043844.

[67] F. Yang, *et al.*, Long-range surface modes supported by thin films, *Phys. Rev. B* **44** (1991) 5855.

[68] F. Yang, J. Sambles, Experimental observation of thermo-optic nonlinearity with a long-range surface wave supported by a very thin palladium film, *J. Mod. Opt.* **39** (1992) 485-498.

TH-2572_156121026

[69] G.V. Naik, *et al.*, Alternative plasmonic materials: beyond gold and silver, *Adv. Mater.* **25** (2013) 3264-3294.

[70] P.R. West, *et al.*, Searching for better plasmonic materials, *Laser Photonics Rev.* **4** (2010) 795-808.

[71] C.R. Zamarreno, *et al.*, Sensing properties of indium oxide coated optical fiber devices based on lossy mode resonances, *IEEE Sens. J.* **12** (2011) 151-155.

[72] S.P. Usha, *et al.*, Fiber optic hydrogen sulfide gas sensors utilizing ZnO thin film/ZnO nanoparticles: A comparison of surface plasmon resonance and lossy mode resonance, *Sens. Actuators B Chem.* **218** (2015) 196-204.

[73] A. Ozcariz, *et al.*, Aluminum doped zinc oxide (AZO) coated optical fiber LMR refractometers—An experimental demonstration, *Sens. Actuators B Chem.* **281** (2019) 698-704.

[74] A. Ozcariz, *et al.*, Lossy mode resonance optical sensors based on indium-gallium-zinc oxide thin film, *Sens. Actuator A Phys.* **290** (2019) 20-27.

[75] A. Andreev, *et al.*, A refractometric sensor using index-sensitive mode resonance between single-mode fiber and thin film amorphous silicon waveguide, *Sens. Actuators B Chem.* **106** (2005) 484-488.

[76] L. Wu, *et al.*, Lossy-mode-resonance sensor based on perovskite nanomaterial with high sensitivity, *Opt. Express* **29** (2021) 17602-17612.

[77] U. Betz, *et al.*, Thin films engineering of indium tin oxide: large area flat panel displays application, *Surf. Coat. Technol.* **200** (2006) 5751-5759.

[78] Z. Liu, *et al.*, Flexible Indium-Tin-Oxide Homojunction Thin-Film Transistors with Two In-Plane Gates on Cellulose-Nanofiber-Soaked Papers, *Adv. Electron. Mater.* **5** (2019) 1900235.

[79] S. Suresh, *et al.*, Enhanced nonlinear optical responses of layered epsilon-near-zero metamaterials at visible frequencies, *ACS Photonics* **8** (2020) 125-129.

[80] A. Iwan, *et al.*, Optical, electrical and mechanical properties of indium tin oxide on polyethylene terephthalate substrates: Application in bulk-heterojunction polymer solar cells, *Mater. Sci. Semicond. Process.* **24** (2014) 110-116.

[81] Y.W. Kim, *et al.*, Tailoring Opto-electrical properties of ultra-thin indium tin oxide films via filament doping: Application as a transparent cathode for indoor organic photovoltaics, *J. Power Sources* **424** (2019) 165-175.

[82] Y. Sung, *et al.*, Anti-reflective coating with a conductive indium tin oxide layer on flexible glass substrates, *Appl. Opt.* **57** (2018) 2202-2207.

[83] P. Yilmaz, *et al.*, Spectrally selective PANI/ITO nanocomposite electrodes for energy-efficient dual band electrochromic windows, *ACS Appl. Energy Mater.* **3** (2020) 3779-3788.

TH-2572_156121026

[84] S. Dietrich, *et al.*, Evaluation of Indium Tin Oxide for Gas Sensing Applications: Adsorption/Desorption and Electrical Conductivity Studies on Powders and Thick Films, *Sensors* **21** (2021) 497.

[85] D.S. Ginley, C. Bright, Transparent conducting oxides, *MRS Bull.* **25** (2000) 15-18.

[86] M. Marezio, Refinement of the crystal structure of In2O3 at two wavelengths, *Acta Crystallogr.* **20** (1966) 723-728.

[87] G. Giusti, Deposition and characterisation of functional ITO thin films, in, University of Birmingham, 2011.

[88] R. Bel Hadj Tahar, *et al.*, Tin doped indium oxide thin films: Electrical properties, *J. Appl. Phys.* **83** (1998) 2631-2645.

[89] Z. Ma, *et al.*, Indium-tin-oxide for high-performance electro-optic modulation, *Nanophotonics* **4** (2015) 198-213.

[90] J.C. Fan, J.B. Goodenough, X-ray photoemission spectroscopy studies of Sn-doped indium-oxide films, *J. Appl. Phys.* **48** (1977) 3524-3531.

[91] E. Burstein, Anomalous optical absorption limit in InSb, *Phys. Rev.* **93** (1954) 632.

[92] C. Rhodes, *et al.*, Surface plasmon resonance in conducting metal oxides, *J. Appl. Phys.* **100** (2006) 054905.

[93] X. Liu, *et al.*, Electrical tuning of a quantum plasmonic resonance, *Nat. Nanotechnol.* **12** (2017) 866-870.

[94] M. Guizzardi, *et al.*, Large scale indium tin oxide (ITO) one dimensional gratings for ultrafast signal modulation in the visible spectral region, *Phys. Chem. Chem. Phys.* **22** (2020) 6881-6887.

[95] C. Rhodes, *et al.*, Dependence of plasmon polaritons on the thickness of indium tin oxide thin films, *J. Appl. Phys.* **103** (2008) 093108.

[96] J. Kim, *et al.*, Plasmonic resonances in nanostructured transparent conducting oxide films, *IEEE J. Sel. Top. Quantum Electron* **19** (2013) 4601907-4601907.

[97] C. Chen, *et al.*, Tunable near-infrared epsilon-near-zero and plasmonic properties of Ag-ITO co-sputtered composite films, *Sci. Technol. Adv. Mater* **19** (2018) 174-184.

[98] J.B. Khurgin, Replacing noble metals with alternative materials in plasmonics and metamaterials: how good an idea?, *Philos. Trans. Royal Soc. A* **375** (2017) 20160068.

[99] X. Niu, *et al.*, Epsilon-near-zero photonics: a new platform for integrated devices, *Adv. Opt. Mater.* **6** (2018) 1701292.

[100] R.W. Ziolkowski, Propagation in and scattering from a matched metamaterial having a zero index of refraction, *Phys. Rev. E* **70** (2004) 046608.

TH-2572_156121026

[101] N. Kinsey, *et al.*, Epsilon-near-zero Al-doped ZnO for ultrafast switching at telecom wavelengths, *Optica* **2** (2015) 616-622.

[102] J. Bohn, *et al.*, All-optical switching of an epsilon-near-zero plasmon resonance in indium tin oxide, *Nat. Commun.* **12** (2021) 1-6.

[103] M.Z. Alam, *et al.*, Large optical nonlinearity of indium tin oxide in its epsilon-near-zero region, *Science* **352** (2016) 795-797.

[104] M.Z. Alam, *et al.*, Large optical nonlinearity of nanoantennas coupled to an epsilon-near-zero material, *Nat. Photonics* **12** (2018) 79-83.

[105] T.S. Luk, *et al.*, Directional perfect absorption using deep subwavelength low-permittivity films, *Phys. Rev. B* **90** (2014) 085411.

[106] J. Yoon, *et al.*, Broadband epsilon-near-zero perfect absorption in the near-infrared, *Sci. Rep.* **5** (2015) 12788.

[107] B. Edwards, *et al.*, Experimental verification of epsilon-near-zero metamaterial coupling and energy squeezing using a microwave waveguide, *Phys. Rev. Lett.* **100** (2008) 033903.

[108] Y.C. Jun, *et al.*, Epsilon-near-zero strong coupling in metamaterial-semiconductor hybrid structures, *Nano Lett.* **13** (2013) 5391-5396.

[109] S. Vezzoli, *et al.*, Optical time reversal from time-dependent epsilon-near-zero media, *Phys. Rev. Lett.* **120** (2018) 043902.

[110] S. Franzen, *et al.*, Plasmonic phenomena in indium tin oxide and ITO-Au hybrid films, *Opt. Lett.* **34** (2009) 2867-2869.

[111] M. Kang, *et al.*, Near-Infrared Optical Extinction of Indium Tin Oxide Structures Prepared by Nanosphere Lithography, *ACS Photonics* **3** (2016) 1993-1999.

[112] M.A. Kats, *et al.*, Ultra-thin perfect absorber employing a tunable phase change material, *Appl. Phys. Lett.* **101** (2012) 221101.

[113] N. Liu, *et al.*, Infrared perfect absorber and its application as plasmonic sensor, *Nano Lett.* **10** (2010) 2342-2348.

[114] M.L. Brongersma, *et al.*, Light management for photovoltaics using high-index nanostructures, *Nat. Mater.* **13** (2014) 451-460.

[115] W. Li, J. Valentine, Metamaterial perfect absorber based hot electron photodetection, *Nano Lett.* **14** (2014) 3510-3514.

[116] A. Anopchenko, *et al.*, Field-effect tunable and broadband epsilon-near-zero perfect absorbers with deep subwavelength thickness, *ACS Photonics* **5** (2018) 2631-2637.

[117] V. Torres, *et al.*, Indium tin oxide refractometer in the visible and near infrared via lossy mode and surface plasmon resonances with Kretschmann configuration, *Appl. Phys. Lett.* **108** (2016) 043507.

TH-2572_156121026

[118] S. Cho, Effects of rapid thermal annealing on the properties of In2O3 thin films grown on glass substrate by rf reactive magnetron sputtering, *Microelectron. Eng.* **89** (2012) 84-88.

[119] J. Stankiewicz*, et al.*, Structural and electrical properties of indium oxide thin films grown by pulsed laser deposition in oxygen ambient, *J. Alloys Compd.* **694** (2017) 1280-1286.

[120] V. Senthilkumar, P. Vickraman, Annealing temperature dependent on structural, optical and electrical properties of indium oxide thin films deposited by electron beam evaporation method, *Curr. Appl. Phys.* **10** (2010) 880-885.

[121] Q. Ma*, et al.*, Atomic-layer-deposition of indium oxide nano-films for thin-film transistors, *Nanoscale Res. Lett.* **13** (2018) 4.

[122] N. Pramod*, et al.*, Structural, optical and methanol sensing properties of sprayed In2O3 nanoparticle thin films, *Ceram. Int.* **38** (2012) 4151-4158.

[123] D.H. Lowndes*, et al.*, Synthesis of novel thin-film materials by pulsed laser deposition, *Science* **273** (1996) 898-903.

[124] H.M. Smith, A. Turner, Vacuum deposited thin films using a ruby laser, *Appl. Opt.* **4** (1965) 147-148.

[125] D. Dijkkamp*, et al.*, Preparation of Y-Ba-Cu oxide superconductor thin films using pulsed laser evaporation from high T c bulk material, *Appl. Phys. Lett.* **51** (1987) 619-621.

[126] B. Roas*, et al.*, Epitaxial growth of YBa2Cu3O7− x thin films by a laser evaporation process, *Appl. Phys. Lett.* **53** (1988) 1557-1559.

[127] H.M. Christen, G. Eres, Recent advances in pulsed-laser deposition of complex oxides, *J. Condens. Matter Phys.* **20** (2008) 264005.

[128] J. Yao*, et al.*, Production of large-area 2D materials for high-performance photodetectors by pulsed-laser deposition, *Prog. Mater. Sci.* **106** (2019) 100573.

[129] M.N. Ashfold*, et al.*, Pulsed laser ablation and deposition of thin films, *Chem. Soc. Rev.* **33** (2004) 23-31.

[130] D.B. Chrisey, G.K. Hubler, Pulsed laser deposition of thin films, (1994).

[131] H. Kim*, et al.*, Electrical, optical, and structural properties of indium–tin–oxide thin films for organic light-emitting devices, *J. Appl. Phys.* **86** (1999) 6451-6461.

[132] T.-K. Yong*, et al.*, Pulsed laser deposition of indium tin oxide nanowires in argon and helium, *Mater. Lett.* **66** (2012) 280-281.

[133] T.K. Yong*, et al.*, Pulsed laser deposition of nanostructured indium-tin-oxide film, *Nanostructured Thin Films III* **7766** (2010) 776615.

[134] J. Perriére*, et al.*, Formation of metallic nanoclusters in oxygen deficient indium tin oxide films, *J. Appl. Phys.* **109** (2011) 123704.

TH-2572_156121026

[135] E. Millon, *et al.*, Phase separation in nanocomposite indium tin oxide thin films grown at room temperature: on the role of oxygen deficiency, *J. Mater. Chem.* **22** (2012) 12179-12185.

[136] G.V. Naik, *et al.*, Oxides and nitrides as alternative plasmonic materials in the optical range, *Opt. Mater. Express* **1** (2011) 1090-1099.

[137] X. Fang, *et al.*, Pulsed laser deposited indium tin oxides as alternatives to noble metals in the near-infrared region, *J. Condens. Matter Phys.* **28** (2016) 224009.

[138] S. Xian, *et al.*, Effect of oxygen stoichiometry on the structure, optical and epsilon-near-zero properties of indium tin oxide films, *Opt. Express* **27** (2019) 28618-28628.

[139] D. Mills, A. Maradudin, Surface roughness and the optical properties of a semi-infinite material; the effect of a dielectric overlayer, *Phys. Rev. B* **12** (1975) 2943.

[140] F. Toigo, *et al.*, Optical properties of rough surfaces: general theory and the small roughness limit, *Phys. Rev. B* **15** (1977) 5618.

[141] E. Kretschmann, *et al.*, Splitting of the dispersion relation of surface plasmons on a rough surface, *Phys. Rev. Lett.* **42** (1979) 1312.

[142] E. Fontana, R. Pantell, Characterization of multilayer rough surfaces by use of surface-plasmon spectroscopy, *Phys. Rev. B* **37** (1988) 3164.

[143] A. Kolomenski, *et al.*, Propagation length of surface plasmons in a metal film with roughness, *Appl. Opt.* **48** (2009) 5683-5691.

[144] I. Kotelnikov, G. Stupakov, Dispersion relation of a surface wave at a rough metal-air interface, *Phys. Rev. A* **94** (2016) 053847.

[145] I. Del Villar, *et al.*, Design rules for lossy mode resonance based sensors, *Appl. Opt.* **51** (2012) 4298-4307.

[146] P. Willmott, J. Huber, Pulsed laser vaporization and deposition, *Rev. Mod. Phys.* **72** (2000) 315.

[147] D.R. NORTON, Pulsed Laser Deposition of Complex Materials: Progress, (2007) 1.

[148] H. Fujiwara, *Spectroscopic ellipsometry: principles and applications*, John Wiley & Sons, 2007.

[149] J.J. Moré, *The Levenberg-Marquardt algorithm: implementation and theory*, in: Numerical analysis, Springer, 1978, pp. 105-116.

[150] *Spectroscopic Ellipsometry Analyzer: User's Referenc e Manual*, Semilab Co. Ltd., 2012.

[151] D. Schmidt, M. Schubert, Anisotropic Bruggeman effective medium approaches for slanted columnar thin films, *J. Appl. Phys.* **114** (2013) 083510.

[152] A. Mock, *et al.*, Anisotropy, band-to-band transitions, phonon modes, and oxidation properties of cobalt-oxide core-shell slanted columnar thin films, *Appl. Phys. Lett.* **108** (2016) 051905.

TH-2572_156121026

[153] B.C. Bergner, *et al.*, Effective medium approximations for modeling optical reflectance from gratings with rough edges, *J. Opt. Soc. Am. A* **27** (2010) 1083-1090.

[154] E. Le Ru, P. Etchegoin, *Principles of Surface-Enhanced Raman Spectroscopy: and related plasmonic effects*, Elsevier, 2008.

[155] D.W. Berreman, Optics in stratified and anisotropic media: 4× 4-matrix formulation, *J. Opt. Soc. Am.* **62** (1972) 502-510.

[156] G. Smith, Theory of angular selective transmittance in oblique columnar thin films containing metal and voids, *Appl. Opt.* **29** (1990) 3685-3693.

[157] M. Skorobogatiy, *Nanostructured and Subwavelength Waveguides: fundamentals and applications*, John Wiley & Sons, 2012.

[158] B. Thestrup, *et al.*, Electrical and optical properties of thin indium tin oxide films produced by pulsed laser ablation in oxygen or rare gas atmospheres, *Appl. Surf. Sci.* **142** (1999) 248-252.

[159] T. Yong, *et al.*, Pulsed Nd: YAG laser deposition of indium tin oxide thin films in different gases and organic light emitting device applications, *Thin Solid Films* **516** (2008) 4267-4271.

[160] M. Morales-Paliza, *et al.*, Nitrogen as background gas in pulsed-laser deposition growth of indium tin oxide films at room temperature, *Thin Solid Films* **429** (2003) 220-224.

[161] R. Savu, E. Joanni, Influence of ambient gas on the growth and properties of porous tin-doped indium oxide thin films made by pulsed laser deposition, *Thin Solid Films* **515** (2007) 7813-7819.

[162] B. Johns, *et al.*, Epsilon-near-zero response in indium tin oxide thin films: octave span tuning and IR plasmonics, *J. Appl. Phys.* **127** (2020) 043102.

[163] P. Thilakan, J. Kumar, Studies on the preferred orientation changes and its influenced properties on ITO thin films, *Vacuum* **48** (1997) 463-466.

[164] M. Fusi, *et al.*, Surface electronic and structural properties of nanostructured titanium oxide grown by pulsed laser deposition, *Surf. Sci.* **605** (2011) 333-340.

[165] A. Singh, *et al.*, Doping mechanism in aluminum doped zinc oxide films, *J. Appl. Phys.* **95** (2004) 3640-3643.

[166] P. Gondoni, *et al.*, Structural and functional properties of Al: ZnO thin films grown by Pulsed Laser Deposition at room temperature, *Thin Solid Films* **520** (2012) 4707-4711.

[167] Indium tin oxide coated glass slide, rectangular, https://www.sigmaaldrich.com/IN/en/product/aldrich/636916?context=product.

[168] Y. Ke, *et al.*, Resistivity of thin Cu films with surface roughness, *Phys. Rev. B* **79** (2009) 155406.

[169] H. Liu, *et al.*, Enhanced surface plasmon resonance on a smooth silver film with a seed growth layer, *ACS Nano* **4** (2010) 3139-3146.

TH-2572_156121026

[170] M.H. Javani, M.I. Stockman, Real and imaginary properties of epsilon-near-zero materials, *Phys. Rev. Lett.* **117** (2016) 107404.

[171] J. Lacombe, *et al.*, Three dimensional optical modeling of amorphous silicon thin film solar cells using the finite-difference time-domain method including real randomly surface topographies, *J. Appl. Phys.* **110** (2011) 023102.

[172] K. Jäger, *et al.*, Ambiguities in optical simulations of nanotextured thin-film solar cells using the finite-element method, *Opt. Express* **23** (2015) A1060-A1071.

[173] R. Dewan, *et al.*, Analyzing periodic and random textured silicon thin film solar cells by Rigorous Coupled Wave Analysis, *Sci. Rep.* **4** (2014) 6029.

[174] C. Ciracì, *et al.*, Impact of surface roughness in nanogap plasmonic systems, *ACS Photonics* **7** (2020) 908-913.

[175] B. Fodor, *et al.*, Effective medium approximation of ellipsometric response from random surface roughness simulated by finite-element method, *Thin Solid Films* **617** (2016) 20-24.

[176] J.C. MAXWELL-GARNETT, Colours in metal glasses and in metallic films, *Phil. Trans. R. Soc. Lond. A* **203** (1904) 385-420.

[177] V.D. Bruggeman, Berechnung verschiedener physikalischer Konstanten von heterogenen Substanzen. I. Dielektrizitätskonstanten und Leitfähigkeiten der Mischkörper aus isotropen Substanzen, *Ann. Phys. (Berl.)* **416** (1935) 636-664.

[178] N. Dung, *et al.*, Perfect and broad absorption by the active control of electric resonance in metamaterial, *J. Opt.* **17** (2015) 045105.

[179] N. Odebo Länk, *et al.*, Large-scale silicon nanophotonic metasurfaces with polarization independent near-perfect absorption, *Nano Lett.* **17** (2017) 3054-3060.

[180] K. Aydin, *et al.*, Broadband polarization-independent resonant light absorption using ultrathin plasmonic super absorbers, *Nat. Commun.* **2** (2011) 1-7.

[181] A. Poruba, *et al.*, Optical absorption and light scattering in microcrystalline silicon thin films and solar cells, *J. Appl. Phys.* **88** (2000) 148-160.

[182] V. Logeeswaran, *et al.*, Electrical Resistivity & Thermal Stability of Smooth Silver Thin Film for Nanoscale Optoelectronic Devices, *2008 8th IEEE Conference on Nanotechnology* (2008) 92-94.

[183] I.E. Stewart, *et al.*, Effect of morphology on the electrical resistivity of silver nanostructure films, *ACS Appl. Mater. Interfaces* **9** (2017) 1870-1876.

[184] H. Khamh, *et al.*, As good as gold and better: conducting metal oxide materials for mid-infrared plasmonic applications, *J. Mater. Chem. C* **6** (2018) 8326-8342.

[185] Y. Zhang, E. Bahar, Mueller matrix elements that characterize scattering from coated random rough surfaces, *IEEE Trans. Antennas Propag.* **47** (1999) 949-955.

TH-2572_156121026

[186] P.A. Letnes, *et al.*, Calculation of the Mueller matrix for scattering of light from two-dimensional rough surfaces, *Phys. Rev. A* **86** (2012) 031803.

[187] A.A. Orlov, *et al.*, Engineered optical nonlocality in nanostructured metamaterials, *Phys. Rev. B* **84** (2011) 045424.

[188] M.A. Ordal, *et al.*, Optical properties of fourteen metals in the infrared and far infrared: Al, Co, Cu, Au, Fe, Pb, Mo, Ni, Pd, Pt, Ag, Ti, V, and W, *Appl. Opt.* **24** (1985) 4493-4499.

[189] R. Koyama, *et al.*, Optical properties of indium, *Phys. Rev. B* **8** (1973) 2426.

[190] M. El Oker, *et al.*, Optical properties and structure of thin indium films, *Phys. Status Solidi A* **73** (1982) 389-394.

[191] S. Goswami, A.K. Sharma, Investigation of the optical behavior of indium oxide thin films with the aid of spectroscopic ellipsometry technique, *Appl. Surf. Sci.* **495** (2019) 143609.

[192] C.C. Katsidis, D.I. Siapkas, General transfer-matrix method for optical multilayer systems with coherent, partially coherent, and incoherent interference, *Appl. Opt.* **41** (2002) 3978-3987.

[193] A. Trügler, *et al.*, Influence of surface roughness on the optical properties of plasmonic nanoparticles, *Phys. Rev. B* **83** (2011) 081412.

[194] M.A. Badsha, *et al.*, Admittance matching analysis of perfect absorption in unpatterned thin films, *Opt. Commun.* **332** (2014) 206-213.

[195] J.P. Hugonin, P. Lalanne, Reticolo software for grating analysis, *arXiv preprint arXiv:2101.00901* (2021).

[196] S. Feng, K. Halterman, Coherent perfect absorption in epsilon-near-zero metamaterials, *Phys. Rev. B* **86** (2012) 165103.

[197] S. Campione, *et al.*, Theory of epsilon-near-zero modes in ultrathin films, *Phys. Rev. B* **91** (2015) 121408.

[198] W. Chen, J. Chen, Surface plasma wave study of submonolayer Cs and Cs・O covered Ag surfaces, *Surf. Sci.* **91** (1980) 601-617.

[199] I. Pockrand, Surface plasma oscillations at silver surfaces with thin transparent and absorbing coatings, *Surf. Sci.* **72** (1978) 577-588.

[200] C.R. Zamarreño, *et al.*, Experimental demonstration of lossy mode resonance generation for transverse-magnetic and transverse-electric polarizations, *Opt. Lett.* **38** (2013) 2481-2483.

[201] R. Saini, *et al.*, Lossy Mode Resonance-Based Refractive Index Sensor for Sucrose Concentration Measurement, *IEEE Sens. J.* **20** (2019) 1217-1222.

[202] P.B. Johnson, R.-W. Christy, Optical constants of the noble metals, *Phys. Rev. B* **6** (1972) 4370.

TH-2572_156121026

[203] S. D'Elia*, et al.*, Ellipsometry investigation of the effects of annealing temperature on the optical properties of indium tin oxide thin films studied by Drude–Lorentz model, *Appl. Surf. Sci.* **255** (2009) 7203-7211.

[204] Y.S. Jung, Spectroscopic ellipsometry studies on the optical constants of indium tin oxide films deposited under various sputtering conditions, *Thin Solid Films* **467** (2004) 36-42.

[205] H. Fujiwara, M. Kondo, Effects of carrier concentration on the dielectric function of ZnO: Ga and In 2 O 3: Sn studied by spectroscopic ellipsometry: analysis of free-carrier and band-edge absorption, *Phys. Rev. B* **71** (2005) 075109.

[206] O. Fuentes*, et al.*, Improving the width of lossy mode resonances in a reflection configuration D-shaped fiber by nanocoating laser ablation, *Opt. Lett.* **45** (2020) 4738-4741.

[207] N. Paliwal, J. John, Theoretical modeling of lossy mode resonance based refractive index sensors with ITO/TiO 2 bilayers, *Appl. Opt.* **53** (2014) 3241-3246.

[208] A. Ozcariz*, et al.*, A comprehensive review: Materials for the fabrication of optical fiber refractometers based on lossy mode resonance, *Sensors* **20** (2020) 1972.

[209] F.J. Arregui*, et al.*, Giant sensitivity of optical fiber sensors by means of lossy mode resonance, *Sens. Actuators B Chem.* **232** (2016) 660-665.

[210] D. Kaur*, et al.*, High sensitivity lossy mode resonance sensors, *Sens. Actuators B Chem.* **198** (2014) 366-376.

[211] C. Lee*, et al.*, Quantum plasmonic sensors, *Chem. Rev.* **121** (2021) 4743-4804.

[212] P. Sezemsky*, et al.*, Tailoring properties of indium tin oxide thin films for their work in both electrochemical and optical label-free sensing systems, *Sens. Actuators B Chem.* (2021) 130173.

[213] Q. Wang*, et al.*, Lossy mode resonance-based fiber optic sensor using layer-by-layer SnO2 thin film and SnO2 nanoparticles, *Appl. Surf. Sci.* **492** (2019) 374-381.

TH-2572_156121026

List of Publications

Peer reviewed Journals (included in the thesis work)

1. **Sumit Goswami**, Ashwini Kumar Sharma, "Material platform for realization of a *fiber-like* lossy mode resonance response in a simple Kretschmann–Raether geometry", Opt. Lett. **46**, 3065–3068 (2021).
2. **Sumit Goswami**, Ashwini Kumar Sharma, Subrata Biswas, and Perumal Alagarsamy, "Evolution of epsilon-near-zero plasmon with surface roughness and demonstration of perfect absorption in randomly rough indium tin oxide thin films", J. Appl. Phys. **130**, 173102 (2021).
3. **Sumit Goswami**, Ashwini Kumar Sharma, "Widely tunable epsilon-near-zero properties of pulsed laser deposited indium tin oxide thin films probed at different ambient conditions", (**Manuscript Under Preparation**).
4. **Sumit Goswami**, Ashwini Kumar Sharma, "Film thickness dependency and refractive index sensing capabilities of lossy mode resonances in metallic indium-rich ITO thin films", (**Manuscript Under Review**).

Peer reviewed Journals (outside the thesis work)

1. **Sumit Goswami,** Ashwini Kumar Sharma, "Investigation of the optical behavior of indium oxide thin films with the aid of spectroscopic ellipsometry technique", **Appl. Surf. Sci.** 495 (2019) 143609.

2. **Sumit Goswami**, Ashwini Kumar Sharma, "Multiple band thin film perfect absorber based on lossy mode resonances", (**Manuscript Under Preparation**).

Conference proceedings

1. **Sumit Goswami** and Ashwini Kumar Sharma, "Effect of ambient conditions on the structural and optical properties of pulsed laser deposited indium tin oxide thin films," Paper No. **SP 134**, Proceedings of the Photonics 2018, ISBN: 978-93-88653-41-1

TH-2572_156121026

2. **Sumit Goswami** and Ashwini Kumar Sharma, "Structural and Morphological Properties of Pulsed Laser Deposited In_2O_3 Thin Films at Various Oxygen Pressures," AIP Conference Proceedings **2082**, 040008 (2019).

3. **Sumit Goswami** and Ashwini Kumar Sharma, "Ambient condition dependent surface plasmon resonance properties of pulsed laser deposited ITO thin films," 2019 Workshop on Recent Advances in Photonics (WRAP). IEEE, pp. 1-3.

4. **Sumit Goswami** and Ashwini Kumar Sharma, "Perfect absorption in a pulsed laser deposited sub-wavelength thick indium tin oxide thin film via Kretschmann-Raether geometry," Contributory Paper no.: CP-06-307, 29th DAE-BRNS National Laser Symposium (NLS-29) (2021).

Conferences/ Symposium Attended

1. Attended the Symposium on **30 Years of Photonic Crystals – the Indian Research Scenario** (sponsored by SERB, IIT Kanpur and IEEE-UP Section) held during 21st September, 2017 to 23rd September, 2017 at IIT Kanpur.
2. Presented a Poster at **Research Conclave'18** organized by Students' Academic Board, Indian Institute of Technology Guwahati, India.
3. Presented a poster entitled "***Effect of ambient conditions on the structural and optical properties of pulsed laser deposited indium tin oxide thin films***" in Photonics 2018 organized by Indian Institute of Technology Delhi on December 12-15, 2018.
4. Presented a poster entitled "***Structural and Morphological Properties of Pulsed Laser Deposited In_2O_3 Thin Films at Various Oxygen Pressures***" in the International Conference on Optoelectronic and Nano Materials for Advanced Technology (icONMAT 2019 held during January 3-5, 2019) at Cochin University of Science and Technology, Kochi, India.
5. Presented a poster entitled "***Effect of Substrate Temperature on the Structural, Morphological and Optical Properties of Pulsed Laser Deposited Indium Oxide Films***" in the International Conference on Nanoscience and Nanotechnology (ICONN 2019) organized by Department of Physics and Nanotachnology, SRM IST – India during 28 – 30 January 2019.

TH-2572_156121026

6. Presented a poster entitled "***Ambient condition dependent surface plasmon resonance properties of pulsed laser deposited ITO thin films***," in 2019 Workshop on Recent Advances in Photonics (WRAP) held during December 13-14, 2019 in IIT Guwahati, Guwahati.
7. Presented a poster entitled "**Perfect absorption in a pulsed laser deposited sub-wavelength thick indium tin oxide thin film via Kretschmann-Raether geometry**" in the 29th **DAE-BRNS** National Laser Symposium (NLS-29) organized in collaboration with Indian Laser Association and Shri Vaishnav Vidyapeeth Vishwavidyalaya, Indore during February 12-15, 2021.

Workshop/School/Exhibition

1. Participated in the "**One-Day workshop on Vacuum Technology and its Applications in Optical Science**" jointly organized by SPIE IIT Guwahati Student Chapter and Pfeiffer Vacuum Pvt. Ltd., in association with Department of Physics, IIT Guwahati on 19th August, 2017 at IIT Guwahati.
2. Participated in the **Latex workshop** organized by Research Scholar Forum, EEE of IIT Guwahati held on September 9, 2017.
3. Participated in the **Advanced Excel/Advanced Origin/ImageJ** workshop at Research Conclave'18 organized by Students' Academic Board, Indian Institute of Technology Guwahati, India.
4. Participated in the Short Term Course on "**Nanomaterials and Smart Devices**" conducted under the Technical Education Quality Improvement Programme (TEQIP) sponsored by Ministry of Human Resource Development, Government of India, held on 17-21 September, 2018 at IIT Guwahati.

List of Awards/Accolades

1. Received Best Poster Award for the poster entitled "***Effect of Substrate Temperature on the Structural, Morphological and Optical Properties of Pulsed Laser Deposited Indium Oxide Films***" in the International Conference on Nanoscience and Nanotechnology (ICONN 2019) organized by Department of Physics and Nanotachnology, SRM IST – India during 28 – 30 January 2019.

TH-2572_156121026

2. Delivered an invited talk entitled "***Ellipsometric Characterization of Pulsed Laser Deposited Indium Oxide Thin films Grown at Different Substrate Temperature Using Combination of Tauc-Lorentz and Gaussian Oscillators Models***" on "National Science Day 2019" organized by Department of Physics, IIT Guwahati on 28th February, 2019.

TH-2572_156121026